Technische Universität München
TUM School of Engineering and Design

Process gas influences during the powder bed fusion of metals using a laser beam

Siegfried Hugo Bähr

Vollständiger Abdruck der von der TUM School of Engineering and Design der Technischen Universität München zur Erlangung eines

Doktors der Ingenieurwissenschaften (Dr.-Ing.)

genehmigten Dissertation.

Vorsitz: Prof. Dr.-Ing. Katrin Wudy

Prüfende der Dissertation:

1. Prof. Dr.-Ing. Michael F. Zäh
2. Prof. Dr. Ali Gökhan Demir

Die Dissertation wurde am 20.02.2025 bei der Technischen Universität München eingereicht und durch die TUM School of Engineering and Design am 30.06.2025 angenommen.

Editors' Preface

In times of global challenges, such as climate change, the transformation of mobility, and an ongoing demographic change, production engineering is crucial for the sustainable advancement of our industrial society. The impact of manufacturing companies on the environment and society is highly dependent on the equipment and resources employed, the production processes applied, and the established manufacturing organization. The company's full potential for corporate success can only be taken advantage of by optimizing the interaction between humans, operational structures, and technologies. The greatest attention must be paid to becoming as resource-saving, efficient, and resilient as possible to operate flexibly in the volatile production environment.

Remaining competitive while balancing the varying and often conflicting priorities of sustainability, complexity, cost, time, and quality requires constant thought, adaptation, and the development of new manufacturing structures. Thus, there is an essential need to reduce the complexity of products, manufacturing processes, and systems. Yet, at the same time, it is also vital to gain a better understanding and command of these aspects.

The research activities at the Institute for Machine Tools and Industrial Management (*iwb*) aim to continuously improve product development and manufacturing planning systems, manufacturing processes, and production facilities. A company's organizational, manufacturing, and work structures, as well as the underlying systems for order processing, are developed under strict consideration of employee-related requirements and sustainability issues. However, the use of computer-aided and artificial intelligence-based methods and the necessary increasing degree of automation must not lead to inflexible and rigid work organization structures. Thus, questions concerning the optimal integration of ecological and social aspects in all planning and development processes are of utmost importance.

The volumes published in this book series reflect and report the results from the research conducted at *iwb*. Research areas covered span from the design and development of manufacturing systems to the application of technologies in manufacturing and assembly. The management and operation of manufacturing systems, quality assurance, availability, and autonomy are overarching topics affecting all areas of our research. In this series, the latest results and insights from our application-oriented research are published, and it is intended to improve knowledge transfer between academia and a wide industrial sector.

Rüdiger Daub *Gunther Reinhart* *Michael Zäh*

Preface

This dissertation was elaborated during my work as a research associate and as a member of the management board of the Institute for Machine Tools and Industrial Management (*iwb*) at the Technical University of Munich.

First and foremost, I would like to express my deepest gratitude to my supervisor, Prof. Dr.-Ing. Michael F. Zaeh, for granting me the opportunity to pursue a doctorate and for his guidance and support during the past years. I am also thankful for the opportunity he gave me to contribute to the management board of the *iwb* and to head the Additive Manufacturing department.

I further wish to thank my second examiner, Prof. Dr. Ali Goekhan Demir, for his expertise and invaluable input during the final stages of my doctoral journey, as well as for his evaluation of this dissertation. I also appreciate Prof. Dr.-Ing. Katrin Wudy for kindly serving as the chair of the examination committee.

My gratitude extends to the former Additive Manufacturing department at the Linde GmbH, especially to Pierre Forêt, for generously financing this work. I am particularly indebted to my mentor there, Thomas Ammann, for his excellent supervision, his dedicated involvement, and the many meaningful discussions that shaped this project – and often went far beyond it.

I am also thankful to the many colleagues in Garching and in Unterschleissheim, who made this period a memorable and enriching experience. I would particularly like to thank Tobias Deckers for being such a great office mate and for pushing each other forward throughout this journey. Furthermore, I am thankful to Andreas Wimmer, Xiao Fan Zhao, Daniel Baier, Sophie Grabmann, Sophie Dubiez-Le Goff, and Dominik Bauer for their motivation and thoughtful feedback.

Finally, I would like to express my heartfelt thanks to my family and friends for their unwavering support over the years, without which the completion of this thesis would not have been possible. I am sincerely grateful to my parents, Frauke and Gerhard Bähr, who imparted the value of education to me from an early age and have always stood by my side with advice and encouragement. I also thank my brother, Julius Bähr, for offering new perspectives through our conversations and for expanding my way of thinking. Lastly, I am grateful to my partner Bianca for her patience and mental support during the final stages of this dissertation.

Munich, September 2025 *Siegfried Bähr*

Table of contents

List of abbreviations

Abbreviation	Description
2D	Two-dimensional
3D	Three-dimensional
AER	Chair of Aerodynamics and Fluid Mechanics of the Technical University of Munich
AM	Additive manufacturing
CFD	Computational fluid dynamics
CT	Computational tomography
CW	Continuous wave
EBSD	Electron backscatter diffraction
EDX	Energy-dispersive X-ray spectroscopy
e.g.	For example (lat.: exempli gratia)
FEM	Finite element method
HWA	Hot-wire anemometry
i.e.	That is (lat.: id est)
iwb	Institute for Machine Tools and Industrial Management of the Technical University of Munich
L	Lens
LW	Laser welding
OT	Optical tomography
P	Publication
PBF-LB/M	Powder bed fusion of metals using a laser beam
RA	Research area
RF	Research finding
SEM	Scanning electron microscopy
SO	Sub-objective
SPH	Smoothed-particle hydrodynamics

UTS	Ultimate tensile strength
VA	Vane anemometry
VED	Volumetric energy density
YS	Yield strength

List of symbols

Chemical symbols

Variable	Description
Al	Aluminum
Ar	Argon
ArHe30	70 vol.-% argon + 30 vol.-% helium
ArHe70	30 vol.-% argon + 70 vol.-% helium
CO	Carbon monoxide
CO_2	Carbon dioxide
Cu	Copper
He	Helium
Mg	Magnesium
N_2	Nitrogen molecule
O	Atomic oxygen
O_2	Molecular oxygen
Ti	Titanium
Zn	Zinc

Greek symbols

Variable	Unit	Description
α	$W/(m^2 \cdot K)$	Heat transfer coefficient
$\alpha(\lambda)$	-	Absorptivity
δ	mm	Boundary layer thickness
$\delta(x)$	mm	Boundary layer thickness profile
$\varepsilon(\lambda)$	-	Spectral emission coefficient
$\varepsilon_{x,z}$	rad	Deflection in the x- or z-direction

η_g	µPa·s	Dynamic viscosity of a gas
$\eta_{i,j}$	µPa·s	Dynamic viscosity of the gases i and j
η_{mix}	µPa·s	Dynamic viscosity of a gas mixture
λ	nm	Wavelength
λ_e	nm	Real wavelength
λ_g	W/(m·K)	Thermal conductivity of a gas
λ_{mix}	W/(m·K)	Thermal conductivity of a gas mixture
λ_v	nm	Wavelength ratio
λ_w	W/(m·K)	Thermal conductivity of a wall
ρ_c	kg/m³	Density of a gas at calibration conditions
ρ_g	kg/m³	Density of a gas
ρ_i	kg/m³	Density of a gas i in a gas mixture
$\rho(\lambda)$	-	Reflectivity
ρ_m	kg/m³	Density of a gas at measurement conditions
ρ_{mix}	kg/m³	Density of a gas mixture
ρ_p	kg/m³	Density of a powder particle
σ	mN/m	Surface tension coefficient
σ_B	W/(m·K^4)	Stefan-Boltzmann constant
τ	-	Transmissivity
Ω	rad	Unit solid angle

Latin symbols

Variable	Unit	Description
a_w	m²/s	Thermal diffusivity of a wall
A	m²	Exposed surface area
A_O	m²	Object surface
A_p	µm²	Particle surface
$Arch$	-	Archimedes number
A_S	µm²	Pyrometer surface
A_w	m²	Wall surface
c_0	m/s	Speed of light in vacuum

c_1	W·m²	Radiation constant
c_2	K·m	Radiation constant
c	m/s	Speed of light in a medium
c_g	€/m³	Gas cost per volume
$\tilde{c}_{p,i}$	kJ/(mol·K)	Molar specific isobaric heat capacity of a gas i
$c_{p,i}$	kJ/(kg·K)	Specific isobaric heat capacity of a gas i
$c_{p,mix}$	kJ/(kg·K)	Specific isobaric heat capacity of a gas mixture
c_w	-	Drag coefficient
C	€	Overall part costs
C_{cons}	€	Consumables costs
C_{en}	€	Energy consumption costs
C_{eq}	€	Equipment costs
C_{fac}	€	Facility costs
C_{gas}	€	Gas costs
C_{lab}	€	Labor work costs
C_{mat}	€	Material costs
C_{pp}	€	Post-processing costs
C_{setup}	€	Process setup costs
Δd	µm	Displacement of a deflected light beam
d_k	µm	Remaining diameter of a cut-off undisturbed light beam
d_0	µm	Diameter of an indisturbed light beam
d_p	µm	Particle diameter
d_s	µm	Diameter of an ideal point light source
d_w	m	Wall thickness
f	-	Scrap rate
$f_{1,2}$	mm	Focal lengths
F	N	Drag force
$\bar{F}$	-	Normalized drag force
FOV	µm²	Field of view
F_S	-	System parameters term
g	m²/s	Gravitational acceleration
h	µm	Hatch distance

h_P	J·s	Planck's quantum of action
i	-	Control variable
I_0	lx	Undisturbed illumination
I_k	lx	Cut-off illumination
j	-	Control variable
k	cm^3/g	Gladstone-Dale coefficient
K_D	-	Modification factor for the flow profile
K_Φ	-	Modification factor for the particle shape
L	mm	Characteristic length
$L(\lambda,T)$	$W/(m^2 \cdot \mu m \cdot sr)$	Spectral radiance
L_O	$W/(m^2 \cdot \mu m \cdot sr)$	Spectral radiance of an object
L_V	kJ/mol	Enthalpy of vaporization
$M_{i,j}$	kg/mol	Molar masses of the gases *i* and *j*
$M(\lambda,T)$	$W/(m^2 \cdot \mu m)$	Specific spectral radiation
$M_{BB}(T)$	$W/(m^2 \cdot \mu m)$	Specific spectral radiation of a black body
$M_{RB}(T)$	$W/(m^2 \cdot \mu m)$	Specific spectral radiation of a real body
n	-	Number of constituents in a gas mixture
n_0	-	Refractive index of a surrounding medium
n_b	-	Number of parts per build job
n_g	-	Refractive index of a gas
Nu	-	Nusselt number
Nu_{forced}	-	Nusselt number in the case of forced convection
$Nu_{natural}$	-	Nusselt number in the case of natural convection
p	Pa	Pressure
p_b	Pa	Saturated pressure
p_I	Pa	Ambient pressure
Pr	-	Prandtl number
p_{rec}	Pa	Recoil pressure
$\dot{Q}_{cond}$	W	Heat flux by conduction
$\dot{Q}_{conv}$	W	Heat flux by convection
$\dot{Q}_{rad}$	W	Heat flux by radiation
$\dot{Q}_{total}$	W	Total heat flux

$\dot{q}$	W/m²	Heat flux density
R	J/(mol·K)	Universal gas constant
Ra	-	Rayleigh number
Re	-	Reynolds number
Re_{crit}	-	Critical Reynolds number
Re_{p}	-	Particle Reynolds number
R_{S}	µm	Pyrometer sensitivity
S_{A}	V	Pyrometer output signal
S_{R}	-	Pyrometer signal ratio
t	µm	Layer thickness
t_{build}	h	Processing time
t_{purge}	h	Purging time
ΔT	K	Temperature difference
T	K	Temperature
T_{b}	K	Boiling temperature
t_{c}	s	Time
T_{O}	K	Object temperature
u_{c}	m/s	Calibration velocity
u_{g}	m/s	Gas flow velocity
u_{m}	m/s	Measurement velocity
u_{pu}	m/s	Particle pickup velocity
$u(x,z)$	m/s	Gas flow velocity profile
v	m/s	Scanning velocity
$\dot{V}_{\mathrm{build}}$	m³/h	Volume flow rate of the gas during processing
$\dot{V}_{\mathrm{purge}}$	m³/h	Volume flow rate of the gas during purging
VED	J/mm³	Volumetric energy density
$\tilde{x}_{\mathrm{i}}$	-	Molar fraction
x, y	-	Scanning or gas flow directions
z	-	Building direction
Z_{ij}	-	Weighting factor

1 Introduction

1.1 Additive manufacturing – a driver for innovation in industrial production?

Additive manufacturing (AM) is a production technique characterized by a repetitive layer-by-layer deposition of material (GEBHARDT 2016). This additive deposition of the material enables the production of complex geometries, which are not or only difficult to produce conventionally in an economical way (GIBSON ET AL. 2021). When the freedom of design is introduced in an early design stage in the product development, the benefits of AM can be fully exploited – parts with integrated functionalities and topology-optimized designs in a near-net-shape geometry are manufacturable (RUDOLPH ET AL. 2023). Additionally, since the material is theoretically only deposited and used where it is needed, the material efficiency of the production can be increased. This leads to reduced wastage or buy-to-fly ratios (WILLIAMS ET AL. 2016). Coming from prototyping mainly, AM has emerged as a relevant production method over recent years. In the field of metal additive manufacturing, the powder bed fusion of metals using a laser beam (PBF-LB/M) has especially been established as one of the most prominent technologies (GIBSON ET AL. 2021). This process uses a fine metal powder that is molten in layer-by-layer mode by a laser beam to manufacture the final part. A high resolution of parts and a fine microstructure are benefits of this specific additive technology (CHOWDHURY ET AL. 2022). In particular, parts that require a high specific strength (i.e., high mechanical strength and low density) and are needed in small numbers are predestined to be produced via PBF-LB/M (GEBHARDT 2016).

Some challenges, however, still stand against the variety of benefits that limit the current use of this promising manufacturing technique in the production industry. A few of these challenges are associated with the nature of the process leading to high and costly requirements in the production environment, for example, regarding safety and production atmosphere (WALTER ET AL. 2019). As the handled fine metal powders are usually in respirable size ranges and are prone to pick up oxygen or humidity from the ambient air, workers need to wear personal protection equipment and the machines need to be placed in encapsulated laboratories with a regulated ambient temperature and humidity (WALTER ET AL. 2019). Other barriers that hinder the further spreading of PBF-LB/M in the industry are posed by process-related challenges. High production times compared to conventional manufacturing processes, low reproducibility of the part properties, or process abortions due to part failures during manufacturing are a few examples of challenges that need to be resolved (NARASIMHARAJU ET AL. 2022).

Therefore, to further establish PBF-LB/M as a driver for innovation in industrial production and to fully exploit its potential, research institutes and companies are investing a significant amount of effort into the research on and the development of this manufacturing technology.

1.2 Problem statement, objectives, and approach

PBF-LB/M is characterized by a high energy density input from a laser beam in a confined area with rapid heating and cooling cycles (GIBSON ET AL. 2021). The material is heated up according to the cross-section of the part until a melt pool is created. By the following solidification, one layer of the part is produced. If the energy input is sufficiently high, the material can even evaporate, leading to the creation of an indentation in the melt pool (keyhole) and a continuous stream of vapor out of it (DEBROY ET AL. 2018). To protect the liquid melt pool from chemical reactions with the ambient air, such as oxidation or nitridation, the process chamber of the machine is flooded with an inert gas prior to the process (GEBHARDT 2016). The high scanning velocities of the laser movement of approximately 1 m/s and above result in strong melt pool dynamics and lead to high solidification rates of the material. Process by-products, such as vapor and spatters (ejected liquid metal droplets), are the result of the high process dynamics (DEBROY ET AL. 2018). To avoid negative impacts by the process by-products, such as interactions with the laser beam or altering of the powder bed properties, a continuous inert gas flow is guided over the build platform to remove them. To date, the influence of the process gas on PBF-LB/M has not been fully uncovered. Argon (Ar) or nitrogen (N_2) are used as standard gases with parameter settings that are not touched (GEBHARDT 2016). The use of the process gas as an additional parameter to increase the process stability and capability has only been studied to a limited extent. Investigations of resulting part properties that were produced with different atmosphere settings were oftentimes used to draw conclusions on the influence of the process gas, such as in the works of PAUZON ET AL. (2019) or DECKERS ET AL. (2024). However, a comprehensive and transferable understanding of the influences of the process gas on PBF-LB/M remains difficult with only experimental ex-situ methods at hand.

This dissertation project aimed to unveil fundamental influences of the gas used during PBF-LB/M and to contribute to an enhanced usage of this parameter. In particular, the focus points of the removal of process by-products through the gas flow and the heat balance in the process were addressed. Figure 1-1 depicts the four-stage approach that was applied to achieve this overall goal. In stage 1, preliminary investigations were performed based on the state of the art to gain a better understanding of the relevant phenomena to be studied. The second and third stages were built upon the results of stage 1 and were dedicated to investigations on the removal of spatters and the heat balance in the process. Stage 2 thereby addressed the removal of spatters by a two-step approach. First, the upper limits of the gas flow velocity in any gas-material setting were elaborated. With this knowledge, the removal of spatters was studied with a unique and novel experimental setup. In stage 3, the heat balance during PBF-LB/M was studied with the goal of unveiling the spatter cooling by the gas flow as well as the heat transfer mechanisms of the melt pool. Experimentally, this was done by Schlieren imaging and metallography. For the analytical approaches, a formula-based heat transfer model and a smoothed-particle hydrodynamics simulation model were applied. In the final stage 4, a comprehensive experimental study was performed to showcase the potential of the process gas as an additional parameter to improve PBF-LB/M. This was done by investigating the density, chemical composition, and static mechanical properties of parts produced under varying atmospheres.

In summary, the presented approach supports the choice of a suitable process gas and its application to PBF-LB/M. Beyond the results shown in this thesis, the presented models can be applied to any combination of gases and materials to find proper process settings.

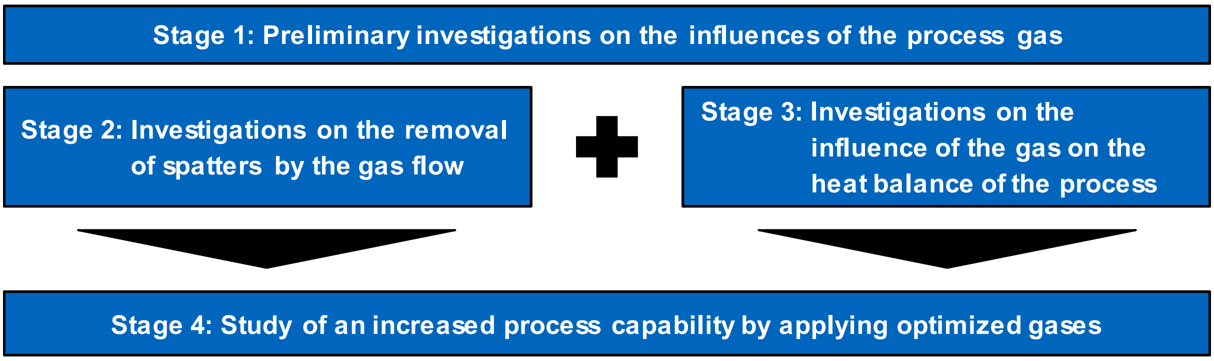

Figure 1-1: Scientific approach of this dissertation project

1.3 Structure of the thesis

This cumulative thesis is structured in six main chapters. After the introduction in Chapter 1, Chapter 2 presents the necessary fundamentals for understanding the research results. In particular, the relevant basics of PBF-LB/M, technical gases, fluid mechanics and thermodynamics, and process monitoring devices are elaborated. In Chapter 3, the current state of the art of experimental and numerical investigations on spattering and the influence of gases during PBF-LB/M and its related laser beam welding process are presented. After the formulation of the need for action at the end of Chapter 3, Chapter 4 continues with the description of the research approach. Based on the open research areas, scientific objectives are defined and the methodological approach to solve them is presented. The description of the integration of this approach into the six publications of this publication-based dissertation concludes Chapter 4. The following Chapter 5 contains a summary of each individual publication, followed by a discussion of the findings and an assessment of the degree of achievement of the scientific objectives defined in Chapter 4. Finally, the presented work is summarized in Chapter 6 and an outlook is given on potential future research activities.

2 Fundamentals

2.1 Chapter overview

In this chapter, the fundamentals relevant to this work are presented. Section 2.2 describes the fundamentals of the PBF-LB/M process, followed by basics of technical gases in Section 2.3. The Sections 2.4 and 2.5 conclude Chapter 2 and lay the foundations for the understanding of fluid flow and heat transfer and for process monitoring systems used within this dissertation project, respectively.

Following remarks on the terminology and the principles of the PBF-LB/M process in the Subsections 2.2.1 and 2.2.2, respectively, Subsection 2.2.3 describes the characteristics of the process zone, while Subsection 2.2.4 gives an overview of relevant process parameters. In the beforementioned subsections, the focus is placed on relevant physical phenomena related to the scope of this work, such as laser energy coupling and recoil pressure. This focus is continued in Subsection 2.3.1, as the importance of using process gases is explained by outlining their main tasks in the PBF-LB/M process. Since the performance of process gases in fulfilling their tasks during PBF-LB/M depends on their properties as well as on the flow settings, the Subsections 2.3.2 and 2.3.3 give an overview of the properties of technical gases and the principles of gas flow measurements, respectively. Subsection 2.4.1 continues in the context of gas flow properties with a description of the boundary layer theory, followed by the main basics of heat transfer in Subsection 2.4.2. Based on general remarks on process monitoring techniques in Subsection 2.5.1, the Subsections 2.5.2 and 2.5.3 deal with the working principles of Schlieren imaging and pyrometry, respectively.

2.2 Powder bed fusion of metals using a laser beam

2.2.1 Terminology

The industrially most relevant standard for the terminology of AM processes today is the DIN EN ISO/ASTM 52900 standard. It categorizes the AM processes based on their specifications. Seven main process categories are defined:

- Binder jetting
- Directed energy deposition
- Material extrusion
- Material jetting
- Powder bed fusion (PBF)
- Sheet lamination
- Vat photopolymerization

The processes belonging to PBF are further divided based on the energy source (laser beam (LB) or electron beam) and the material used (e.g., metals (M) or plastics). With this definition, the abbreviation for the process applied in this work, the powder bed fusion of metals using a laser beam, is PBF-LB/M (DIN EN ISO/ASTM 52900:2021).

2.2.2 Principle of the process

For a successful manufacturing of parts by PBF-LB/M, pre-, in- as well as post-processing steps need to be performed before, during, and after the actual fabrication (VDI 3405:2014). During pre-processing, the part modeled by computer-aided design is virtually sliced and the resulting layers are attributed with processing parameters. The main parameters are the laser power, the scanning velocity of the laser beam, the hatch distance (distance between the center lines of two neighboring scan paths), and the layer thickness. Process characteristics, such as overheating in the turning points of the laser, might require variations of the processing parameters within one layer of the part or the addition of support structures at overhanging areas. Once the digital preparation of the part is finished, the model can be transferred to the PBF-LB/M machine. (GIBSON ET AL. 2021)

Figure 2-1 shows a schematic cross-section of a typical PBF-LB/M machine with its main components. The machine is prepared for manufacturing by various steps, such as inertizing the build chamber (see Figure 2-1 (1)) with a suitable processing gas (typically Ar or N_2) or filling in the metal powder into the powder reservoir (see Figure 2-1 (2)).

Once the machine is set up, the PBF-LB/M process can be started. In this paragraph, the numbers called refer to Figure 2-1. Three main steps are repeatedly performed for the layer-by-layer fabrication of the part (3). In the first step, a layer of powder is applied onto the build platform (4). For this, the recoating device (6) is moved to the right end position, then the powder reservoir (2) is lifted by a pre-defined height increment, and the recoating device moves to the left end position again. A blade (typically metal or rubber), which is mounted at the bottom of the recoating device, shoves the powder evenly onto the build platform. Any excess powder from the recoating step is collected in the overflow container (5). In the second step, the laser illumination, the beam of a typically continuous wave (CW; (HÜGEL & GRAF 2009)) laser source (7) is guided over the build platform following the contour of the part. The energy input from the laser beam leads to the melting of the metal powder. The high scanning velocities of up to 1 m/s lead to a rapid cooling of the resulting melt pool and, hence, to a solidification of the material. Once the laser beam has passed the entire contour of the part, one layer of the part is created. In the third step, the build platform is lowered by the pre-defined layer thickness and the process starts again with the first step. This cycle is repeated until the entire part is built. (WANG ET AL. 2024)

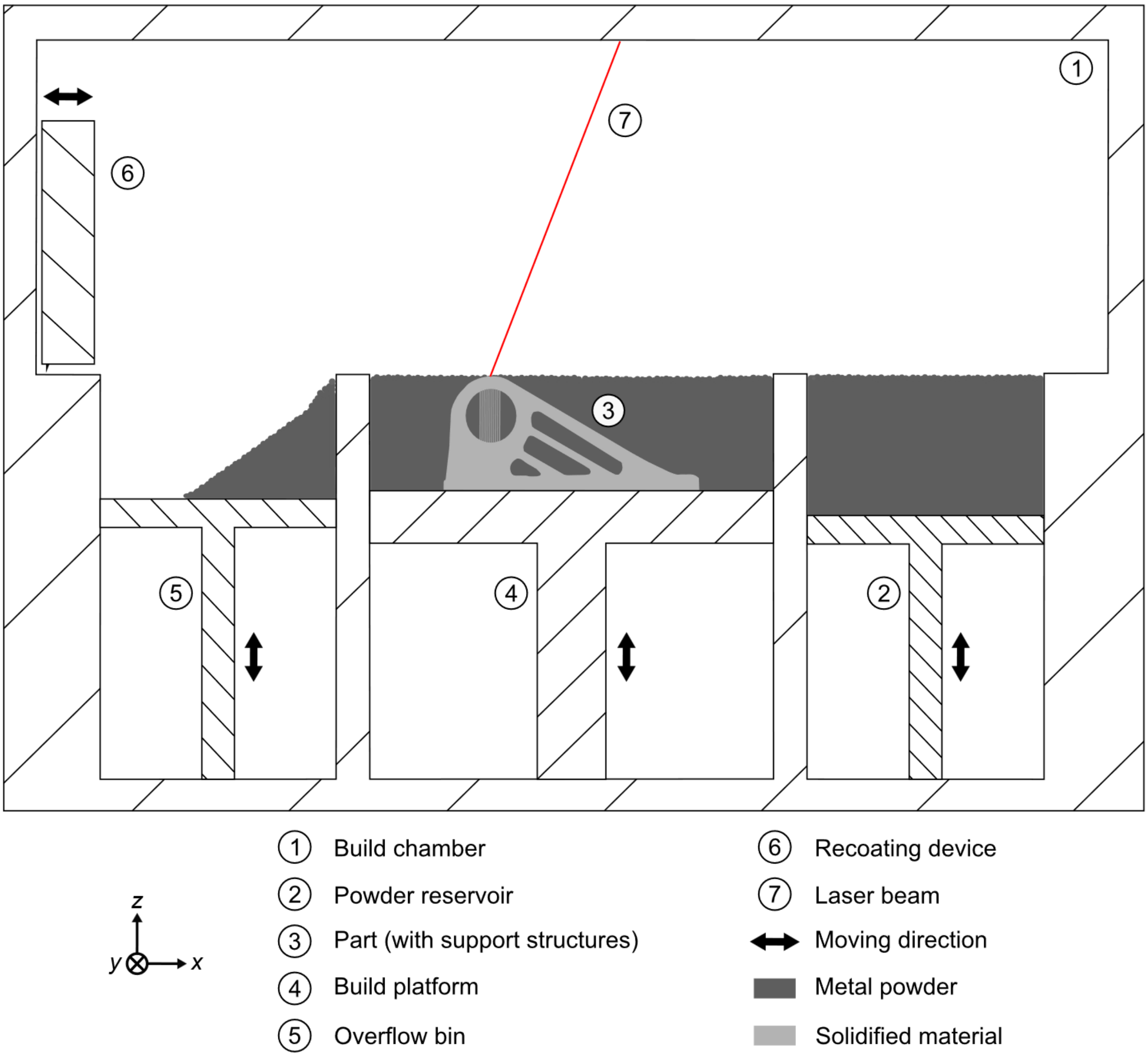

Figure 2-1: Schematic cross-section of a typical PBF-LB/M machine (not to scale); z: building direction (own representation based on WANG ET AL. (2024); exemplary part design based on AIRBUS (2016))

2.2.3 Characteristics of the process zone

In the second step of the PBF-LB/M process, the laser is activated leading to the emission of a laser beam in the infrared range with a typical wavelength of 1064 nm and a gaussian energy distribution. When the laser beam reaches the metal powder, a part of it is absorbed and a part of it is reflected by the material (KATAYAMA 2020). Transmission is not happening, since the metal powder is an opaque material. The absorptivity $\alpha(\lambda)$ following the Fresnel absorption and the reflectivity $\rho(\lambda)$, each with a value that ranges from 0 to 1, depend on the material and wavelength used and are related by (HÜGEL & GRAF 2009)

$$\alpha(\lambda) + \rho(\lambda) = 1. \quad (1)$$

The absorbed radiation heats up the material leading to the creation of a melt pool (KATAYAMA 2020). This melt pool typically expands over several already solidified layers. Figure 2-2 illustrates the process zone and relevant characteristics of the melt pool in PBF-LB/M in detail.

In the following paragraphs of this section, the numbers called refer to Figure 2-2. Between the melt pool (6) and its environment, heat transfer by conduction (8), radiation (9), and convection (10) occurs. Into the underlying solidified material (5), heat is transferred by conduction. The latter happens to be the most significant source of cooling for the melt pool. Between the melt pool and the ambient atmosphere, heat is transferred by radiation and convection. Radiation is mostly neglected in research about PBF-LB/M due to its comparably low impact. Heat transfer by convection is a result of the gas flow (2) above the process zone. (DEBROY ET AL. 2018)

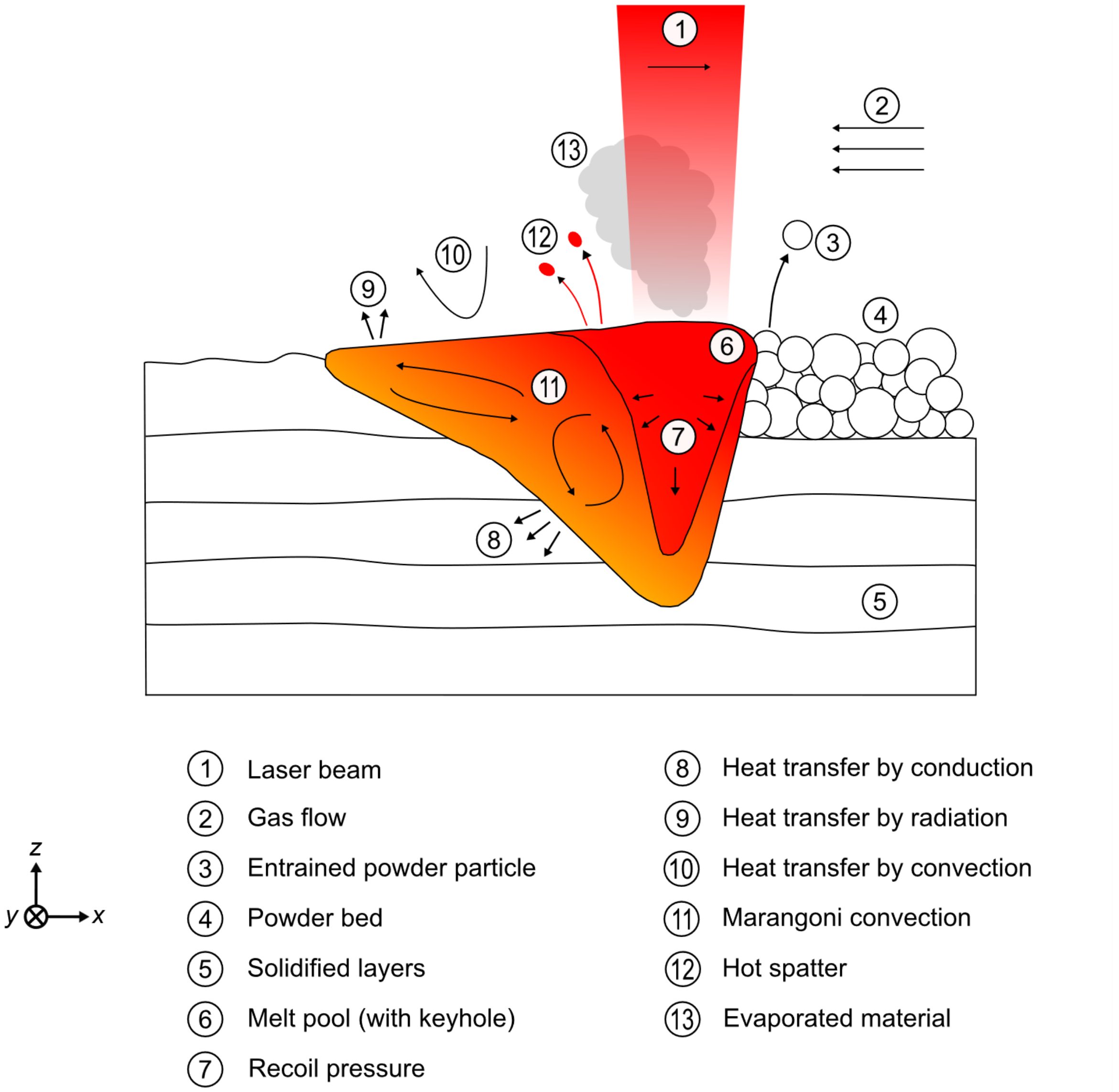

Figure 2-2: Schematic cross-section of the PBF-LB/M process zone and its characteristics as well as relevant physical phenomena (not to scale); z: building direction (own representation based on BERGMUELLER ET AL. (2023))

The shape of the melt pool is determined by various complex interacting physical phenomena. In the center of the laser beam, when the laser energy is high enough to heat up the material until its boiling point, evaporation (13) occurs. This requires special attention when processing materials with volatile elements with low boiling points, as the part properties can be influenced in this way (DEBROY ET AL. 2018). With an increasing evaporation of material, the recoil pressure p_{rec} (7) from the evaporated material leads to a penetration of the melt pool and, thus to the formation of a steeply indented keyhole (vapor capillary) (6). The calculation of p_{rec} is most commonly derived from Anisimov's evaporation model and formulated as (ANISIMOV 1968)

$$p_{\mathrm{rec}} = 0.54 \cdot p_{\mathrm{b}} \cdot \exp\left(L_{\mathrm{v}} \cdot \frac{T - T_{\mathrm{b}}}{R \cdot T \cdot T_{\mathrm{b}}}\right), \quad (2)$$

with the liquid surface temperature T, the saturated pressure p_{b} at the boiling temperature T_{b}, the enthalpy of vaporization of the liquid L_{v}, and the universal gas constant R (XIA & PESTANA 2023). Figure 2-3 (a) exemplarily shows the exponential increase of p_{rec} over T for iron.

The liquid metal is moved by buoyancy effects as well as surface tension forces following the so-called Marangoni convection (HÜGEL & GRAF 2009). This phenomenon causes the molten material to move from the center of the melt pool with the maximum temperatures towards its outer areas with lower temperatures (PEI ET AL. 2023). At the cold boundaries, the flow is deflected downwards leading to a circulation within the melt pool. Figure 2-3 (b) shows the surface tension coefficient σ over T with the assumption of no oxygen activity. It can be seen that σ decreases linearly with an increasing T.

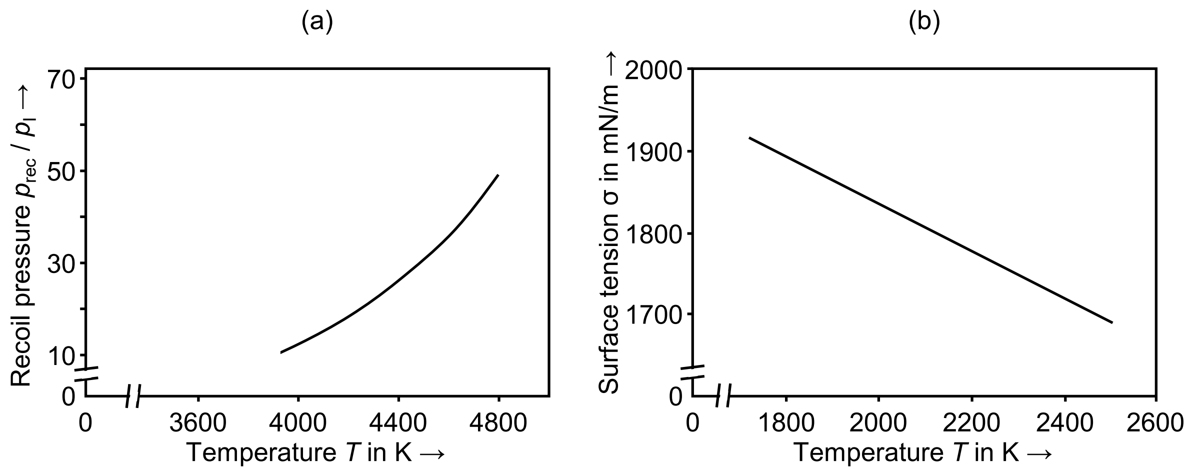

Figure 2-3: (a) Ratio of the recoil pressure p_{rec} and the ambient pressure p_l of iron as a function of the temperature T (own representation based on LIU & WEN (2022)), (b) surface tension σ of iron as a function of the temperature T with the assumption of no oxygen activity (own representation based on WILLE ET AL. (2002))

As a result of the dynamics and physical phenomena in the process zone, by-products are formed. These are entrained powder particles (3), hot liquid melt pool ejections (hot spatter (12)), and evaporated material. These by-products can potentially interact with the laser beam, if their flight trajectory intersects the laser beam path, and, thus, impair the energy input. To avoid those unwanted impairing effects, a gas flow is continuously guided over the process zone.

2.2.4 Process parameters

Primary process parameters

During the laser illumination, several primary parameters influence the final result. In a one-dimensional consideration of a single melt track, these are the laser power *P* and the scanning velocity *v*. The quotient of *P* over *v* defines the line energy density. Both parameters combined span a stable processing window, as illustrated in Figure 2-4. When an unfavorable combination of them is used, various common part or process defects can occur. At a laser power that is too low, lack-of-fusion pores can be created due to insufficient melting and, thus, melt track interruptions. In the opposite case, keyhole porosity can occur as a consequence of an unstable and collapsing vapor capillary due to an excessive laser energy input. When the scanning velocity surpasses a certain limit, the melt can be separated leading to the defect phenomenon of the so-called balling. For further details on the creation mechanism of those defects, the reader is kindly referred to the literature (GIBSON ET AL. 2021).

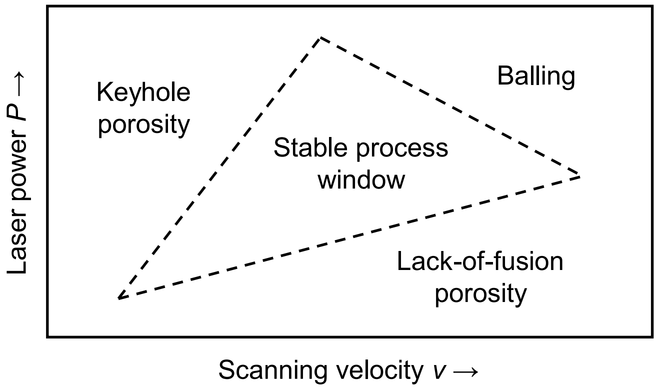

Figure 2-4: Schematic representation of the boundaries of a stable process window and the occurring defects outside of these boundaries (own representation based on PEI ET AL. (2023))

In a layer-oriented two-dimensional (2D) consideration of PBF-LB/M, the hatch distance *h* defines the distance between the center lines of two adjacent melt tracks. This distance needs to be selected considering a trade-off between the productivity and the quality of the parts. The higher it is set, the faster the process step is finished. However, when it is set too high, the connection between the two tracks cannot be ensured. Another parameter to be set on the plane is the scan pattern. The scan pattern describes the manner in which the laser beam is guided over the build platform by the scanning mirrors. In the simplest way, this is done by parallel lines, which are distributed evenly over the layer and illuminated uni-directionally. However, to avoid anisotropy of the mechanical part properties, these parallel lines are commonly turned by a certain angle from layer to layer, thereby creating shorter and longer melt tracks within one layer. As a result, homogeneous part properties can be achieved. This turning angle is oftentimes set to 67°. The value has been found to provide an optimum. A sequence in the scan pattern would be created if a non-prime number is used (PAKKANEN 2018). Other approaches, for example, divide the layer into small squares, which consist of parallel lines within but differ in their angle.

In a three-dimensional (3D) consideration of PBF-LB/M, the layer thickness d becomes relevant. It defines the distance, about which the build platform is lowered after each illumination step. The same trade-off between productivity and part quality, as it appears for the hatch distance, applies to this parameter on the layer level. The four parameters P, v, h, and d define the volumetric energy density (VED), which is regularly used to characterize the PBF-LB/M process (MEINERS 1999):

$$VED = \frac{P}{v \cdot h \cdot d}. \quad (3)$$

To ensure a stable and defect-free manufacturing, several requirements have to be met when selecting the values of the primary parameters. These include, for example, providing a sufficiently high laser power to reach the melting temperature of the material or adjusting the laser power at downward-facing part areas to avoid the adhesion of surrounding powder particles (GIBSON ET AL. 2021).

Secondary parameters

Several further parameters contribute to the process stability and to the production of defect-free parts. In contrast to the primary process parameters, which are well-described in the literature, the influences of these secondary parameters are still to be explored in detail and bring uncertainty into the process planning. A list of secondary parameters is given by the Ishikawa diagram ("fishbone diagram") in Figure 2-5.

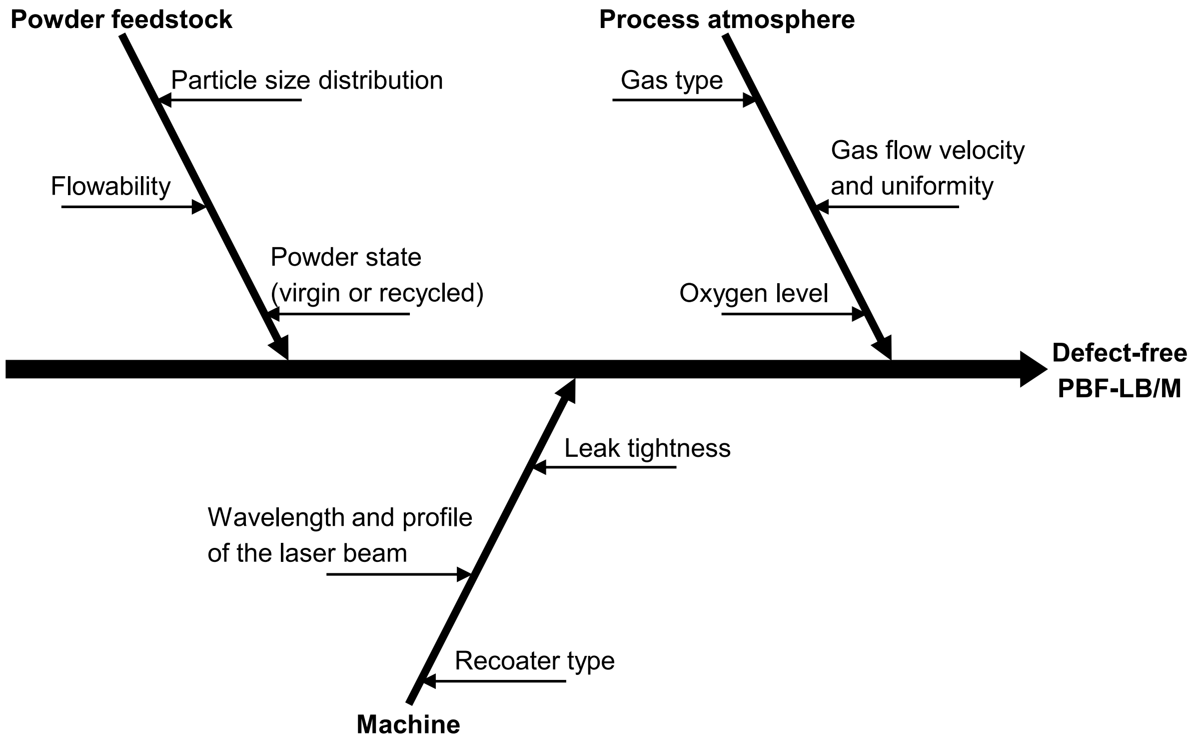

Figure 2-5: Overview of selected secondary process parameters of the PBF-LB/M process (own representation based on KOTADIA ET AL. (2021))

The interactions between primary and secondary parameters are complex and require a careful selection. For example, regarding the powder feedstock, it is crucial to know the particle size distribution to choose a suitable layer height *d*. This avoids uneven powder layers after recoating. Another example is related to the machine. The wavelength of the laser beam source needs to be appropriate for the absorptivity of the material used. This influences the level of *P* and *v* required to enable sufficient melting. For further details on the interactions of the process parameters, the reader is kindly referred to the literature (GRUND 2015, GIBSON ET AL. 2021, KOTADIA ET AL. 2021).

2.3 Process gases

2.3.1 Process gases in the powder bed fusion of metals using a laser beam

The gas used in PBF-LB/M has two main tasks in the process chain. First, it is used to inertize the build chamber and, hence, to lower the content of remaining oxygen in the atmosphere prior to the printing process. This is done to avoid unwanted chemical reactions with the molten metal, such as oxidation or nitration. Typically, Ar or N_2, despite its dissociation behavior, are used as process gases to ensure that the oxygen level is kept below 1000 ppm. During manufacturing, a small amount of this gas is constantly or repeatedly purged into the gas circulation system as a compensation for leakages. Second, a continuous gas flow is guided over the process zone to remove unwanted by-products. (GEBHARDT 2016)

2.3.2 Technical gases and gas properties

In general, gases are considered as the gaseous state of matter. They are mostly invisible and intangible and have neither constant shape nor volume. The use of flammable, oxidizing, and inert gases for technical and industrial applications nowadays covers a wide field. Flammable gases, such as hydrogen or acetylene, can be used in the metals industry for annealing, welding, or cutting of metals. Oxygen (O_2), the main representative of oxidizing gases, is relevant, for example, for refining iron in steel production or for medical applications. Inert gases, such as Ar or He, are used for freezing applications in the food industry or for gas-shielding purposes in the welding of metals. (DOWNIE 2002)

Since the PBF-LB/M process is closely related to traditional welding processes, inert gases are also typically applied. Besides N_2 and Ar, helium (He) is rarely applied. The first two gases are major constituents of air (N_2: 78.1 vol.-% in air, Ar: 0.93 vol.-% in air) and are primarily obtained from the cryogenic air separation process. In this process, air is liquefied and separated into its major constituents by distillation (KENT 1992). Helium, which is only a minor constituent of air (0.00005 vol.-% in air), is produced commercially rather by the liquefaction of natural gas wells.

For the design of technical applications using gases, the properties of these gases must be known. With sufficient accuracy, the aforementioned gases (e.g., N_2, O_2, Ar, and He) behave like ideal gases under atmospheric conditions (i.e., standard temperature and pressure). This includes the assumptions of large distances between the particles, negligibly small expansions of the gas particles, and the obedience of the thermal equation of state. If gas mixtures are used instead of pure gases, this assumption of ideal gases leads to several simplifications in the calculation of the thermo-physical properties of these mixtures. The density ρ_{mix} of a gas mixture can be calculated via a molar fraction average according to

$$\rho_{\mathrm{mix}} = \sum_{i=1}^{n} \rho_{\mathrm{i}} \cdot \tilde{x}_{\mathrm{i}}, \tag{4}$$

with the densities ρ_i and the molar fractions $\tilde{x}_i$ (binary gases: $x_1 + x_2 = 1$) of a number of n contributing gases (POLING ET AL. 2001). For other properties, such as the dynamic viscosity η, thermal conductivity λ, and specific heat capacity c_p, mixing equations must be applied. For binary gas mixtures, the dynamic viscosity η_{mix} depends on the characteristic lengths of the contributing gases i and j and can be determined according to Wilke's rule of mixture (WILKE 1950):

$$\eta_{\mathrm{mix}} = \sum_{i,j=1}^{n} \frac{\tilde{x}_{\mathrm{i}} \cdot \eta_{\mathrm{i}}}{\sum_{j} \tilde{x}_{\mathrm{i}} \cdot Z_{\mathrm{ij}}}. \tag{5}$$

Z_{ij} denotes a weighting factor for the influence of the polarity of the gases and can be calculated according to

$$Z_{\mathrm{ij}} = \frac{[1 + (\eta_{\mathrm{i}}/\eta_{\mathrm{j}})^{1/2} \cdot \left(M_{\mathrm{j}}/M_{\mathrm{i}}\right)^{1/4}]^2}{\sqrt{8 \cdot (1 + \left(M_{\mathrm{i}}/M_{\mathrm{j}}\right))}}, \tag{6}$$

with the molar masses $M_{i,j}$ of the gases. The thermal conductivity λ_{mix} is calculated analogously to η_{mix} according to the rule of mixture from Wassiljeva, Mason, and Saxena (POLING ET AL. 2001).

The specific isobaric heat capacity $c_{p,mix}$ of a gas mixture with $i = 1 \ldots n$ constituents can be determined according to

$$c_{\mathrm{p,mix}} = \sum_{i=1}^{n} \tilde{c}_{\mathrm{p,i}} \cdot \tilde{x}_{\mathrm{i}}, \tag{7}$$

with the molar specific isobaric heat capacity $\tilde{c}_{p,i}$ and the molar fraction $\tilde{x}_i$ (VDI E.V. 2013). The former physical quantity is calculated with the specific isobaric heat capacity $c_{p,i}$ according to

$$\tilde{c}_{\mathrm{p,i}} = c_{\mathrm{p,i}} \cdot M_{\mathrm{i}}. \tag{8}$$

In this work, special focus is placed on the use of He and Ar-He gas mixtures in comparison to Ar for the PBF-LB/M process. Due to its higher thermal properties and lower density compared to Ar, significant differences in the process can be expected. The progressions of ρ_{mix}, η_{mix}, λ_{mix}, and $c_{p,mix}$ for Ar-He gas mixtures between pure Ar and pure He are depicted in Figure 2-6. The specific values of the four gases, which are relevant for this dissertation, are summarized in Table 1.

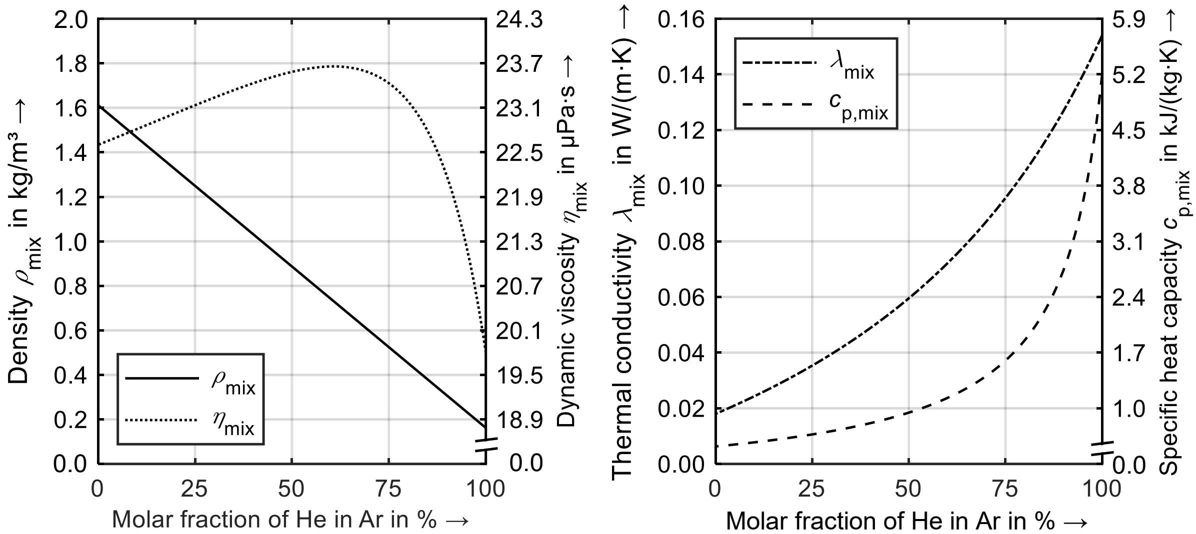

Figure 2-6: Gas properties for Ar-He gas mixtures between pure Ar and pure He (values for pure Ar and pure He taken from VDI E.V. (2013))

Table 1: Gas properties of Ar, He, and ArHe30/70 (70/30 vol.-% Ar + 30/70 vol.-% He) at standard conditions (temperature: 25 °C, pressure: 1 bar); values for pure Ar and pure He taken from VDI E.V. (2013)

Gas	**Density ρ_{mix} in kg/m³**	**Dynamic viscosity η_{mix} in µPa·s**	**Thermal conductivity λ_{mix} in W/(m·K)**	**Specific isobaric heat capacity $c_{p,mix}$ in kJ/(kg·K)**
Ar	1.612	22.6	0.018	0.520
ArHe30	1.177	23.2	0.039	0.712
ArHe70	0.597	23.6	0.087	1.405
He	0.162	19.8	0.154	5.193

2.3.3 Anemometry

The determination of the velocity and direction of a gas flow is referred to as anemometry. Depending on the application, different anemometers are used. They are categorized depending on the physical principle that is applied to measure the gas flow. For precise measurements of the gas flow velocity and directions in the field of fluid mechanics, oftentimes laser-doppler anemometers or hot-wire anemometers (HWA) are used. In other industrial applications, such as the design of ventilation systems, two other types of anemometers are widely used: a vane anemometer (VA) and a pitot static tube. When measuring with a VA, the kinetic energy of the gas flow is transferred into a rotational movement of the low mass impeller of the device. Its rotational speed is, thereby, proportional to the gas flow velocity. For minor differences in the density, pressure, and temperature of the gas, and for maximum flow vector misalignments of

20°, a VA can be used without calibration. However, if large differences in the density ρ occur, the measured velocity u_{m} needs to be calibrated according to

$$u_{\mathrm{c}} = u_{\mathrm{m}} \cdot \sqrt{\frac{\rho_{\mathrm{m}}}{\rho_{\mathrm{c}}}}, \tag{9}$$

with the indizes c and m for the calibration and measurement conditions, respectively (SIREN ET AL. 2001).

2.4 Selected basics of fluid flow and heat transfer

2.4.1 Gas flow characteristics and drag force

Gas flow characterization

In the PBF-LB/M process, a laminar gas flow inside the build chamber is desired. This enables a proper removal of process by-products and, thus, ensures an unhindered energy input by the laser. In a simplified two-dimensional consideration, a gas flow over a smooth or rough surface can be categorized into three flow regimes: laminar, laminar-turbulent transition, and turbulent. The categorization is made by calculating the Reynolds number *Re* of the flow according to

$$Re = \frac{\rho_{\mathrm{g}} \cdot L \cdot u_{\mathrm{g}}}{\eta_{\mathrm{g}}}, \tag{10}$$

with the gas density ρ_{g}, the characteristic length L, the gas flow velocity u_{g}, and the dynamic gas viscosity η_{g} (SCHLICHTING, H., GERSTEN, K. 2006). Above a critical Reynolds number

$$Re_{\mathrm{crit}} = 10^5 \text{ to } 3 \cdot 10^6, \tag{11}$$

the flow becomes fully turbulent. The application-specific Re_{crit} highly depends on the surface roughness of the substrate and the inlet flow. In typical PBF-LB/M machines, *Re* is smaller than Re_{crit} and a laminar gas flow regime is realized. A laminar flow is characterized by the absence of turbulences in the boundary layer of the flow. The boundary layer is the region between the solid substrate and the fully developed flow, where the viscosity of the flow leads to friction-induced impulse transport from the fluid to the substrate and, thus, a resulting shear stress. This influences the velocity profile of the flow perpendicular to the flow direction, as the adhesion condition requires the flow velocity to be zero at the contact point between the fluid and the substrate. Between this contact point and the fully developed flow further away, the velocity profile develops according to Figure 2-7.

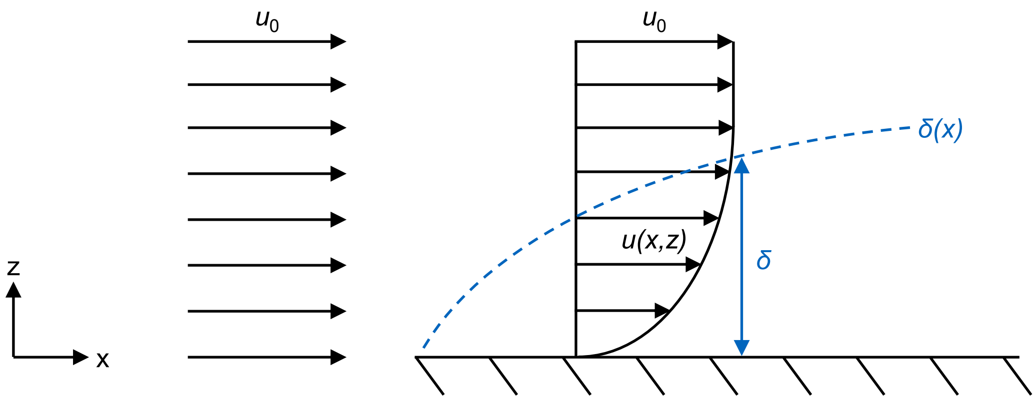

Figure 2-7: Velocity profile u(x,z) and boundary layer thickness profile δ(x) in a laminar flow over a flat surface; u_0: initial free flow velocity, δ: boundary layer thickness (own representation based on SCHLICHTING, H., GERSTEN, K. (2006))

The boundary layer thickness δ is described as the height, at which the flow velocity has reached 99 % of the velocity outside of the boundary layer. For a two-dimensional, stationary laminar flow with constant physical properties, δ can be calculated according to

$$\delta = \frac{5 \cdot L}{\sqrt{Re}}. \tag{12}$$

Equation 12 is derived from the continuity and the Navier-Stokes equations. For further details on the derivation, the reader is kindly referred to SCHLICHTING, H., GERSTEN, K. (2006).

Particle pickup velocity

In the PBF-LB/M process, the gas flow velocity has to be set high enough to ensure a sufficient removal of process by-products. However, if the velocity is chosen too high, there is a risk of blowing away the powder bed as a consequence of the shear stress in the boundary layer described above. KALMAN ET AL. (2005) and SHEN ET AL. (2020) proposed a step-wise model to calculate this gas- and powder-specific particle pickup velocity u_{pu}, above which the powder bed starts to be blown away. Their model is based on the Archimedes number $Arch$[1], which accounts for the ratio between the buoyancy and the friction force, and the particle Reynolds number Re_p. The particle pickup velocity u_{pu} can be determined by

$$u_{pu} = \frac{Re_p \cdot \eta_g}{d_p \cdot \rho_g \cdot K_D}, \tag{13}$$

with the powder particle diameter d_p. K_D is a modification factor for the flow profile and is set depending on the application. Re_p is calculated stepwise according to

$$Re_p = \begin{Bmatrix} \text{(I)} & 5 \cdot Arch^{3/7} & \text{for} & Arch \geq 16.5 \\ \text{(II)} & 16.7 & \text{for} & 0.45 < Arch < 16.5 \\ \text{(III)} & 21.8 \cdot Arch^{1/3} & \text{for} & Arch \leq 0.45 \end{Bmatrix}. \tag{14}$$

[1] Usually, the abbreviation *Ar* is applied for the Archimedes number in literature. However, as these two letters are used for the gas argon in this work, the abbreviation *Arch* was introduced to avoid misunderstandings.

The Archimedes number $Arch$ can be determined via the particle density ρ_p, the gravitational acceleration g, and the particle shape modification factor K_Φ by

$$Arch = \frac{g \cdot \rho_g \cdot (\rho_p - \rho_g) \cdot d_p^3}{\eta_g^2 \cdot K_\Phi}. \tag{15}$$

The stepwise calculation of Re_p considers the increasing influence of interparticular forces leading to cohesion towards small particle diameters (III). For larger particle diameters, gravitational forces dominate and withstand the blowing force by the gas flow (I).

Drag force on a particle in a gas flow

The trajectory of a powder particle, which was separated from the powder bed due to an exceedance of u_{pu}, or of a spatter particle are affected by a drag force coming from the gas flow. This drag force F can be calculated in a simplified manner for spherical particles according to the Stokes equation:

$$F = \frac{1}{2} \cdot c_w \cdot \rho_g \cdot A_p \cdot u_g^2. \tag{16}$$

The particle surface A_p is calculated by

$$A_p = \left(\frac{d_p}{2}\right)^2 \cdot \pi. \tag{17}$$

The calculation of the drag coefficient c_w depends on whether or not gravitational forces can be neglected in the specific use case.

2.4.2 Heat transfer

During the PBF-LB/M process, a liquid metal melt pool is created, which transfers heat into its surroundings. The three transport mechanisms of heat transfer, depicted in Figure 2-2, are conduction, convection, and radiation. On the upper melt pool boundary towards the gas atmosphere, heat is mainly transferred by radiation and convection. In the direction of the underlying solidified material, heat transfer by conduction is dominant. Besides the melt pool, also the spatters experience rapid temperature changes during their flight caused by radiative and convective cooling. In both cases, the resulting total heat flux $\dot{Q}_{total}$ can be expressed as

$$\dot{Q}_{total} = \dot{Q}_{cond} + \dot{Q}_{conv} + \dot{Q}_{rad}, \tag{18}$$

with the conductive contribution $\dot{Q}_{cond}$, the convective contribution $\dot{Q}_{conv}$, and the radiative contribution to the heat transfer $\dot{Q}_{rad}$. In the following paragraphs, the governing equations for the heat transfer phenomena are described. For the detailed description and calculation of the varying heat transfer phenomena, the reader is kindly referred to (BAEHR & STEPHAN 2011).

Heat transfer by conduction

For a stationary one-dimensional case of heat conduction through an even and homogeneous wall, the resulting heat flux $\dot{Q}_{\mathrm{cond}}$ is defined by Fourier's law as

$$\dot{Q}_{\mathrm{cond}} = \lambda_{\mathrm{w}} \cdot A_{\mathrm{w}} \cdot \frac{\Delta T}{d_{\mathrm{w}}}, \tag{19}$$

whereby λ_{w} is the thermal conductivity of the wall material, A_{w} is the wall surface, ΔT is the temperature difference, and d_{w} is the wall thickness. Since, in many real applications, heat transfer by conduction is a three-dimensional and time-dependent phenomenon, a differential equation for the unsteady heat conduction is necessary. In cartesian coordinates, this differential equation is given by

$$\frac{\partial T}{\partial t_{\mathrm{c}}} = a \cdot \left[\frac{\partial^2 T}{\partial x^2} + \frac{\partial^2 T}{\partial y^2} + \frac{\partial^2 T}{\partial z^2}\right] \pm \frac{\dot{q}}{\rho \cdot c_{\mathrm{p}}}, \tag{20}$$

with the time t_{c}, the thermal diffusivity a, and the heat flux density $\dot{q}$ (GRIESINGER 2019). The thermal diffusivity a_{w} is related to λ_{w} by

$$a_{\mathrm{w}} = \frac{\lambda_{\mathrm{w}}}{\rho \cdot c_{\mathrm{p}}}. \tag{21}$$

Heat transfer by convection

The heat flux by convection $\dot{Q}_{\mathrm{conv}}$ can be calculated by

$$\dot{Q}_{\mathrm{conv}} = \alpha \cdot A \cdot \Delta T, \tag{22}$$

with the heat transfer coefficient α and the exposed surface area A. The heat transfer coefficient α is calculated with the dimensionless Nusselt number Nu by

$$\alpha = \frac{Nu \cdot \lambda_{\mathrm{g}}}{L}. \tag{23}$$

To account for both convection phenomena, natural and forced convection, the respective Nusselt numbers Nu_{forced} and Nu_{natural} are considered using the following equation:

$$Nu = \sqrt[3]{Nu_{\mathrm{forced}}^3 + Nu_{\mathrm{natural}}^3}\,. \tag{24}$$

In the case of forced convection, the Nusselt number Nu_{forced} is calculated using the dimensionless Prandtl number Pr and Re ($Nu_{\mathrm{forced}} = \mathrm{f}(Re, Pr)$). For the calculation of Nu_{natural}, the dimensionless Rayleigh number Ra and Pr are used ($Nu_{\mathrm{natural}} = \mathrm{f}(Ra, Pr)$).

Heat transfer by radiation

The heat transfer by radiation $\dot{Q}_{\mathrm{rad}}$ for a non-blackbody radiator is formulated as

$$\dot{Q}_{\mathrm{rad}} = \varepsilon(\lambda) \cdot \sigma_{\mathrm{B}} \cdot A_{\mathrm{O}} \cdot T^4, \tag{25}$$

with the spectral emission coefficient $\varepsilon(\lambda)$, the surface of the object A_{O}, and the Stefan-Boltzmann constant σ_{B}.

2.5 Process monitoring systems

2.5.1 General remarks

Depending on their position relative to the laser beam path, process monitoring systems for PBF-LB/M can be divided into on-axis and off-axis systems. On-axis systems are coupled into the laser beam path in such a way that the sensor detects information from a position around the laser spot. In contrast, off-axis systems are located for observation anywhere around the processing zone. An overview of typical process monitoring systems for PBF-LB/M with exemplary applications is given in Table 2. Due to their relevance for this dissertation, only the methods of pyrometry and Schlieren imaging are described in detail in the following subsections.

Table 2: Overview of typical process monitoring methods for PBF-LB/M

Position	Method	Exemplary goal of investigation
Off-axis	Schlieren imaging Thermography Computational tomography (CT)	Evaporation phenomena Melt pool cooling Creation of pores
On-axis	Pyrometry High-speed imaging	Melt pool temperature Spatter tracking

2.5.2 Schlieren imaging

Optical deflections in inhomogeneous media

In a gaseous medium, the interaction of light with gases of a changing refractive index n_{g} influences the speed of light propagation within the medium c according to

$$n_{\mathrm{g}} = \frac{c_0}{c}, \tag{26}$$

with the speed of light in vacuum c_0 (SETTLES 2001). The refractive index of gases linearly relates to the gas density ρ_{g} by

$$n_{\mathrm{g}} - 1 = k \cdot \rho_{\mathrm{g}}. \tag{27}$$

The Gladstone-Dale coefficient k is used in Equation (27) and has a value of 0.23 cm^3/g for air at standard conditions (temperature: 25 °C, pressure: 1 bar) and varies from 0.10 to 1.50 cm^3/g for other gases (SETTLES 2001). Inhomogeneities in the path of the light beam can occur due to various reasons, such as caused by a temperature change. In the case of PBF-LB/M, this can be of particular benefit for process monitoring, as the atmosphere close to the process zone is an area of different gaseous media with varying temperatures and, thus, densities. The process gas, which enters the build chamber near room temperature, is heated up in areas close to the melt pool due to convective and radiative heat transfer. Furthermore, evaporated metal alloy components leave the melt pool as a gaseous jet stream. The hot spatters ejected from the melt pool can also heat up their surrounding atmosphere. The different temperatures of the media lead to areas of varying densities according to the ideal gas equation at or near atmospheric conditions

$$\frac{p}{\rho} = R \cdot T, \tag{28}$$

with the pressure p and the universal gas constant R. If a ray of light travels through and is refracted by such an inhomogeneity with a gradient in the refractive index, its resulting 2D ray curvature is given by (SETTLES 2001)

$$\frac{\partial^2 x}{\partial y^2} = \frac{1}{n_\mathrm{g}} \cdot \frac{\partial n_\mathrm{g}}{\partial x} \text{ and } \frac{\partial^2 z}{\partial y^2} = \frac{1}{n_\mathrm{g}} \cdot \frac{\partial n_\mathrm{g}}{\partial z}. \tag{29}$$

In a 2D setup, the resulting deflection angles of the rays of light over a test section with the length L_test in the x- and in the z-direction ε_x and ε_z, respectively, can each be obtained by a single integration of Equation (29) according to

$$\varepsilon_\mathrm{x} = \frac{1}{n_\mathrm{g}} \cdot \int_0^{L_\mathrm{test}} \frac{\partial n_\mathrm{g}}{\partial x} dy = \frac{L_\mathrm{test}}{n_0} \cdot \frac{\partial n_\mathrm{g}}{\partial x} \text{ and} \tag{30}$$

$$\varepsilon_\mathrm{z} = \frac{1}{n_\mathrm{g}} \cdot \int_0^{L_\mathrm{test}} \frac{\partial n_\mathrm{g}}{\partial z} dy = \frac{L_\mathrm{test}}{n_0} \cdot \frac{\partial n_\mathrm{g}}{\partial z}, \tag{31}$$

with the refractive index of the surrounding medium n_0 (SETTLES 2001). In many real applications, these angles are usually quite small in the order of magnitude of 10^{-6} to 10^{-3} radians. In an experimental study by CHENG ET AL. (2020), for example, where a linear Schlieren setup was applied with air as the surrounding medium, deflection angles in the order of magnitude of $4 \cdot 10^{-4} - 7 \cdot 10^{-4}$ radians were observed. Therefore, the small angle approximation can be applied when describing the image analysis.

Schlieren imaging analysis

Schlieren imaging is an optical process monitoring method that allows visualizations of density differences in transparent media. In practical applications, the effects can be visualized in the most straightforward manner in a linear Schlieren imaging setup (see Figure 2-8) (SETTLES 2001). A light beam bundle from an ideal point light source with the diameter d_s is collimated using a convex lens (L_1). If one of these collimated light beams reaches a second convex lens (L_2) unhindered, it is focused in the focal point of the lens (solid lines). However, if one of these light beams travels through an area of a varying refractive index (test section) between the two lenses, it is deflected and, thus, will not reach the focal point of the second convex lens L_2 (dashed line). When a cut-off (knife-edge) is placed in the focal point of L_2, and a screen is placed at the conjugate focus of the test section, then a sharp upside-down image of various greyscales will appear on that screen. The appearance of this image depends on the number of light beams being deflected or not, and on the shape and size of the cut-off.

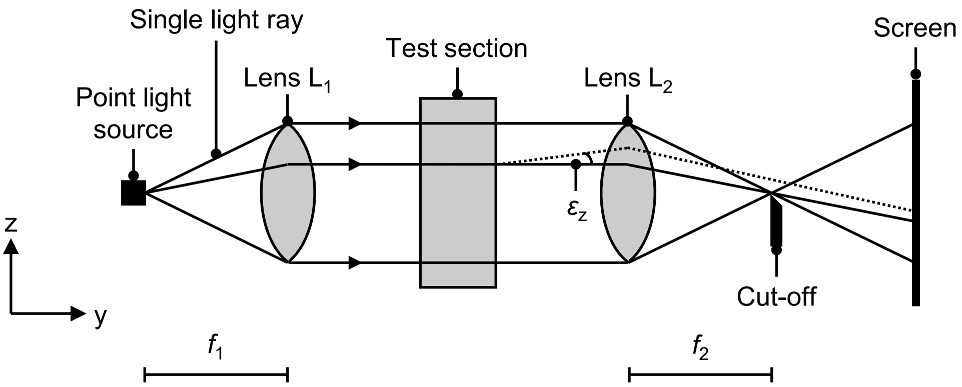

Figure 2-8: Basic principle of Schlieren imaging demonstrated on a linear Schlieren imaging setup; n: refractive index, $f_{1,2}$: focal lengths of $L_{1,2}$ (own representation based on PANIGRAHI & MURALIDHAR (2012))

Figure 2-9 shows a detailed schematic view on the optical situation at the cut-off. An undisturbed light beam reaches the cut-off in the focal point of L_2 with the diameter d_0, which is related to d_s by

$$\frac{d_0}{d_\mathrm{s}} = \frac{f_2}{f_1}, \tag{32}$$

with the focal lengths f_1 and f_2 of the lenses L_1 and L_2, respectively. If no cut-off is present, the screen is illuminated by the illumination I_0. The illumination I_k, which appears on the screen when a cut-off is properly positioned at the focal point of L_2, is related to I_0 according to (PANIGRAHI & MURALIDHAR 2012)

$$I_\mathrm{k} = \frac{d_\mathrm{k}}{d_0} \cdot I_0. \tag{33}$$

The diameter d_k represents the remaining dimension of an undisturbed light beam, when a certain amount of it is cut-off.

When the light beam is deflected by an inhomogeneity with a certain angle ε_z, its displacement Δd in the z-direction can be expressed by

$$\Delta d = f_2 \cdot \varepsilon_\mathrm{z}, \tag{34}$$

using the small angle approximation. The illumination I_f, which remains on the screen after deflection, is, thus, given by (PANIGRAHI & MURALIDHAR 2012)

$$I_\mathrm{f} = I_\mathrm{k} \cdot \frac{d_\mathrm{k} + \Delta d}{d_\mathrm{k}} = I_\mathrm{k} \cdot \left(1 + \frac{\Delta d}{d_\mathrm{k}}\right). \tag{35}$$

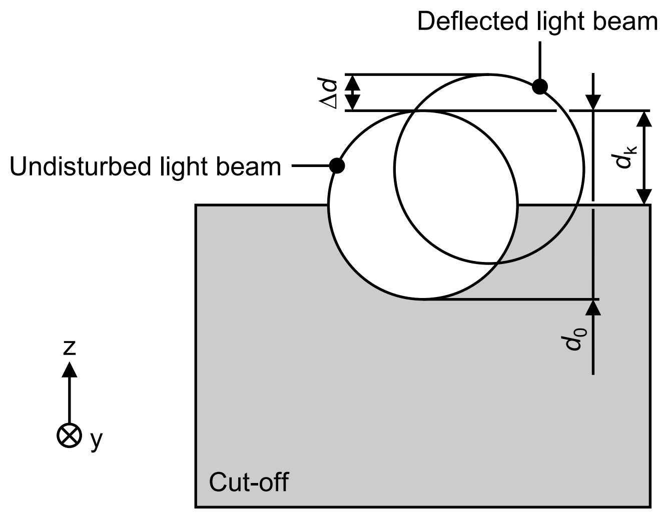

Figure 2-9: Detailed schematic view on the optical situation at a cut-off in a Schlieren imaging setup describing the impact areas of an undisturbed and a deflected light beam (own representation based on PANIGRAHI & MURALIDHAR (2012))

Finally, considering the change in the light intensity $\Delta I = I_f - I_k$, the contrast produced by the Schlieren imaging setup (i.e., the difference between light and dark areas of the image) can be expressed by

$$\text{contrast} = \frac{\Delta I}{I_\text{k}} = \frac{\Delta d}{d_\text{k}} = \frac{f_2 \cdot \varepsilon_\text{z}}{d_\text{k}}. \tag{36}$$

For practical applications, Equation 36 shows that the contrast is directly related to f_2. Larger values of f_2, therefore, lead to a greater sensitivity of the setup. (PANIGRAHI & MURALIDHAR 2012)

2.5.3 Pyrometry

Thermal radiation

Every physical body emits electromagnetic radiation, which is referred to as thermal radiation. This radiation depends on the emissivity and the temperature of the body. Below approximately 3800 K, the maximum of the thermal emission lies in the infrared spectral range with wavelengths ranging from 0.78 µm to 40 µm. The basics of its propagation are described by Maxwell's equations. Various radiation laws describe the creation and properties of thermal radiation. The most relevant laws are described in the following. For further details, the reader is kindly referred to the work of BUDZIER & GERLACH (2023).

The laws of Planck and Stefan-Boltzmann describe the creation of thermal radiation, while Wien's displacement law and Kirchhoff's law for thermal radiation define the properties of thermal radiation. Planck's law defines the specific spectral radiation $M(\lambda,T)$ as

$$M(\lambda, T) = \frac{c_1}{\lambda^5} \cdot \frac{1}{e^{\frac{c_2}{\lambda \cdot T}} - 1}. \tag{37}$$

$M(\lambda,T)$ is defined as the radiation flux Φ that an area element dA emits. The radiation constants c_1 and c_2 were determined to be

$$c_1 = 2 \cdot \pi \cdot c_0^2 \cdot h_P = 3.741832 \cdot 10^{-16}\,\mathrm{W} \cdot \mathrm{m}^2 \text{ and} \tag{38}$$

$$c_2 = \frac{c_0 \cdot h_P}{\sigma_B} = 1.438786 \cdot 10^{-2}\ \mathrm{K} \cdot \mathrm{m}, \tag{39}$$

with Planck's quantum of action h_P. Bodies that emit thermal radiation according to Planck's law are defined as black-body radiators. According to the theory of Planck, a black-body radiator is an ideal radiator that absorbs all radiation and emits the maximum specific spectral radiation at all wavelengths. Figure 2-10 illustrates the spectral specific radiation depending on λ and T. The individual curves of $M(\lambda,T)$ never intersect, which means that $M(\lambda,T)$ increases for all λ with an increasing T. This enables the assignment of the thermal radiation to the temperature of the body.

Besides $M(\lambda,T)$, which describes the specific spectral radiation into the half-space, the spectral radiance $L(\lambda,T)$ is often used in pyrometry setups. It defines the radiation flux Φ per area element in the normal direction and per unit solid angle Ω according to

$$L(\lambda, T) = \frac{c_1}{\pi \cdot \Omega \cdot \lambda^5} \cdot \frac{1}{e^{\frac{c_2}{\lambda \cdot T}} - 1}. \tag{40}$$

Wien's displacement law describes the situation that the maximum of $M(\lambda,T)$ at λ_{max} shifts towards lower values of λ with an increasing T. Thus, the product of λ_{max} and T remains constant according to

$$\lambda_{max} \cdot T = 2897.8\ \mathrm{K} \cdot \mu\mathrm{m}. \tag{41}$$

The graph of Wien's displacement law is marked in Figure 2-10.

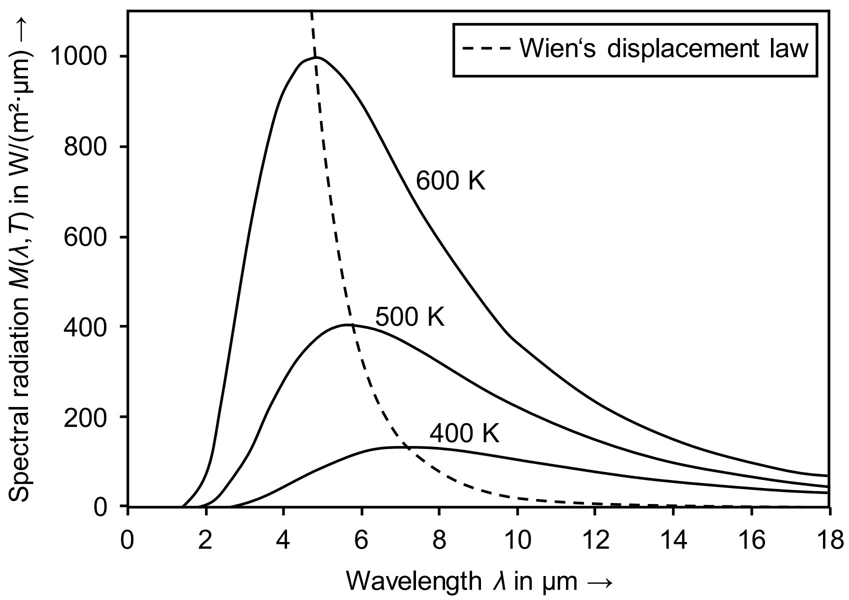

Figure 2-10: Course of the specific spectral radiation M(λ,T) depending on the wavelength λ and the temperature T; the dashed line characterizes Wien's displacement law (own representation based on GENGENBACH (2007))

To determine the specific spectral radiation for a certain wavelength range $\Delta\lambda = \lambda_2 - \lambda_1$, Equation (37) needs to be integrated over $\Delta\lambda$:

$$M(T) = \int_{\lambda_1}^{\lambda_2} \frac{c_1}{\lambda^5} \cdot \frac{1}{e^{\frac{c_2}{\lambda \cdot T}} - 1} \, d\lambda \,. \tag{42}$$

The Stefan-Boltzmann law provides the only known solution to this equation for the whole wavelength range from $\lambda_1 = 0$ to $\lambda_1 = \infty$. For this wavelength range, Equation (42) transforms to

$$M(T) = \sigma \cdot T^4. \tag{43}$$

If $M(T)$ or $L(T)$ shall be calculated for a real body rather than a black-body radiator, the equations (37) and (40) need to be multiplied by the spectral emission coefficient $\varepsilon(\lambda)$. The emission coefficient can be defined as the ratio between the specific spectral radiations of the real body to be measured and a black body $M_{\mathrm{RB}}(T)$ and $M_{\mathrm{BB}}(T)$, respectively, at the same temperatures according to

$$\varepsilon(\lambda) = \frac{M_{\mathrm{RB}}(T)}{M_{\mathrm{BB}}(T)}. \tag{44}$$

For a black body, $\varepsilon(\lambda)$ equals to 1. Since most bodies emit less radiation at the same temperature than a black body, gray and real bodies are defined. If the emitted radiation is a fraction of that emitted by a black body and independent of λ, the term gray body is used ($0 < \varepsilon(\lambda) < 1$, $\varepsilon(\lambda) = \text{constant}$). If the fraction is, additionally, dependent on λ, the designation real body applies ($0 < \varepsilon(\lambda) < 1$, $\varepsilon(\lambda) = \text{variable}$). Figure 2-11 exemplarily shows these differences by the courses of $M(\lambda)$ for the three bodies at a temperature of 600 K.

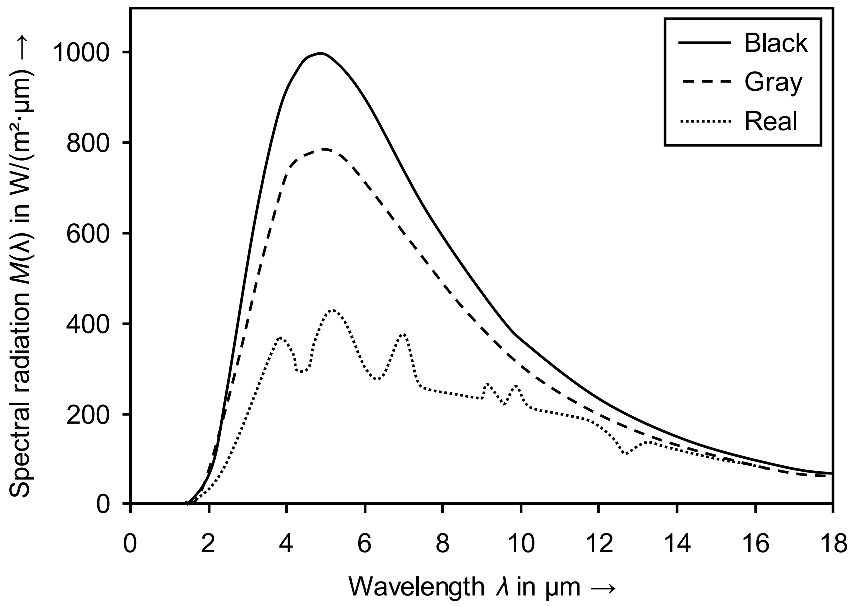

Figure 2-11: Comparison of black, gray, and real bodies by the courses of their specific spectral radiation M(λ) at a fixed temperature of 600 K (own representation based on GRIESINGER (2019))

As described in Equation 1 for PBF-LB/M, the laser beam can either be absorbed or reflected and the sum of the coefficients $\alpha(\lambda)$ and $\rho(\lambda)$, respectively, equals to one. In general, besides absorption and reflection, any radiation that hits a non-opaque body can also be transmitted with the transmission coefficient $\tau(\lambda)$. In this case, Equation 1 modifies to (HÜGEL & GRAF 2009)

$$\alpha(\lambda) + \rho(\lambda) + \tau(\lambda) = 1. \tag{45}$$

In a black body, $\rho(\lambda)$ and $\tau(\lambda)$ are zero and, according to Kirchhoff's law for thermal radiation, $\alpha(\lambda) = \varepsilon(\lambda)$.

Measuring principle of a two-color pyrometer

Figure 2-12 depicts a general setup of pyrometer measurements. Before the radiation reaches the sensor of the pyrometer, it passes along the transmission path as well as through the imaging system. In the case of PBF-LB/M, the transmission path is typically the gas atmosphere above the melt pool, which can be comprised of inert gas, metal vapor and spatters.

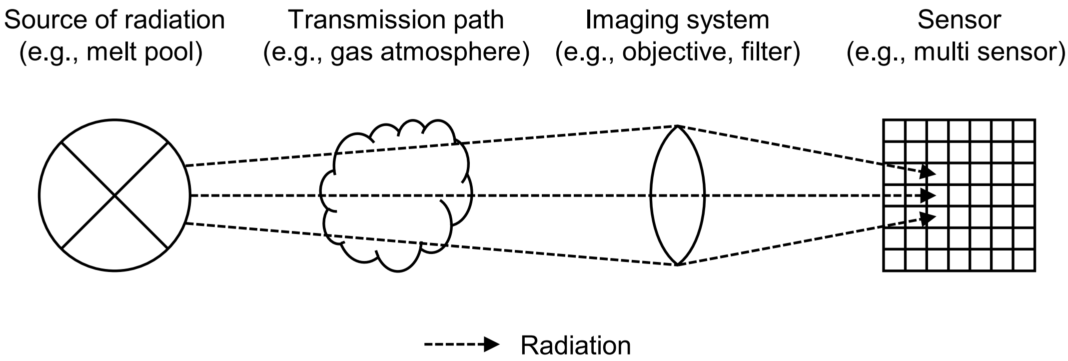

Figure 2-12: Schematic representation of pyrometry measurement setups (own representation based on BUDZIER & GERLACH (2023))

In a two-color pyrometry setup, the temperature of the object T_O is measured by the ratio of two spectral radiances. These two spectral radiances are captured in two individual measuring channels, which are each built as spectral pyrometers. In a spectral pyrometer, the output signal S_A of the pyrometer is given by

$$S_A = R_S \cdot A_S \cdot L_O \cdot \pi \cdot \sin^2\left(\frac{FOV}{2}\right), \tag{46}$$

with the sensitivity and surface of the pyrometer sensor R_S and A_S, respectively, the spectral radiance of the object L_O, and the field of view of the pyrometer FOV. A spectral pyrometer determines the radiation flux in a narrow wavelength range. When L_O from Equation (40) is multiplied by ε_O to account for a real body and inserted into Equation (46), the latter can be rearranged according to the temperature. By neglecting the influence of the ambient temperature T_∞ ($T_O >> T_\infty$), the temperature of the object T_O can then be determined by

$$T_O = \frac{c_2}{\lambda_e} \cdot \frac{1}{\ln\left(\varepsilon_O \cdot \frac{F_S}{S_A} + 1\right)}. \tag{47}$$

The term F_S accounts for the system parameters and constants according to

$$F_{\mathrm{S}} = A_{\mathrm{S}} \cdot R_{\mathrm{S}} \cdot \frac{\Delta\lambda_{\mathrm{e}} \cdot c_1}{\lambda_{\mathrm{e}}^5} \cdot \sin^2\left(\frac{FOV}{2}\right), \tag{48}$$

with the real wavelength λ_e. For a very narrow wavelength range between λ_1 and λ_2, λ_e can be approximated by

$$\lambda_{\mathrm{e}} = \frac{\lambda_1 + \lambda_2}{2}. \tag{49}$$

As it is described in the equations above, the emission coefficient $\varepsilon(\lambda, T)$ must be known for real temperature measurements. In the case of PBF-LB/M, however, this poses a major challenge as $\varepsilon(\lambda, T)$ highly depends on the temperature and the surface condition (e.g., solid versus liquid, oxidized versus non-oxidized). For this purpose, two-color pyrometers are applied. These systems enable temperature measurements without knowledge of $\varepsilon(\lambda, T)$ by measuring the radiance L at two wavelengths λ_1 and λ_2. The signal ratio S_R equals to

$$S_{\mathrm{R}} = \frac{\varepsilon(\lambda_1)}{\varepsilon(\lambda_2)} \cdot \frac{L_{\lambda_1}}{L_{\lambda_2}} = \frac{\varepsilon(\lambda_1)}{\varepsilon(\lambda_2)} \cdot \frac{\lambda_1^{-5}}{\lambda_2^{-5}} \cdot \frac{e^{\frac{-c_2}{\lambda_1 \cdot T_{\mathrm{O}}}}}{e^{\frac{-c_2}{\lambda_2 \cdot T_{\mathrm{O}}}}} = \frac{\varepsilon(\lambda_1)}{\varepsilon(\lambda_2)} \cdot \left(\frac{\lambda_2}{\lambda_1}\right)^5 \cdot e^{\frac{-c_2}{\lambda_{\mathrm{V}} \cdot T_{\mathrm{O}}}}, \tag{50}$$

with the wavelength ratio λ_V given by

$$\frac{1}{\lambda_{\mathrm{V}}} = \frac{1}{\lambda_1} - \frac{1}{\lambda_2}. \tag{51}$$

When assuming that $\varepsilon(\lambda, T)$ is nearly constant within a certain temperature range ($\varepsilon(\lambda_1) \approx \varepsilon(\lambda_2)$), S_R only depends on the temperature T_O. As a consequence, T_O can be determined by rearranging Equation (50) to

$$T_{\mathrm{O}} = \frac{c_2}{\lambda_{\mathrm{V}}} \cdot \frac{1}{5 \cdot \ln\left(\frac{\lambda_2}{\lambda_1}\right) - \ln(S_{\mathrm{R}})}. \tag{52}$$

The error produced by the assumption of a nearly constant emission coefficient is exemplarily visualized in Figure 2-13 based on Equation (52) for a true temperature of an arbitrary object of T_O = 1000 °C. (BUDZIER & GERLACH 2023)

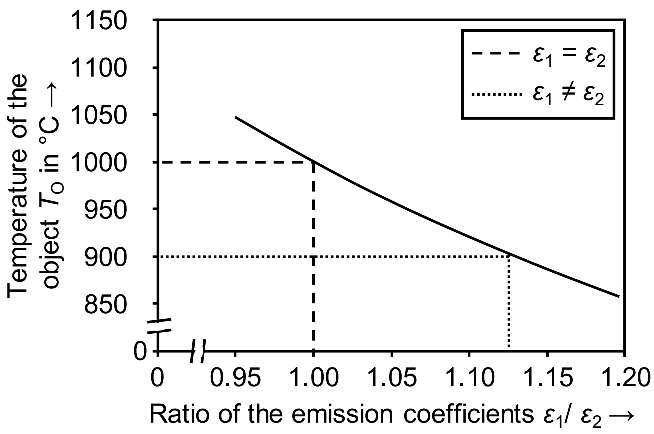

Figure 2-13: Influence of the ratio of the emission coefficients ε(λ_1) and ε(λ_2) on the detected temperature of the object for λ_1 = 1.4 µm and λ_2 = 1.7 µm (own representation based on BUDZIER & GERLACH (2023))

The solid line in Figure 2-13 depicts the object temperature T_O that the pyrometer shows depending on the ratio of the emission coefficients $\varepsilon(\lambda_1)/\varepsilon(\lambda_2)$ for λ_1 = 1.4 µm and λ_2 = 1.7. At a temperature of 1000 °C, the ratio equals 1 (dashed line). If $\varepsilon(\lambda_1)$ and $\varepsilon(\lambda_2)$ deviate from each other, the temperature that the pyrometer shows also changes. This is exemplarily shown by the dotted line in Figure 2-13, which depicts a deviation of the emission coefficients of about 12.5 %, leading to a displayed object temperature of only 900 °C. These deviations depend on the material used. Thus, for true temperature measurements, the emission coefficients must be known as accurately as possible.

3 State of the art

3.1 Chapter overview

Chapter 3 presents the state of the art on formation mechanisms as well as impacts of process by-products and how the gas flow and type affect the PBF-LB/M process. Relevant literature on related processes is focused on the process of laser beam welding, as this is considered as the most closely related process to PBF-LB/M. Section 3.2 describes the studies on process by-products. Within this section, their formation mechanisms and characteristics (Subsection 3.2.1), their impact on part properties, and hardware-based mitigation strategies (Subsection 3.2.2) are elaborated on. Section 3.3 is dedicated to the spatter effects during laser beam welding. In Section 3.4, the influences of the gas flow (Subsection 3.4.1) and type (Subsection 3.4.2) on the PBF-LB/M process are presented. An overview of relevant literature on process gas influences in related processes is given in Section 3.5. The chapter is concluded with an overview of relevant simulation techniques for the PBF-LB/M process in Section 3.6 and the derived need for action in Section 3.7.

3.2 Spatters during the powder bed fusion of metals using a laser beam

3.2.1 Formation mechanisms and characterization

SIMONELLI ET AL. (2015) experimentally investigated the characteristics of spatters produced during the PBF-LB/M of the materials[2] 1.4404, 3.2381, and 3.7164 under an Ar atmosphere. For all materials, the spatters collected from the powder bed after processing showed a spherical shape and were significantly larger in size (1.4404: 45 – 250 µm, 3.2381: 110 – 330 µm, 3.7164: 130 – 270 µm) than the mainly spherical virgin metal powders (1.4404: 5 – 50 µm, 3.2381: 30 – 50 µm, 3.7164: 15 – 70 µm). On the spatters from the materials 1.4404 and 3.2381, surface oxides were found. Otherwise, their chemical composition matched with that of the respective virgin metal powders. Regarding the spatter formation mechanism, the authors hypothesized that spatters are created due to the upwards separating of liquid metal in the rear area of the dynamic melt pool as a consequence of the vapor pressure resulting from the continuous evaporation of metal.

KHAIRALLAH ET AL. (2016) numerically studied the formation mechanisms of spatters during the PBF-LB/M process using the material 1.4404. No information on the applied gas phase was given. A three-dimensional high-fidelity model including the metal powder was set up and used

[2] For the most common materials used in the PBF-LB/M process, their designation is given according to the European standardization: 1.4404: 316L, 2.4668: IN718, 3.2381: AlSi10Mg, 3.7164: Ti6Al4V

to investigate spatter formation resulting from the highly dynamic melt pool. Two main mechanisms were identified. One describes the spatter formation in the bow wave of the melt pool ahead of the laser beam spot. This bow wave is created as a consequence of liquid metal that moves up the front of the penetration zone due to convective flows within the melt pool. In this highly dynamic area of the melt pool, liquid metal can be separated from the melt pool and ejected in the form of spatters. The second mechanism describes liquid metal being ejected vertically from the indentation area of the melt pool due to the strong vertical metal vapor jet. The spatters were described as small droplets. The authors discussed and concluded that deep and narrow melt pools should generally be avoided due to an increased risk of pore formation and spattering.

In an experimental study by WANG ET AL. (2017) on a cobalt-chromium powder processed via PBF-LB/M under an Ar atmosphere, the three mechanisms of spatter formation described by SIMONELLI ET AL. (2015) and KHAIRALLAH ET AL. (2016) were investigated. For this purpose, the spatters were collected after processing and studied regarding their size, shape, and chemical composition. Consistent with previous works, the average size of the spatters (132 µm) was higher than that of the virgin metal powder (32 µm). The spatters were distinguished by their shapes and, by that, each attributed to one of the three formation mechanisms. Spatters being ejected from the rear part of the melt pool, as they were hypothesized by SIMONELLI ET AL. (2015), were found to have a spherical shape with some satellite particles adhering to their surface. These stick to the spatter surface when the hot, solidified spherical spatter lands in the powder bed. Spatters being ejected vertically from the indentation zone of the melt pool were found to have a spherical shape with a smooth surface, as they had enough time for solidification and cooling. The spatters being created by the mechanism described by KHAIRALLAH ET AL. (2016) showed irregular shapes with coarse surfaces. These result when liquid metal from the bow wave splashes onto the powder bed and creates agglomerates. The chemical composition was found to be mainly consistent with the virgin metal powder with a slight increase in the oxygen content. Another result from this study showed that spattering depends on the energy input. With a higher energy input, more spatters occurred.

The experimental studies of ANDANI ET AL. (2017), ANDANI ET AL. (2018), and LUTTER-GÜNTHER ET AL. (2018) delivered similar results to the previous works. In the work of ANDANI ET AL. (2017), the influence of a multi-laser PBF-LB/M process with the material 3.2381 under an Ar atmosphere on the spattering was investigated. Similar spatter formation mechanisms as described by WANG ET AL. (2017) were proposed. The driving forces for spatter creation were found to be even stronger in the multi-laser process than in the single-laser process. In a second study with the material 3.2381 in a single-laser PBF-LB/M process from ANDANI ET AL. (2018), the isolated effects of varying laser powers and scanning velocities were investigated. The results showed that decreasing the laser power or increasing the scanning velocity led to less spattering. Changing the scanning velocity had a stronger influence than a change in the laser power. LUTTER-GÜNTHER ET AL. (2018) studied and characterized the emerging spatters during the PBF-LB/M of the material 3.2381 under an Ar atmosphere. Spherical as well as agglomerated spatters with an average size of 140.1 µm and maximum sizes of up to 300 µm were found (average size of the virgin metal powder: 48.9 µm). The oxygen content in the spatters was nearly tripled compared to the virgin metal powder.

BIDARE ET AL. (2018a) presented an in-depth study on the fluid and particle dynamics during the PBF-LB/M with the material 1.4404. Experimental investigations using Schlieren and high-speed imaging on a custom PBF-LB/M machine, which was previously presented by BIDARE ET AL. (2017), were combined with a multi-physics simulation model. The results of the study confirmed the upwards ejection of spatters due to the aerodynamic drag of the metal vapor jet. This effect became especially evident when the simulation results were studied. It was shown that the metal vapor jet propagated into the atmosphere with a velocity of several hundreds of meters per second, accelerating the surrounding gas phase and entraining not only the spatters, but also metal powder particles close to the melt pool. As the temperature of the jet was found to be higher than 3500 K, the authors discussed potential melting and vaporization of the spatters during their flight.

Additional in-depth insights into spatter formation mechanisms and spatter characteristics in the PBF-LB/M process under an Ar atmosphere were given by GUO ET AL. (2018), CHEN & YAN (2020), and OBEIDI ET AL. (2020). GUO ET AL. (2018) applied X-ray imaging to the processing of the materials 1.4404 and 3.2381. Consistent with the study of BIDARE ET AL. (2018a), it was found that the spatters entrained by the metal vapor jet exhibited the highest velocities. Within this study, these velocities were found to be three times as high as the velocities of spatters, which were ejected from the rear area of the melt pool and accelerated by the Ar gas flow. The numerical study by CHEN & YAN (2020) on the material 1.4404 unveiled similar findings on the vapor jet velocity and temperature as well as the acceleration of spatters and surrounding metal powder particles. OBEIDI ET AL. (2020) delivered additional and consistent results on the shapes, sizes, and chemical compositions of spatters in their experimental study with the material 1.4404.

In the experimental study of YOUNG ET AL. (2020) on the processing of the materials 3.2381 and 3.7164 via PBF-LB/M under an Ar atmosphere, two further types of spatters were described in contrast to the previously presented studies: solid spatters and defect-induced spatters. One additional type of spatters results from the entrainment of metal powder particles due to the aerodynamic drag of the metal vapor jet, as already hinted by BIDARE ET AL. (2018a). The latter type originates from the interactions between the laser beam and defects from the previous layers. These can lead to spontaneous and violent eruptions of liquid metal and, thus, spattering. Consistent to previous studies, the spatters being entrained by the metal vapor jet exhibited the highest velocities, while the agglomerated spatters exhibited the largest sizes.

Further studies were published on this topic, delivering more detailed information on formation mechanisms and spatter characteristics. WANG ET AL. (2021), for example, correlated different spatter types to the energy input during the PBF-LB/M. LI ET AL. (2023) further discussed the entrainment of spatters and metal powder particles by the metal vapor jet. However, the underlying physical mechanisms described before held valid in these studies.

Interim conclusion

Over the past years, several studies investigated spatter formation mechanisms as well as the shapes and sizes of spatters. Depending on their formation mechanism, five different types of spatters have been identified over the years. The three most prominently studied types are spatters being ejected at the front of the melt pool creating large irregular-shaped agglomerates, mostly spherical spatters being ejected at the rear part of the melt pool, and fine spherical spatters being entrained and accelerated by the metal vapor jet resulting from the keyhole. The maximum spatter sizes were found to be about one order of magnitude larger than the particle sizes of virgin metal powder. During their flight in the ambient atmosphere, spatters can pick up oxygen. This became evident during measurements of their chemical compositions, where increased oxygen contents were found while the remaining composition was similar to the respective virgin metal powder. The metal vapor jet of evaporated material was found to reach a velocity of several hundreds of meters per second, leading to the upwards momentum of the melt pool flow and, thus, spattering. Schlieren and high-speed imaging have shown to be promising experimental methods to study process by-products in the PBF-LB/M process.

3.2.2 Impact on the process and part properties as well as mitigation strategies

Impact on the process and part properties

LUTTER-GÜNTHER ET AL. (2018) experimentally investigated the influence of spatters on the powder bed quality during PBF-LB/M of the material 3.2381 under an Ar atmosphere. Although the average spatter size was found to be larger than that of the virgin metal powder (cf. Subsection 3.2.1), a significant number of spatters fell through the sieve in the powder sieving process. This effect enhances metal powder feedstock degradation, as these spatters change properties of the powder feedstock, such as the particle size distribution or the chemical composition.

ALI ET AL. (2019) studied spatter effects on the mechanical properties of 1.4548 parts built using PBF-LB/M under an Ar atmosphere. For this purpose, tensile test specimens were located close to the gas inlet and close to the gas outlet. The latter ones were hypothesized to exhibit worse mechanical properties, as they were located in the downstream area of the gas flow. This was the area, where spatter settling was expected. For comparison, the surface roughness and the static mechanical properties were determined. The tensile test specimens located near the gas outlet showed by 15 % higher surface roughness values. The tensile tests exhibited comparable ultimate tensile strengths (UTS) and yield strengths (YS) in the specimens, while the ductility was decreased by 5 % for the specimens close to the gas outlet. Furthermore, a higher number of pores with, on average, larger sizes were found in the specimens close to the gas outlet via CT scans. The authors attributed this finding to the insufficient melting of present spatters in that area, which leads to defects in the built parts and, therefore, decreased mechanical properties. This mechanism of spatter inclusion is depicted in Figure 3-1. During the PBF-LB/M process, two exemplary spatters A and B settle on and adhere to the solidified melt track behind the current melt pool. Both spatters might exhibit varying sizes, shapes, and chemical compositions. After recoating, the process continues with the laser illumination, whereby the laser power is only high enough to fully melt spatter B. Spatter A is not fully molten and, finally, remains in the final part as an inclusion, which can act as a crack initiation location.

Consistently to the studies of ANDANI ET AL. (2018) and ALI ET AL. (2019), CHEN ET AL. (2022) observed similar spatter effects in their numerical study on the material 2.4668 processed via PBF-LB/M. With their approach, it was shown that spatters falling into the melt pool might not be fully melted by the laser beam and, thus, remain as a defect in the built part.

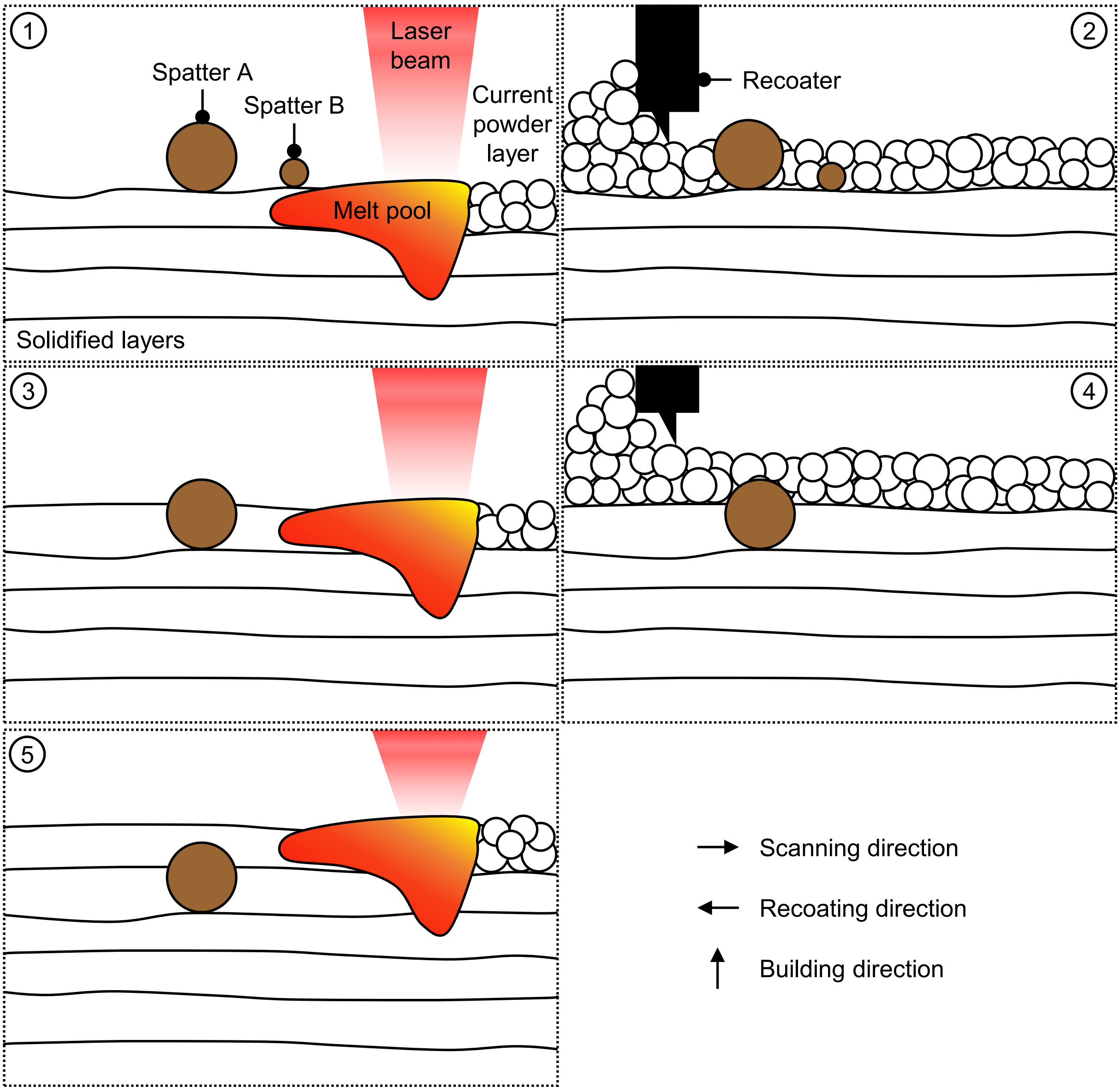

Figure 3-1: Schematic representation of the process of spatter adhesion and inclusion during PBF-LB/M (not to scale; own representation based on ANDANI ET AL. (2018))

The experimental methods in the study of OLIVEIRA ET AL. (2023) resembled those of ALI ET AL. (2019). Tensile test specimens fabricated via PBF-LB/M from a maraging steel under an N_2 atmosphere were located near the gas inlet and outlet as well as in between them and were investigated regarding their mechanical properties. The evaluated hardness values decreased from 458 HV at the gas inlet to 383 HV at the gas outlet. A slight decrease in the UTS from 1135 to 1081 MPa and in the YS from 913 to 867 MPa was found between the gas inlet and the gas outlet, respectively. The authors highlighted the reduced standard deviation for the values of the specimens close to the gas inlet compared to those of the specimens close to the gas outlet. This was attributed to a more unstable process at the latter position due to an increased density of spatters in that area.

Hardware-based mitigation strategies

Besides adjusting the process parameters to reduce spattering, as shown by WANG ET AL. (2017), which are likely to result in economically too slow processes, hardware-based mitigation strategies were presented in the literature. One promising approach is multi-beam illumination, as presented by HEELING ET AL. (2017) and SLODCZYK ET AL. (2021). HEELING ET AL. (2017) used two laser beams to study the occurring effects during the PBF-LB/M of the material 1.4404 under an N_2 atmosphere. Conventional single-laser processing was compared to the application of a second laser for three purposes: pre-heating of the powder in front of the first laser, post-heating of the melt pool behind the first laser, or wobbling around the first laser. These strategies were hypothesized to decrease the thermal gradients of the melt pools and, hence, to reduce melt pool dynamics and spattering. The resulting processes with two scanning velocities (low and high) were captured via high-speed imaging and the spatters were counted. In the single-laser processes, a higher number of spatters was found at the higher scanning velocity. It was shown that the pre-heating as well as the wobbling strategy led to the reduction of the spatter counts compared to the single-laser processes. The authors explained this finding with an agglomeration of metal powder particles before their melting and, thus, a reduced risk for these heavy agglomerates of being entrained by the metal vapor jet or blown away by the gas flow. This advantage was found for both investigated scanning velocities in the multi-laser processes. The post-heating strategy, however, resulted in an increased number of spatters compared to the single-laser process. This was attributed to a splitting of large spatters, which are ejected from the rear area of the melt pool, into more smaller spatters.

SLODCZYK ET AL. (2021) created a multi-laser situation using one single laser, which was split into multiple spots using a diffractive optical element. This approach was applied to the processing of 1.4404 via PBF-LB/M under an Ar atmosphere and monitored via high-speed imaging. The resulting effects of reduced thermal gradients leading to a higher process stability were comparable to those from the wobbling strategy presented by HEELING ET AL. (2017). The number of spatters was found to be similar to the standard single-laser process. However, the multi-laser approach leads to a wider melt pool and, hence, to fewer melt tracks needed to build a part.

A different hardware-based mitigation strategy for spattering was presented by BIDARE ET AL. (2018b). Their study investigated the effect of increased ambient pressures up to 5000 hPa on the PBF-LB/M of 1.4404 under Ar and He atmospheres using Schlieren and high-speed imaging. Several impacts were observed. Under both atmospheres, spatters could successfully be suppressed using high ambient pressures due to the reduction of the metal vapor jet velocity. However, in the Ar process, also more metal vapor was created which reduced the surface quality of the melt tracks. This did not occur in the He process, which led to evenly smooth surfaces at higher ambient pressures compared to the standard process at 1000 hPa. In addition, the scanning velocity could be increased in the He process while maintaining the same melt track quality.

Interim conclusion

Spatters were found to have negative effects on the properties of parts produced via PBF-LB/M. A high number of spatters in the process led to slightly decreased values of the YS, UTS, and elongation at break of the parts. Also, higher porosities were found in those parts, as the large and oxidized spatters might not be fully melted by the laser beam. Spatters could also alter the properties of the powder bed, as not all of them are removed during sieving.
Various complex hardware-based approaches were presented to mitigate those disturbing effects. The application of a second laser to smoothen the melt pool dynamics or the application of high-pressure atmospheres were two of them. However, for industrial applications, the search for a less complex mitigation strategy is still an open research field.

3.3 Formation and effects of spatters in the laser beam welding process

The spattering phenomenon has been studied in the laser beam welding (LW) process for quite a while. The formation mechanisms of spatters in the PBF-LB/M process are similar to those present in laser welding processes. KAPLAN & POWELL (2011) summarized the driving mechanisms for spatter creation in their theoretical work on CW laser welding in the keyhole and conduction modes. In the former case, spatters can be ejected from the melt pool, if the upwards momentum of the melt exceeds its surface tension. The upwards momentum is created by internal convection-driven melt pool dynamics as a consequence of temperature gradients from the keyhole walls to the melt pool edges. Especially in high-power laser welding processes with applied laser powers of several kilowatts, spattering is present. Depending on the area of spatter ejection and the applied process parameters, the size and velocity of the spatters can vary. Spatters ejected close to the keyhole in an upwards direction can, additionally, be accelerated by the metal vapor jet. The authors mentioned that, also in conduction mode laser welding, the boiling temperature of the alloy can be reached. This can lead to spontaneous and violent evaporations and, thus, spatter creation. Metal alloys with alloying elements with low boiling points are particularly susceptible to this phenomenon.

ZHANG ET AL. (2013) provided experimental proof for the spatter formation mechanisms introduced by KAPLAN & POWELL (2011) in their study on high-power (10 kW) CW fiber laser welding of thick plates made of the material 1.4301. For this purpose, the process was observed via high-speed imaging. The melt movement along the keyhole walls could be observed, which is leading to a splashy melt pool and, thus, spatter creation. Furthermore, it could be shown that metal droplets were torn off the keyhole and accelerated upwards by the metal vapor jet inside the keyhole.

Further insights on the dependence of spatter creation on the process parameters were presented by SCHWEIER ET AL. (2013) and LI ET AL. (2014). In the experimental study by SCHWEIER ET AL. (2013), a CW fiber laser with a maximum laser power of 3 kW was applied to the material 1.4301 using beam oscillation. Their results showed that spatter creation highly depends on the applied process parameters. An increasing number of spatters was observed with a decreasing scanning velocity from 150 to 16.67 mm/s (at a fixed laser power) or with an increasing laser power from 1 to 3 kW (at a fixed scanning velocity). LI ET AL. (2014) found similar dependencies on the laser power in their experimental study with a high-power (13 kW) CW fiber laser on the material 1.4301. The authors further mentioned the risk of underfilling of the weld seam due to a loss of molten metal as a consequence of intense spattering.

HAUBOLD & ZÄH (2019) intensified the investigations on reducing or mitigating spattering by the use of laser beam oscillation. For this purpose, a real-time spatter detection algorithm was applied to a laser welding process with a CW fiber laser with a maximum laser power of 3 kW. The results exhibited a significant influence of the beam oscillation frequency on spatter formation. With a decreasing frequency from 242 to 150 Hz, the number of spatters increased. The same trend was found for the average spatter sizes, which increased from 23 µm to 3.8 mm. The authors concluded that all process parameters need to be considered to find a stable process window.

Interim conclusion

As LW is related to PBF-LB/M in terms of the fundamental process characteristics, similar formation mechanisms and effects of spattering were reported. However, since the laser beam velocity in the LW process is about one order of magnitude lower and the laser powers are multiple times as high as those in the PBF-LB/M process, the dependence of spattering on the laser power is more pronounced. It was found that the spattering is especially increased under high laser powers. This is due to the stronger melt pool dynamics induced by the deep and narrow keyhole. One presented mitigation strategy is the oscillation of the laser beam. Results have shown a decreasing number of spatters with an increasing oscillation frequency.

3.4 Process gas usage during the powder bed fusion of metals using a laser beam

Several researchers dedicated their work to increasing the understanding of the interactions between the shielding gas and the PBF-LB/M process phenomena, such as spattering, and the resulting part properties. The related literature presented in this chapter is divided into influences induced by an altered gas flow setting (Subsection 3.4.1) and by a changing gas type (Subsection 3.4.2). The latter topic was dedicated to the gases Ar, N_2, He, and mixtures thereof. Other process gases for the PBF-LB/M process were scarcely studied, for example in a study on the use of hydrogen by ABEL ET AL. (2020), and, thus, are not further considered within the following literature overview. Furthermore, studies related to the topic of the influence of the remaining oxygen level in the build chamber were excluded, such as the works from BAUER ET AL. (2016), PAUZON ET AL. (2019), or PAUZON ET AL. (2021a), since they were not considered relevant for this thesis.

3.4.1 Influence of the process gas flow

Part properties

LADEWIG ET AL. (2016) experimentally studied the effects of varying Ar gas flow velocities and non-uniformities on the material 2.4668 processed via PBF-LB/M on a commercially available machine. The melt pool widths of single melt tracks, the surface and volume defects of bulk material, and the part surfaces were investigated. The gas flow velocity was manipulated by changing the differential pressure of the machine, with the highest setpoint corresponding to a flow rate of 65 m^3/h. The results of the study highlighted the importance of a uniform gas flow over the entire build platform. The melt pool widths of three specimens, which were placed at equal distances from each other over the build platform, increased by about 20 % with an increasing distance to the gas inlet. This was attributed to a stronger laser beam attenuation by process by-products for the specimens furthest away from the gas inlet and, hence, less deep and more shallow melt pools. When decreasing the gas flow velocity, the results showed that this decrease in the melt pool depth was more pronounced with more observable surface and volume defects. The authors conclusively mentioned the importance of a uniform gas flow and stated that the highest possible gas flow velocity should be applied to ensure a stable PBF-LB/M process.

In another experimental study by PAN ET AL. (2022) with an open-architecture PBF-LB/M machine and Ar gas, similar investigations were performed with a custom martensitic stainless steel. Although the results concerning the melt pool width contradicted those presented by LADEWIG ET AL. (2016), which was attributed to significant differences in the experimental setup, the authors underlined the importance of a uniform gas flow with a sufficiently high velocity over the entire build platform. This conclusion was derived from results depending on the position on the build platform of the geometry of single melt tracks and of the density of manufactured cuboids, showing that laser beam attenuation can occur if process by-products are not removed sufficiently.

These findings were corroborated by results from further experimental studies on commercially available machines from REIJONEN ET AL. (2020) and STUTZMAN ET AL. (2023) with the materials 1.4404 and 2.4856, respectively. REIJONEN ET AL. (2020) found a correlation between a decreasing part porosity with an increasing gas flow velocity, as shown in Figure 3-2. All presented studies in Subsection 3.3.1 so far used fixed scanning strategies.

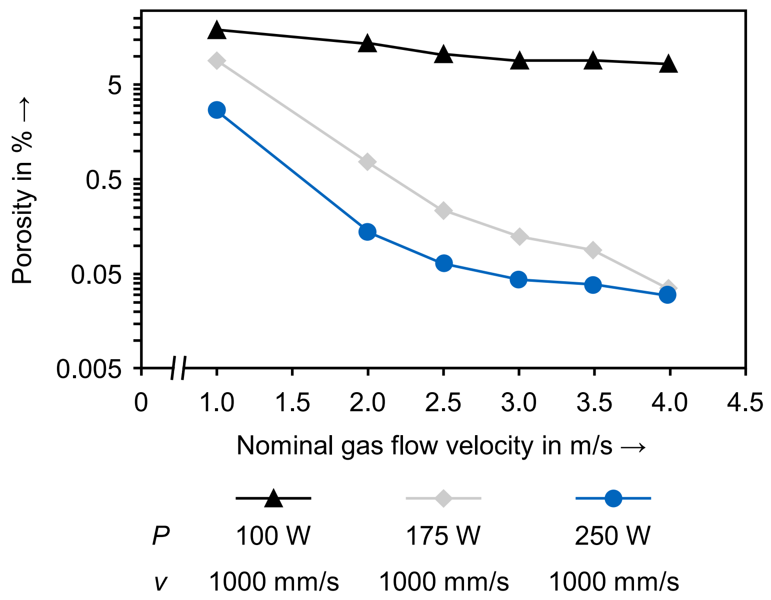

Figure 3-2: Part porosity depending on the gas flow velocity for varying laser powers in 1.4404 processed via PBF-LB/M (own representation based on REIJONEN ET AL. (2020))

AMANO ET AL. (2023) experimentally and numerically investigated the correlations between the Ar gas flow direction relative to the scanning direction and the properties of 1.4404 manufactured via PBF-LB/M. The averaged gas flow velocity, measured via VA, was 1.7 m/s. This velocity was also used in the simulations. In contrast to the above-presented studies from Subsection 3.3.1, the authors of this study claimed uniformity of their gas flow system as presented by AMANO ET AL. (2021a), which allowed a more isolated consideration of the effects. The qualitative results from the simulation showed differences in the temperature and in the thermal conductivity of the gas phase above and behind the melt pool. When the gas flow direction was perpendicular to the scanning direction, the temperature and, thus, the thermal conductivity of the gas phase decreased compared to parallel gas flow and scanning directions. For the latter case, the authors discussed a possibly higher heat dissipation from the melt pool and smaller melt pools as a result of the increased thermal conductivity. However, a proof of this hypothesis was not completed within this work.

In a related study from WEAVER ET AL. (2023), experimental correlations between the relative Ar gas flow direction and the melt pool geometry were determined. HWA measurements unveiled gas flow velocities over the build platform between approximately 3.5 m/s at the gas inlet and below 2 m/s at the gas outlet. Minor differences in the melt pool depth were found between the case of a gas flow direction perpendicular to the scanning direction and the case of a gas flow direction parallel and against the scanning direction. However, a significant decrease of the melt pool depth by about 10 % was determined for parallel and rectified gas flow and scanning directions. This observation was explained by the higher amount of process by-products being blown into the laser beam leading to a lower energy input.

Process by-products

ANWAR & PHAM (2016) presented a study on the accumulation of spatters depending on the relative Ar gas flow direction during PBF-LB/M of the material 3.2381 on a commercially available machine. Two pump power settings, 30 % and 60 % of the maximum power, were applied. In a follow-up study from ANWAR & PHAM (2017), gas flow velocities of 1.43 m/s and 2.87 m/s were found for these low and high pump settings, respectively. Scanning was applied in the direction of and against the gas flow. The created spatters were collected in front of the gas outlet after processing. The results showed that a higher spatter mass occurred with the higher gas flow velocity. For both gas flow velocities, a lower spatter mass was found when scanning in the direction of the gas flow. This was attributed to a higher number of spatters being blown into the laser beam path, re-melted, and separated into finer spatter particles.

With a similar experimental setup, ANWAR & PHAM (2017) investigated the influence of the relative Ar gas flow direction and velocity on the UTS of 3.2381 processed via PBF-LB/M. In order to do this, tensile bars were printed with the identical scanning directions and gas flow velocities presented by ANWAR & PHAM (2016). When scanning against the gas flow direction, a higher UTS of about 290 MPa resulted for the low gas flow velocity compared to when scanning with the gas flow direction (UTS ≈ 260 MPa). For the high gas flow velocity, this significant difference did not occur. The comparison between the gas flow velocities for both scanning directions unveiled that a higher UTS was reached with the higher gas flow velocity. When scanning in the direction of and against the gas flow, this difference in the UTS yielded about 60 MPa and 20 MPa, respectively. These results were correlated with the beforementioned effects of laser beam attenuation when scanning in the direction of the gas flow and a better spatter removal with higher gas flow velocities.

ANWAR & PHAM (2018) extended their previous works and experimentally investigated the spatter distribution in the powder bed during the PBF-LB/M of 3.2381 with Ar. For this purpose, software-processed images taken with a custom imaging setup were studied. By dividing a specific area downstream of the processed area into four segments (see Figure 3-3a), a visual inspection of the spatter distribution was enabled. After the PBF-LB/M processing with two pump power settings of 60 % and 67 %, the spatters were separated from the powder after processing, weighed, and investigated regarding their size. To ensure comparable processing conditions and to avoid influences from a non-uniform gas flow, HWA measurements were conducted before the experiments yielding gas flow velocities of 1.41 ± 0.24 m/s and 1.57 ± 0.21 m/s for the two pump settings, respectively. The imaging results showed that the highest number of spatter pixels (about 40 %) occurred in the segment closest to the processing zone with the lowest number (about 5 %) being observed farthest away from the processing zone (see Figure 3-3b). It was found that the largest and heaviest spatters (diameter: approximately 140 µm, mass: approximately 170 mg) accumulated in the segment closest to the processing zone. With an increasing distance, the spatter size and mass decreased (smallest diameter: approximately 100 µm, lowest mass: approximately 120 mg). Considering the standard deviations, only minor differences were found between the two gas flow velocity settings.

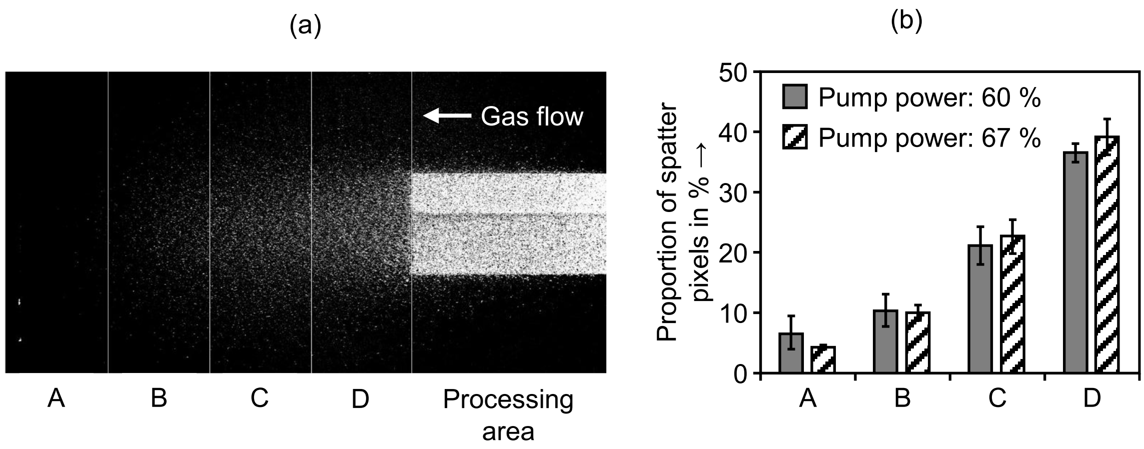

Figure 3-3: Spatter distribution during the processing of 3.2381 via PBF-LB/M; (a) threshold image analysis on a top view image of the process zone demonstrating the spread of powder particles (white) on the powder bed (black), (b) proportion of spatter pixels in the analysis areas for two pump settings with standard deviations (own representation based on ANWAR & PHAM (2018))

In another publication with the same material by ANWAR ET AL. (2019), the research was extended by a numerical study of the spatter distribution. The simulation model was validated using the experimental data from ANWAR & PHAM (2018). The results confirmed the trend from the previous finding that the gas flow was not able to properly remove large and heavy spatters far away from the processing zone. In addition to the first study, the situation of no gas flow was simulated. This led to a significant increase in the percentage of spatters in the segment closest to the processing zone (about 10 %). The model was further utilized to qualitatively extract the travel distances of spatters of various sizes. In the case of a gas flow velocity of 1.41 m/s, spatters were generally transported much further away than in the case of no gas flow. Smaller spatters thereby travelled a higher distance than larger spatters in both cases.

A related study from CHIEN ET AL. (2021) experimentally and numerically investigated the influence of an Ar gas flow on the spattering during the PBF-LB/M of 2.4668. HWA measurements were conducted at nine positions over the build platform to determine the gas flow velocities. Depending on the position and height of the sensor, the measurements showed gas flow velocities between 1.8 and 2.2 m/s. The results of this study additionally confirmed the findings from ANWAR & PHAM (2018) and ANWAR ET AL. (2019) of large spatters landing closer to the processing zone, while only few large particles were found further downstream. The maximum travel distance and height of a spatter leaving the processing zone was determined to have been 154 mm and 57 mm, respectively.

Besides spattering, various studies dealt with the subject of soot and vapor removal by the gas flow. WIRTH ET AL. (2021) experimentally and numerically analyzed both phenomena during the PBF-LB/M of 1.4404 under N_2 on a custom machine. The initial gas flow velocity setting was 1 m/s, which was validated using VA. With the help of the numerical model, it was shown that soot particles were properly removed from the processing zone. However, with regard to spatters, the authors mentioned that the gas flow hardly removed any spatters, especially the large ones. It was discussed that increasing the gas flow velocity could be a measure to counteract this, when staying under a material-dependent threshold velocity. Above this threshold velocity, the powder bed would start to be blown away.

QIN ET AL. (2021) experimentally and numerically investigated the removal of metal vapor by an Ar gas flow during the PBF-LB/M of pure zinc (Zn) in a custom machine. In the simulation, the maximum gas flow velocity of 0.88 m/s and the minimum gas flow velocity of 0.74 m/s were found at the gas inlet and outlet, respectively. The three gas flow velocities 0 m/s, 0.4 m/s, and 0.75 m/s were numerically applied to demonstrate the effects on the removal of the metal vapor. The results for the first case showed that the metal vapor could propagate, while nearly being unaffected, vertically out of the processing zone. Laser beam attenuation was expected. Also, with the second gas flow velocity, no sufficient removal of vapor could be reached. Only with the highest applied velocity, the metal vapor was completely removed from the processing zone. These findings were validated experimentally via optical imaging by capturing the evaporation fume. An unhindered PBF-LB/M could only be applied with the highest gas flow velocity.

Interim conclusion

Several studies highlighted the importance of the gas flow for the stability of the PBF-LB/M process. The results showed that if the gas flow is non-uniform or its velocity is too low, several disadvantages can occur. Spatters and fumes can deflect the laser energy input and, hence, interrupt or reduce the energy input. Increased porosities and reduced mechanical properties could occur. It was mentioned that the gas flow velocity needs to be as high as possible while not blowing away the powder bed. Thus, empirically adjusting the gas flow velocity has shown to be a promising strategy to mitigate negative impacts of spatters. However, the analytical calculation of this threshold velocity for various material and gas combinations has not been done yet.
To study the spread of spatters on the powder bed and characterize them, the separation of spatters was, so far, either done by scooping them out of the powder bed and trying to separate them from the metal powder by sieving, or by extracting solely spatters from only one single layer. In conclusion, the question of the actual spread and collected mass of purely spatters produced under real PBF-LB/M processing conditions remains unanswered.

3.4.2 Influence of the process gas type

The first experimental work on the influence of various gas types on parts produced via PBF-LB/M was presented by WANG ET AL. (2014). The impacts of the gases Ar, N_2, and He on the density, hardness, and tensile properties of specimens manufactured from the material 3.2581 on a commercially available PBF-LB/M machine were determined. No measurements and, thus, no statements on the gas flow velocities were made. The results unveiled no significant differences in the relative density and hardness of the specimens. Relative densities and hardness values of up to approximately 98 % and 110 HV, respectively, were achieved with all gases. The tensile test results showed that the lowest UTS of 342 MPa was achieved for processing with He and the highest UTS of 368 MPa was achieved for processing with N_2. For processing with Ar, a UTS of 355 MPa resulted. The same trend was observed for the YS and the elongation at break. The differences were attributed to severe pore clusters, which occurred in the specimens processed with He.

DAI & GU (2015) numerically investigated a composite material system (3.281 and titanium carbide) and observed the influence of Ar, N_2, and He on the keyhole-mode PBF-LB/M processing. Experimental validation of the findings was obtained by determining the relative density of specimens built on a custom PBF-LB/M machine under the three gases. The simulations showed a significant difference in the fluctuation of the melt pool depth over the course of a single melt track for processing with He (fluctuations of up to 80 µm) compared to N_2 (fluctuations of up to 20 µm) and Ar (no significant fluctuations). It was stated that these fluctuations could lead to a higher porosity due to the collapsing of the keyhole. The resulting surface morphology for processing with He and N_2 qualitatively exhibited more uneven surfaces compared to the processing with Ar. These numerical findings were corroborated by the experimental results showing a lower relative density for the parts produced under He (85 %) and N_2 (91 %) compared to Ar (98.5 %).

Another experimental study on the material 3.2381 was conducted by RAKESH ET AL. (2018). The relative densities, surface roughness values, and tensile properties of specimens produced via PBF-LB/M under Ar and N_2 on a commercially available machine were determined. The results showed no significant differences in the relative density with values for both gases of approximately 98.5 %. The surface roughness values were slightly higher for processing with Ar (approximately 25 µm) than with N_2 (approximately 20 µm). The same trend was observed for the UTS, yielding values of approximately 387 MPa and 365 MPa for processing with N_2 and Ar, respectively. This was primarily attributed to the more even surfaces for processing with N_2.

Similar results on the material 3.2381 were obtained by CH ET AL. (2019), who reported slightly higher UTS for processing with N_2 (UTS ≈ 385 MPa) compared to processing with Ar (UTS ≈ 366 MPa). The conclusions on the surface roughness values and the relative density confirmed the findings from RAKESH ET AL. (2018).

WIMMER ET AL. (2018) focused their experimental work on the influence of Ar, N_2, He, and mixtures thereof on spattering during PBF-LB/M processing of the material 3.2381 in a commercially available machine. For this purpose, high-speed images were evaluated using methods of particle tracking to capture and count spatters and their trajectories. The results unveiled a decreasing number of tracked spatters with an increasing fraction of He in Ar from processing with pure Ar to processing with pure He. Furthermore, a slight decrease in the spatter velocity was found from processing with Ar to processing with He. The values for processing with N_2 lay in between the values of Ar and He.

In a series of studies, the influences of Ar, He, and mixtures thereof on the processing of the material 3.7164 via PBF-LB/M were investigated (PAUZON ET AL. 2020, PAUZON ET AL. 2021b, PAUZON ET AL. 2022a). PAUZON ET AL. (2020) studied the effects of the gases on the mechanical properties and the processing time of parts manufactured on a commercially available machine. Besides pure Ar and pure He, one mixture with 70 vol.-% Ar and 30 vol.-% He and one mixture with 50 vol.-% Ar and 50 vol.-% He were applied to the process. The gas flow velocities were kept constant at 2.2 m/s for all gases. This was ensured by VA measurements. It was shown that the hardness of the manufactured parts in the as-built state increased from Ar (310 HV10) to He (366 HV10). The relative densities in the parts yielded comparable values for all gases in a parameter study. From these results, two promising parameter sets were identified regarding the building rate and used for the tensile tests, since these parameter sets allowed an increase in the building rate of 44 %. The tensile tests unveiled that the UTS and YS of the parts processed under Ar and the gas mixtures were similar with values of 1225 MPa and 1125 MPa, respectively. For processing with He, slightly higher values of the UTS (1275 MPa) and YS (1200 MPa) were achieved. For the latter, lower values for the elongation of approximately 6 % were found compared to the other gases, which yielded similar values of approximately 8 %. The authors discussed that the advantages of He and He-containing gases are coupled with an improved energy input leading to higher residual stresses and, thus, higher static mechanical properties.

In the second study of the series, PAUZON ET AL. (2021b) utilized the optical imaging method of shadowgraphy to further investigate process by-products under He-containing gases during PBF-LB/M. In order to do so, an experimental shadowgraphy setup from HOPPE & ENK (2019) was used. The gases Ar, He, and a mixture thereof were studied. The results showed a lower number of incandescent spatter when using He or the Ar-He gas mixture with reductions of approximately 60 % and 30 %, respectively. This was attributed to the higher cooling ability resulting from the increased thermal conductivity and specific heat capacity of He compared to Ar. It was further hypothesized that the use of He leads to a faster and thinner expanding vapor jet as well as a lower recoil pressure on the melt pool (see Figure 3-4). Ar seemed to remove spatters away from the processing zone more efficiently due to its higher density.

These findings were corroborated by PAUZON ET AL. (2022a), who concluded that the main effect of He on the PBF-LB/M process was the faster cooling of spatters leading to fewer incandescent spatter particles and, thus, lower surface roughness values.

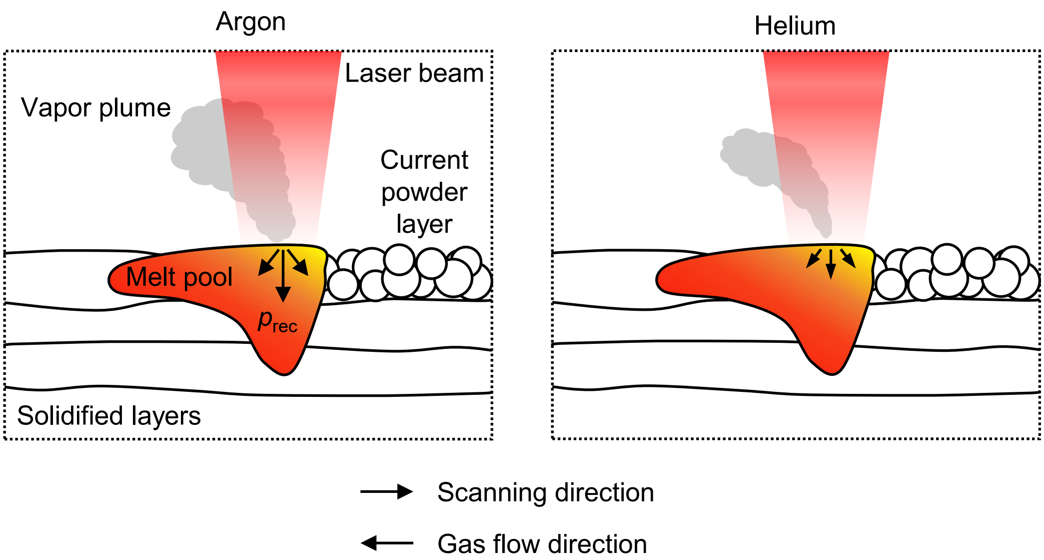

Figure 3-4: Schematic representation of a PBF-LB/M process zone cross-section indicating hypothesized benefits of using helium instead of argon; p_{rec}: recoil pressure (own representation based on PAUZON ET AL. (2021b))

A related study from AMANO ET AL. (2021b) on the material 3.7164 also investigated the influence of Ar and He on the spatter formation in the PBF-LB/M. In contrast to other studies, the authors used a custom spatter collection device in a custom PBF-LB/M machine for their analyses. This device comprised of a metal foil with a cut-out in the middle, which was placed on top of the build platform. One layer of powder was then applied in the area of the cut-out and then the process was started. All generated spatters from the processing of this one layer were ultimately collected on the metal foil. Additionally, thermographic imaging was applied to study the occurring hot spatters. The results showed that the resulting spatter mass was lower for processing with He (approximately 8 mg) than with Ar (approximately 14 mg). The authors discussed that the lower density of He compared to Ar leads to a lower drag force acting on the liquid and, thus, less spatter generation. The thermographic images showed qualitatively fewer hot spatters when processing with He. This was related to the higher thermal conductivity of He compared to Ar.

AMANO ET AL. (2021a) extended their studies with the material 3.7164 on a commercially available machine and experimentally and numerically investigated the cooling rate of the melt pool and the resulting mechanical properties of parts produced via PBF-LB/M for processing with He and Ar. Both gases flowed through the system with the same blow-out pressure of 56 Pa. The numerical model showed higher cooling rates when processing with He compared to Ar. The authors highlighted the higher heat transfer coefficient between the molten liquid and He and the molten liquid and Ar (by a factor of 3.84 higher) as a reason for the better heat dissipation into the gas phase. Finally, a refined α' martensite microstructure and increased hardness values were found in the parts processed with He compared to those processed with Ar. The He-processed parts additionally showed a 4.5 % higher UTS and a 4.8 % higher YS compared to the Ar-processed parts.

TRAORE ET AL. (2021) experimentally investigated the influence of He compared to Ar on the processing of the material 2.4856 via PBF-LB/M. The study was performed on two machines, one custom setup and one commercially available machine. High-speed imaging as well as metallographic methods were applied to study the occurring effects. The focus of the research was placed on spattering, evaporation, the resulting melt pool geometry, and, in contrast to other studies, on the resulting denudation zones. Denudation in this context means the zone around a single melt track, where the metal powder was blown away by the process dynamics. Consistently to other studies, the number of tracked hot spatters for processing with He was lower than for processing with Ar. The results from the metallographic investigations unveiled that the lower part of the melt pool showed no significant differences in size between the gases. The upper part, however, exhibited a larger width under He compared to Ar. This was attributed to more powder from the surrounding being incorporated into the melting process. Further investigations into the resulting denudation area confirmed this finding, as a larger denudation zone was observed under the He atmosphere compared to the Ar atmosphere. Higher observed vapor jet velocities for processing with He due to the lower gas density corroborated the results. The latter finding was also described by STOKES ET AL. (2022), who found higher vapor jet velocities for processing with He compared to processing with Ar and attributed them to the lower molecular mass of He.

PAUZON ET AL. (2022b) applied Ar, He, and a mixture of 70 vol.-% Ar and 30 vol.-% He to gyroid-type lattice structures fabricated via PBF-LB/M from the material 2.4668 on a commercially available machine. X-ray CT and optical tomography (OT) were used, among other methods, to study the occurring effects on the parts and on the process, respectively. The OT images were processed via software and visualized as one single three-dimensional image for comparison. These images showed that fewer incandescent spatters were produced for processing with He-containing gases compared to processing with Ar. Furthermore, the width of their spreading around the parts was reduced. Regarding the built parts, no significant differences were found in their microstructure, density, or mechanical strength.

Interim conclusion

The main gases studied for application in the PBF-LB/M process were Ar, He, and N_2. While only minor differences were found between the gases Ar and N_2 in terms of influences on the process or part properties, the use of He led to changes in the PBF-LB/M process compared to Ar. Early works on the latter comparison reported slight disadvantages in the use of He. This was attributed to higher melt pool depth fluctuations during manufacturing and the creation of severe pore clusters. These lead to reduced YS and UTS values. The lower density of He was held responsible for this since it results in a non-uniform recoil pressure and, hence, an unstable melt pool. In contrast, more recent studies highlighted various advantages of He over Ar in the PBF-LB/M process. The higher thermal conductivity and specific heat capacity of He compared to Ar were found to lead to a decreased number of incandescent spatters and to increased melt pool cooling rates leading to finer microstructures in the parts. A generic description of the cooling process of spatters is, however, still missing. Furthermore, the research area on the influence of the severe differences in the gas density on the process has not been tackled yet.

3.5 Process gas influence during the laser beam welding process

In LW processes, gases were successfully applied for various purposes. One goal is to protect the process zone from contaminations of the surrounding atmosphere, to keep it free of spatters, and to suppress plasma formation. This is mainly done using inert gases, such as Ar or He. Another goal is to influence the geometrical properties and chemical compositions of the melt tracks by the use of active gas components, such as N_2 or CO_2. CHUNG ET AL. (1999) experimentally investigated the effect of various gases on the CO_2 laser beam welding process with a constant laser power of 6 kW and a scanning velocity of 4 m/min. The gases Ar, He, N_2, CO_2, and a mixture of 50 vol.-% Ar and 50 vol.-% N_2 were applied to the processing of a galvanized steel alloy. One goal of the study was to determine the influence of the gases on the geometrical melt track properties. It was shown that He provided the best penetration among the studied gases. This was attributed to the higher ionization energy of the gas compared to, for example, Ar, which leads to a smaller plasma plume above the processing zone and, ultimately, to a better energy input. In this comparison, Ar showed the worst penetration due to a large plasma plume being created. CO_2 showed nearly a penetration as good as He. Although its ionization potential is on the same level as that of Ar, the dissociation of the molecule into carbon monoxide (CO) and oxygen (O) and the following oxidation of the melt leads to an increased penetration compared to Ar. However, this was found to be connected with a higher risk of CO gas pores. When adding N_2 to Ar, the penetration increased compared to the pure Ar process. This was attributed to the fact that N_2 reacted with the liquid metal and, thus, less gas was available for plasma formation. The authors concluded that the Ar-N_2 mixture and He were the best gases in terms of melt track penetration for the CO_2 laser welding process.

The advantages of He were further studied by WANG ET AL. (2007). In their numerical and experimental study on the laser beam welding of the material 3.7164, where the shielding of the process zone is of particular importance, the characteristic lengths of the shielding zones were compared. The results showed that, when the inclination angle of the gas nozzle was fixed, He provided a larger shielding zone than Ar.

In an experimental study by BOUKHA ET AL. (2013), the influences of Ar, CO_2, and mixtures thereof on the laser beam welding process of 3.3547 were investigated. A CW fiber laser with a laser power of 2.5 kW was used at a scanning velocity of 1 m/min. No significant changes in the microstructures and mechanical properties of the built specimens were found with an increasing addition of CO_2 from pure Ar to pure CO_2. However, a significant increase in the melt track width and depth as well as an oxidation of the melt track surfaces were observed. DAUB (2012) observed similar effects with the addition of CO_2 to the process gas in conduction mode laser beam welding and attributed this effect to the increased convective melt pool flows, which lead to increased penetration depths.

Further studies were dedicated to the differences in the use of inert gases in the laser welding process. AHN ET AL. (2017) compared the use of Ar and He in a CW fiber laser welding process of the material 3.1355. Due to the reduced plasma formation under He, which was described by CHUNG ET AL. (1999), higher scanning velocities could be applied. This was enabled by the better energy coupling reducing the risk of pore formation at increased velocities. The hardness of the specimens produced under He remained the same as of those produced under Ar. These findings were corroborated by a study from XU ET AL. (2019), where in addition to the study from AHN ET AL. (2017) and consistent to the study from CHUNG ET AL. (1999), higher penetration depths were found for processing with He. This was again attributed to less plasma formation and, thus, a better energy input.

Another important aspect of the gas utilization in the laser beam welding process, the influence of the local gas flow, was studied by SCHMIDT ET AL. (2020) and CHEN ET AL. (2023). Although being carried out on different materials, both studies presented similar results on the use of the gas flow. When the gas flow rates were increased, various positive effects were found. The keyhole was stabilized due to the increased ambient pressure, plasma plumes were effectively suppressed, and spatters were removed. This led to a reduced risk of defect formation and an increased process stability.

Interim conclusion

In contrast to the PBF-LB/M process, the scanning velocities of the laser beam in LW processes are lower by an order of magnitude. This leads to much higher interaction times between the liquid metal and the surrounding atmosphere. Besides inert gases, which are used for shielding purposes similar to the PBF-LB/M process, active gas components can also be applied in LW processes. The latter gases can be utilized to alter the properties of the resulting parts, such as their chemical composition in the weld seam, or the process behavior and properties, such as the penetration depth. Besides N_2, the most widely studied active gas component is CO_2. This gas molecule can dissociate into CO and O close to the melt pool and, thereby, oxidize the melt surface. This can lead to higher penetration depths as a consequence of increased convective flows in the melt pool. Among the inert gases, He has shown beneficial effects over the standard gas Ar on the LW process. Due to its higher ionization energy, less plasma is created that could potentially interact with the laser beam. Hence, a better energy coupling is reached, even at increased scanning velocities. Finally, similar to the PBF-LB/M process, higher gas flow rates benefit the LW process stability since the plasma plume is suppressed and spatters are removed.

3.6 Simulative approaches to investigate laser-based manufacturing processes

Numerical modeling can support experimental studies to comprehensively understand the complex interactions in the process zone during PBF-LB/M. The numerical methods can be divided depending on the time and size scale to be studied, as it was already partly shown in the previous chapters (see Figure 3-5). In mesh-based modeling approaches, the finite element method (FEM), as well as computational fluid dynamics (CFD) (such as finite volume methods), play a major role. These are usually applied to study effects on the meso- and macroscale but highly depend on the domain size to be studied. While FEM enables investigations on the evolution of the melt pool over several tracks or layers, CFD typically only allows for small domain sizes (several hundred micrometers) in a single-track simulation (TREJOS-TABORDA ET AL. 2022). In the latter, the addition of complexity to the simulation often results in high computational costs. Among the mesh-free methods, smoothed particle hydrodynamics (SPH) or the lattice Boltzmann method were widely utilized in research to investigate micro-, meso-, and macroscale effects, such as heat transfer. In the following, various studies using SPH models are presented, concerning investigations of laser welding followed by those focusing on PBF-LB/M. Other simulation methods are not discussed as they are outside the scope of this thesis.

The conduction mode LW process was simulated using SPH in studies by HU ET AL. (2016) and HU & EBERHARD (2017), where the ability of SPH to represent LW was demonstrated. The basic principles of the 3D model were derived from the works of MONAGHAN & GINGOLD (1983), MONAGHAN (1992), and MONAGHAN ET AL. (2005). Compared to these works, a temperature-dependent surface tension model, as well as temperature-dependent material properties (e.g., specific heat capacity), were additionally incorporated to model melt pool flows properly. A ray tracing approach was used to represent multiple reflections within the melt pool. In the work from HU ET AL. (2016), a successful validation of the SPH model results with experimental and analytical results was performed to study the ability of the model to simulate deep penetration LW. HU & EBERHARD (2017) used the built model to study the basic interrelations between the laser power, the scanning velocity, and the resulting melt pool dimensions. Inverse trends were found for the two parameters, with increasing laser powers and decreasing scanning velocities leading to increasing melt pool dimensions.

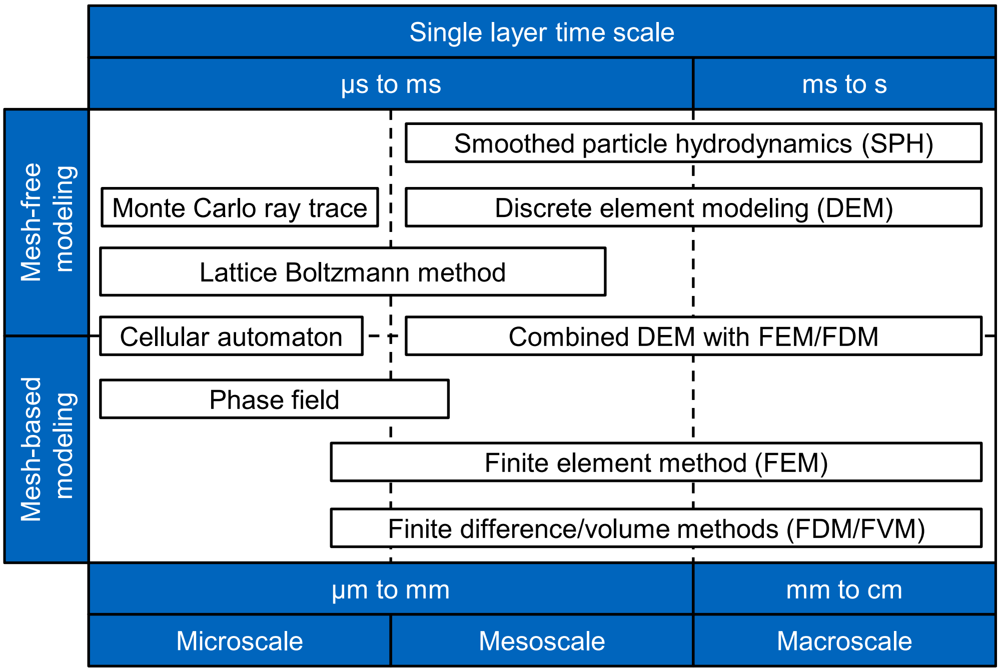

Figure 3-5: Overview of relevant applicable simulation methods to study the PBF-LB/M process (own representation based on SOUNDARARAJAN ET AL. (2021))

In the field of PBF-LB/M, RUSSELL ET AL. (2018) set up a 2D SPH model referring to HU ET AL. (2016) and investigated its suitability to study the PBF-LB/M process. In contrast to the LW investigations, where only conduction mode welding at comparably low temperatures was studied, the application of SPH to PBF-LB/M required further improvements according to (RUSSELL ET AL. 2018). In the thermal part of the model, conduction and radiation were incorporated via the Fourier's and the Stefan-Boltzmann law, respectively. The laser beam was modeled with a Gaussian profile. Its absorption into the material was calculated using a Beer-Lambert scheme, where the laser penetration is a function of the absorptivity of the material. The surface tension was implemented as a function of the temperature to accurately describe melt pool flows. No attempts were made to model the ambient atmosphere or the gas flow. After a successful experimental validation, the developed model was used to study the effect of laser power variations on the melt pool during the processing of a stainless steel. Following the results from previous studies, it was discovered and confirmed that the Marangoni convection was the main driving force for the melt pool flow. Higher laser powers led to increased melt pool turbulences, thereby resulting in higher surface roughness. Another scope of the work was demonstrating the ability of the SPH model to easily represent multi-material PBF-LB/M. For this purpose, every third particle was given twice the thermal conductivity of its neighbors. Small changes in the geometry of the solidified track were found, which could be attributed to the positions of the doped SPH particles. The authors concluded that the SPH method is a promising approach to study the complex phenomena occurring during PBF-LB/M. However, improvements in the computational cost of the method, mainly driven by the implementation of the surface tension, must be made. Also, the extension of the model to 3D domains was highlighted as a future research goal.

These challenges were addressed by Weirather et al. (2019). The authors presented an SPH simulation study on the processing of 2.4668 by PBF-LB/M. Not only did they improve the computation times by switching to processing with a graphics processing unit, but the authors also presented a novel approach for the incorporation of evaporation. Regarding heat transfer, the gas phase was considered as an isothermal boundary condition. No gas flow was included. With a variation of the process parameters, various effects on the melt pool could be shown. For all melt pool dimensions (width, depth, and length) as well as for the mean melt pool temperature, an increase was observed with increasing laser powers and decreasing scanning velocities. Differences were also found in the penetration depths of the melt pool with varying process parameters. However, the authors concluded that multiple reflections of the laser beam need to be considered to enable a realistic keyhole-regime process simulation.

In a series of studies on SPH from Afrasiabi et al. (2021), Afrasiabi et al. (2022b), and Afrasiabi et al. (2022a), the authors build upon the works of Russell et al. (2018) and Weirather et al. (2019), among others. Efforts were put into reducing the computation times by up to 50 % compared to Russell et al. (2018) using an optimized neighbor-search approach (Afrasiabi et al. 2021), implementing an enhanced powder layer generation (Afrasiabi et al. 2022b), and extending the model towards the 3D domain (Afrasiabi et al. 2022a). Similar to Weirather et al. (2019), Afrasiabi et al. (2022a) introduced an additional recoil pressure acting on the melt pool, which was caused by evaporation. The simulation of PBF-LB/M processing of the material 2.4668 was used as the test scenario to study the occurring effects in the melt pool. In the first part, the effect of the introduced recoil pressure was studied. It was shown that the depth of the melt pool significantly increased compared to a model without recoil pressure. The extended model was then used in the second part of the study to demonstrate the effect of varying laser powers and scanning velocities. The results unveiled that the melt pool dimensions increased with increasing laser powers or decreasing scanning velocities.

Other works on the utilization of SPH for the modeling of the PBF-LB/M process investigated further phenomena based on the model of Weirather et al. (2019). Wimmer et al. (2021) extended the model to study in-situ alloying during PBF-LB/M. In order to do so, a species transport formulation based on the Fickian diffusion was incorporated. The authors investigated the resulting melt pool dimensions during the processing of powder blends of the materials 1.4404 stainless steel and 3.2381 and validated their results experimentally. Zöller et al. (2023) made use of the SPH model from Weirather et al. (2019) to study the defect mechanism balling during PBF-LB/M with varying scanning velocities and laser powers. While the balling behavior remained the same for different laser powers, the ball sizes varied.

Interim conclusion

The presented simulative approaches to model PBF-LB/M using SPH showcased that this method is suitable to effectively study relevant process phenomena on the microscale. The characteristics of the melt pool, such as its temperature, dimension, or internal flow regime, can be investigated depending on the process parameters. Furthermore, the resulting solidified melt tracks can be characterized by their surface roughness or by occurring defects, such as balling. However, the presented works did not consider gas flow within their simulations and the gas phase was represented as an isothermal boundary condition.

3.7 Need for action

The overview of related literature given above summarized the relevant state of the art prior to this thesis. From this, the research deficit in the form of open research areas (RAs) was derived. Please note that these RAs were valid at the beginning of this dissertation project.

RA1 Manipulating the gas flow properties has shown to be a promising and simple mitigation strategy against spattering. Increasing the gas flow velocity can lead to an enhanced removal of spatters. However, when the velocity is set too high, the powder bed can be blown away. The current state of the art is lacking a thorough understanding of the threshold velocity and, ultimately, its calculation for various material and gas combinations.

RA2 There is a research deficit concerning the investigation of the spread of spatters over the powder bed, as the studies presented to date are limited in two ways. They were either performed on custom laboratory setups providing only single-layer observations. Alternatively, they were performed on commercially available machines but suffered from uncertainty as they observed spatters lying in the powder bed, which were then only distinguished optically. Furthermore, these studies were only limited to Ar.

RA3 The use of He unveiled various advantages for the PBF-LB/M process, such as the production of less incandescent spatter due to advanced cooling capabilities of He. However, the studies available to date mainly focused on experimentally observing and describing the occurring phenomena. Only few studies presented theoretical approaches to this cooling process. A holistic and generic understanding of the relevant heat transfer mechanisms during the spatter cooling by any process gas is a research deficit.

RA4 A research gap exists in the understanding of the effects of using He instead of Ar on the melt pool characteristics. The studies on this topic presented above mainly focused on the increased cooling rate leading to refined microstructures of the resulting parts. However, to fully understand and exploit the potential of using He or He-containing gases, its influence on the melt pool geometry and temperature needs to be understood to properly set the process parameters.

RA5 High-strength Al alloys become more and more important for industry due to their promising combination of high strengths and low densities, making them alternatives to steel alloys in certain applications. It needs to be investigated whether or not the findings on the process gas influence hold valid for these alloys, too. The studies available to date mainly focused on titanium-, nickel-, or iron-based alloys. The few studies on Al alloys are limited to the material 3.2381, which is known to be a robust alloy for the process. The study of high-strength Al alloys, which are particularly susceptible to cracking phenomena, needs to be performed separately in this regard.

This, in summary, led to the research goal and approach outlined in the next chapter.

4 Research approach

4.1 Chapter overview

In Chapter 4, the research approach of this dissertation is described. Section 4.2 outlies the three scientific objectives based on the need for action derived in Section 3.7. Afterwards, the methodological approach to achieve the scientific objectives comprising of four stages is presented in Section 4.3. The chapter concludes in Section 4.4 with the description of the integration of the six key-publications of this thesis.

4.2 Scientific objectives

There have been various efforts to investigate the influence of the process gas used during PBF-LB/M. Although the experimental observations on the interactions between the gas and the process hold valid for various materials, the underlying physical mechanisms have not been unveiled yet. No generally valid approaches were derived to describe the relevant interactions between the gas and the process. Therefore, the choice of the gas flow velocity and type remained unclear. The global objective of this thesis was to improve the understanding of the relevant interactions and, thus, to support the choice of the process gas settings. Three sub-objectives (SOs) were defined to address the open RAs prior to this thesis work (cf. Section 3.7):

SO1 The removal of spatters and their spread over the build platform during PBF-LB/M were to be investigated. Therefore, in the first step, it was necessary to elaborate the upper limits of the gas flow velocity with regard to the blowing away of powder particles from the powder bed (cf. RA1). Based on these limits, the removal of ejected spatters by the gas flow could be evaluated (cf. RA1). Ultimately, the spread of spatters on the powder bed had to be identified (cf. RA2). Therefore, a method had to be developed to separate the spatter particles from the powder bed (cf. RA2). The elaborated models, which were initially developed independently from the gas type, had to be tested on the gases Ar and He, which have been studied in the current state of the art.

SO2 Since Ar and He have been shown to alter the heat balance in the PBF-LB/M process differently, the influence of arbitrary gases on the heat balance needed to be described. As the effects lie on different scales, individual considerations of the spatter and the melt pool cooling had to be performed (cf. RA3 and RA4). To capture the relevant effects experimentally, suitable process observations had to be selected and applied. However, as relevant process observation techniques only determine the total heat transfer, analytical approaches had to be found to unveil the individual contributions of the three phenomena conduction, convection, and radiation on the spatter and melt pool level (cf. RA3 and RA4). Experimental data had to be used to validate the analytical approaches.

SO3 Once the relevant physical interactions had been derived, a selection of gases were to be applied to PBF-LB/M to determine their influence on the process stability and the resulting part properties. High-strength aluminum (Al) alloys are known to be difficult to process via PBF-LB/M, as they suffer from various defect mechanisms, such as hot cracking. Thus, studying these hard-to-process alloys was hypothesized to emphasize the benefits of an enhanced process gas usage. The resulting parts had to be analyzed with respect to their density, chemical composition, and static mechanical properties for the evaluation.

4.3 Methodological approach

The methodological approach in this thesis was structured into four stages, which were derived from the three SOs presented in Section 4.2. Firstly, preliminary investigations on the influence of the process gas were performed, followed by studies on the underlying physical phenomena in the stages 2 and 3. In the last stage, the gained knowledge was applied to a high-strength Al alloy. The unique and novel results of the investigations were made available to the scientific community via six publications (P1 – P6). Figure 4-1 summarizes the stages within the methodological approach and the associated publications.

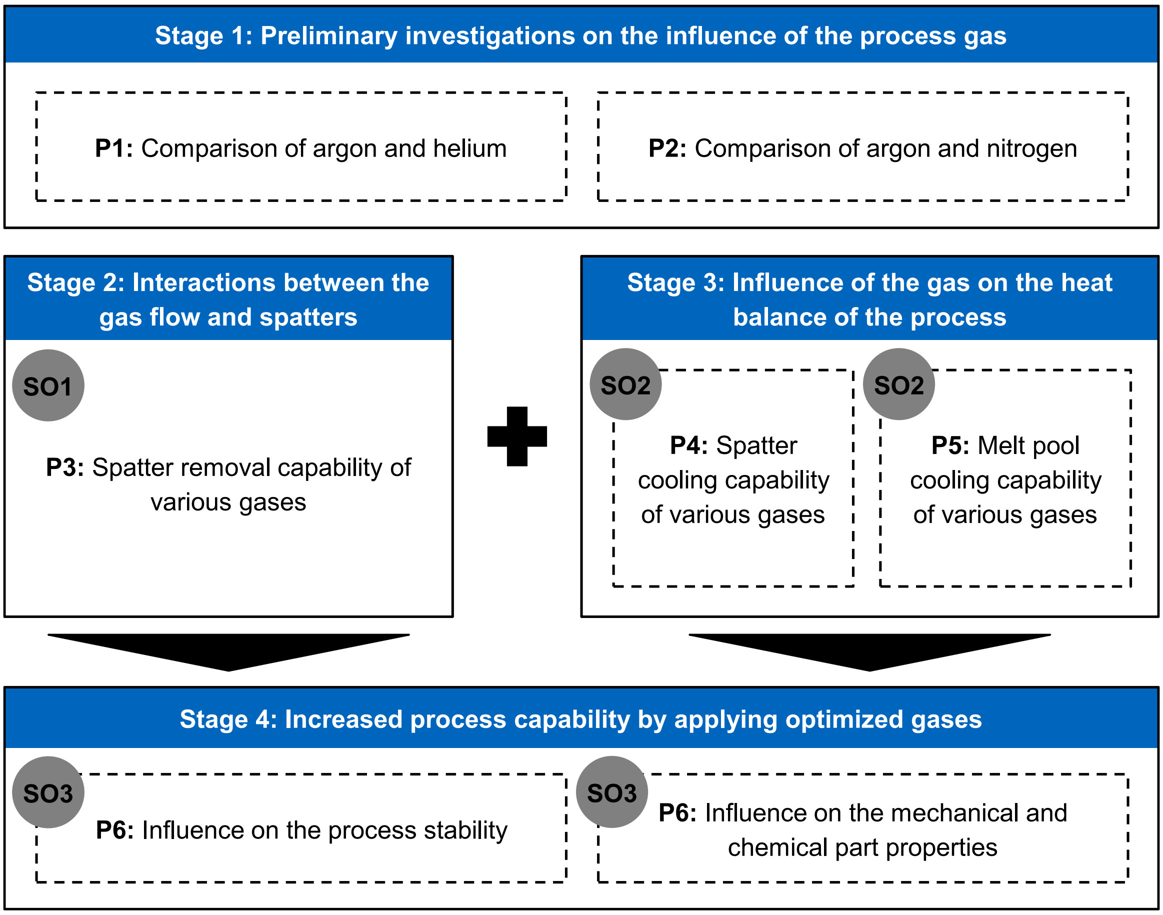

Figure 4-1: Schematic representation of the methodological approach based on four stages with the associated publications P1 – P6

Stage 1 Initially, preliminary investigations were performed to gain basic knowledge about the possible interactions between the process and the gas based on the state of the art. Therefore, Ar, a standard gas for PBF-LB/M, was compared to He (P1) and N_2 (P2) in experimental studies. The gas He has shown benefits for PBF-LB/M in the state of the art for various materials. Since no studies were performed with Al, an initial study had to be performed with that group of alloys. Although N_2 is slow to react with a variety of materials, it has the potential to form intermetallic phases with Al. Therefore, a method to deliberately investigate this phenomenon had to be set up.

Stage 2 Based on the results from the preliminary studies, investigating the removal of spatters by two gases with highly different physical properties, Ar and He, followed (P3). Hence, this stage addressed SO1. The particle pickup velocity for each gas had to be determined in the first step. This velocity set the limit for the maximum applicable gas flow velocity. Once this velocity could be defined, the removal of spatters by the gas flow was investigated. For this purpose, a unique spatter sampling device was designed and set up to only sample spatters during processing. This device enabled the study of the spread of spatters over the powder bed.

Stage 3 Besides the removal and spread of spatters, the cooling of spatters and of the melt pool by the gas flow (Ar, He, and mixtures thereof) was of interest (cf. SO2). The occurring effects on the spatter level were studied analytically by using a heat transfer model for a single spatter particle and experimentally by utilizing the Schlieren imaging method for the visualization of temperature gradients in the gas atmosphere (P4). For the melt pool, a combined experimental and simulative approach was chosen (P5). Pyrometry and metallography were applied to study the surface temperatures and dimensions of the melt pool, respectively, under various gases. The results were used to validate an SPH simulation model. The model was then applied to unveil the heat balance of the melt pool. In particular, the contributions of the individual heat transfer phenomena to the overall heat transfer were studied.

Stage 4 In this stage, which addresses SO3, Ar, He, and mixtures thereof were applied to the processing of a high-strength Al alloy via PBF-LB/M (P6). This experimental study was focused on determining differences in the process stability as well as in the chemical composition and static mechanical properties of the produced parts. Optical process imaging and porosity measurements were applied to investigate the process stability. Destructive testing methods served as techniques to study the properties of the parts.

4.4 Integration of the publications

Figure 4-2 gives an overview of the six publications P1 to P6, which were included in this thesis. The authors, the titles of the publications, and the publication media are provided. The content of the publications is presented in more detail in Chapter 5. A list of the embedded key publications can be found in the Appendix A.

Stage 1: Preliminary investigations on the influence of the process gas	
P1	*Proceedings of Europe's Annual Powder Metallurgy Congress (EuroPM) 2020* **Title:** Influence Of Different Process Gases On AlSi10Mg Parts Processed By LPBF – Microstructure And Mechanical Properties **Authors:** Siegfried Bähr, Thomas Ammann, Graham Matheson, Alper Evirgen, Pierre Forêt, Andreas Bachmann, Michael F. Zäh
P2	*Proceedings of the Metal Additive Manufacturing Conference (MAMC) 2021* **Title:** Cracking Behavior of a Zr-blended Al-Zn-Mg Alloy Processed by PBF-LB/M Under Different Process Gas Mixtures **Authors:** Siegfried Baehr, Thomas Ammann, Graham Matheson, Andreas Wimmer, Michael F. Zaeh
Stage 2: Interactions between the gas flow and spatters	
P3	*Progress in Additive Manufacturing* **Title:** Experimental and Analytical Investigations of the Removal of Spatters by Various Process Gases During the Powder Bed Fusion of Metals Using a Laser Beam **Authors:** Siegfried Baehr, Tobias Klecker, Sebastian Pielmeier, Thomas Ammann, Michael F. Zaeh
Stage 3: Influence of the gas on the heat balance of the process	
P4	*Journal of Laser Applications* **Title:** Investigations of process by-products by means of Schlieren imaging during the powder bed fusion of metals using a laser beam **Authors:** Siegfried Baehr, Lukas Melzig, Dominik Bauer, Thomas Ammann, Michael F. Zaeh
P5	*Metals* **Title:** Investigations on the Heat Balance of the Melt Pool during PBF-LB/M under Various Process Gases **Authors:** Siegfried Baehr, Fabian Fritz, Stefan Adami, Thomas Ammann, Nikolaus A. Adams, Michael F. Zaeh
Stage 4: Increased process capability by applying optimized gases	
P6	*Advances in Industrial and Manufacturing Engineering* **Title:** Influence of argon, helium, and their mixtures on the powder bed fusion of an Al-Cu-Li-Ti alloy using a laser beam: evaporation, microstructure, and mechanical properties **Authors:** Siegfried Baehr, Graham Matheson, Thomas Ammann, Peter Mayr, Michael F. Zaeh

Figure 4-2: Overview of the publications dedicated to the four stages of the methodological approach

In all six publications listed, the author of this dissertation was also the main author. Thomas Ammann, Dr.-Ing. Dominik Bauer, and Pierre Forêt are or were members of the AM group of Linde GmbH. They contributed to brainstorming, experimental work, program activities, and editing. Graham Matheson and Dr. Alper Evirgen are or were material scientists at Oerlikon AM GmbH and contributed to the experimental work and editing. Fabian Fritz currently is a research associate of the chair of aerodynamics and fluid mechanics at TUM (AER) and shared first author of P5. Dr.-Ing. Stefan Adami currently is a research group leader at the AER and supported editing. Tobias Klecker, Sebastian Pielmeier, and Lukas Melzig were students at the *iwb* who supported the experimental work. Andreas Wimmer and Dr.-Ing. Andreas Bachmann were consecutive heads of the department of additive manufacturing at the *iwb*. They contributed to brainstorming and editing. Prof. Dr.-Ing. Nikolaus A. Adams is head of the AER. He contributed to editing. Prof. Dr. Peter Mayr is head of the chair of materials engineering of additive manufacturing at TUM and contributed to editing. Prof. Dr.-Ing. Michael F. Zaeh is head of the *iwb* and the supervisor of this dissertation. A more detailed description of the individual contributions is given in Chapter 5 according to the contributor roles taxonomy (CRediT). A list of all supervised student works can be found in the Appendix B.

5 Research findings

5.1 Chapter overview

Chapter 5 provides a summary and discussion of the research findings of this thesis. Therefore, in Section 5.2, the scientific results of the six key-publications are presented in the Subsections 5.2.1 to 5.2.6. After the recapitulations of the contents, the main findings as well as the individual contributions of the authors are listed. A discussion of the results with respect to the state of the art and the SOs is given in Section 5.3. Finally, to evaluate the costs of a changing process gas, an economic assessment of part costs with respect to the process gas is presented in Section 5.4.

5.2 Process gas influences

5.2.1 P1: Preliminary investigations on argon and helium

Recapitulation

In P1 "Influence Of Different Process Gases On AlSi10Mg Parts Processed By LPBF –Microstructure And Mechanical Properties" (BÄHR ET AL. 2020), an experimental study comparing the use of the gases Ar, Ar-He mixtures, and N_2 during PBF-LB/M was conducted. The well-established Al alloy 3.2381 was applied to focus the investigations on the influence of the gases. Two build job designs were manufactured within the study on a commercial PBF-LB/M machine. First, cubes were fabricated using varying laser powers, scanning velocities, and hatch distances. The cubes were treated metallographically (grinding, polishing, and etching) so that their relative density, hardness, penetration depth of the laser beam, and microstructure could be examined. Based on the density measurement results, the best parameter set was chosen for the second part of the study. In this second part, tensile test specimens were manufactured and static tensile tests were performed.

The results showed minor differences in the mean values of the relative densities, hardnesses, and penetration depths, which originate from the different gases. In the microstructure evaluations via scanning electron microscopy (SEM), the well-known microstructure of 3.2381, exhibiting a cellular grain substructure consisting of a columnar α-Al region surrounded by a eutectic Si-rich region, was determined for all samples produced with all gases (see Figure 5-1). The mean cell size in the columnar α-Al region was found to be about 18 % larger in the samples produced under Ar compared to those produced under a mixture of 50 vol.-% Ar and 50 vol.-% He. It was hypothesized that these differences could be attributed to the higher cooling abilities of He compared to Ar. The tensile tests unveiled an increasing tensile strength and elongation at break while the yield strength remained constant with an increasing He-content in the gas. It was assumed that this originated from a hardening effect following the refined microstructure in the parts processed under He. The static mechanical properties for the processing with N_2 were found to be consistently lower.

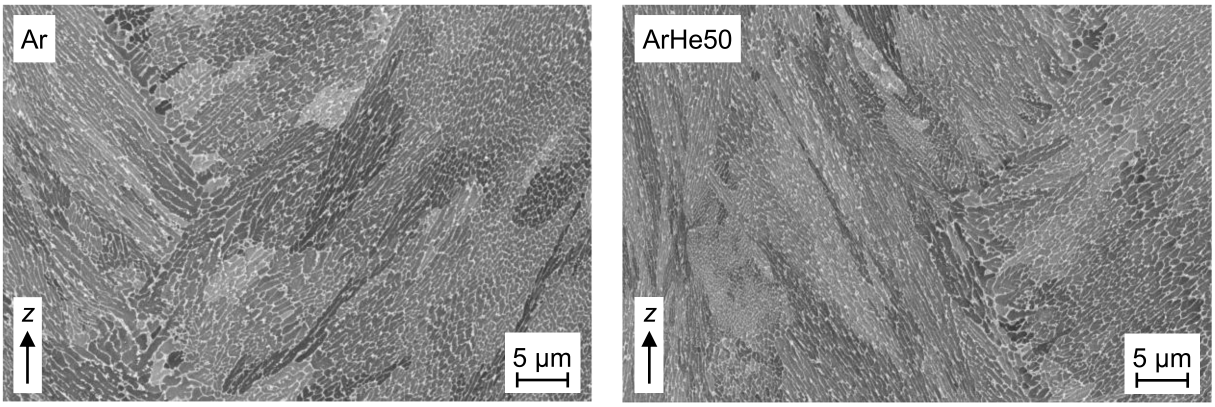

Figure 5-1: SEM images of the metallographic cross-sections unveiling the cellular grain substructure of samples processed under Ar and ArHe50 (50 vol.-% Ar + 50 vol.-% He); z: building direction (own representation based on BÄHR ET AL. *(2020))*

Main findings

The main conclusions and research findings of BÄHR ET AL. (2020) were the following:

RF1 No significant differences in the mean values of the relative densities, hardnesses, and penetration depths were found in the parts processed under Ar, Ar-He mixtures, and N_2.

RF2 The use of the ArHe50 gas mixture led to a reduction in the mean cell size of the cellular substructure of the processed parts of about 18 % compared those fabricated under pure Ar. It was hypothesized that these differences occurred due to the varying cooling capabilities of Ar and He.

RF3 Parts processed with increasing He-contents exhibited higher tensile strengths and elongations at break while the yield strengths remained constant compared to the Ar-processed parts. A hardening effect due to the refined microstructure was assumed to be the main reason for this difference. The use of N_2 led to overall lower values.

Contributions of the authors

Siegfried Baehr was the main author of this publication and presented the results in an online talk at the scientific conference *Europe's annual powder metallurgy congress and exhibition (EuroPM)* that took place from October 5 – 7, 2020. The individual contributions of all authors are listed below:

Siegfried Baehr Conceptualization, Formal analysis, Investigation, Methodology, Validation, Visualization, Writing – original draft

Thomas Ammann Investigation, Methodology

Graham Matheson Investigation

Alper Evirgen Writing – review & editing

Pierre Forêt	Project administration, Writing – review & editing
Andreas Bachmann	Project administration, Supervision, Writing – review & editing
Michael F. Zaeh	Project administration, Supervision, Writing – review & editing

5.2.2 P2: Preliminary investigations on argon and nitrogen

Recapitulation

In P2 "Cracking behavior of a Zr-blended Al-Zn-Mg alloy processed by powder bed fusion of metals using a laser beam under different process gas mixtures" (BAEHR ET AL. 2021), possible chemical reactions between the process gas and the melt pool were investigated. The hypothesis of the publication indicated that N_2 could lead to nitride formation in Al alloys.

For that purpose, a high-strength Al alloy (Al, zinc (Zn), magnesium (Mg)) was processed via PBF-LB/M under Ar and N_2. To avoid cracking in the specimens, the alloy was mixed with 1.2 m% zirconium (Zr). The creation of Al_3Zr precipitates during solidification showed promising results in the literature to avoid cracking. The first part of the study was dedicated to the demonstration of this crack-avoiding effect. Therefore, cubes were fabricated on a PBF-LB/M machine under Ar and N_2 atmospheres and investigated using metallography (grinding, polishing, and etching) and optical microscopy. The second part of the study focused on the initial hypothesis of this publication that the use of N_2 could lead to nitride formation. An experimental setup was designed and applied, where a gas mixer, which could mix up to six gases at any ratio desired, was connected to the PBF-LB/M machine. To deliberately demonstrate the occurring effects, a build job design was applied that consisted of cuboids, which were divided into three zones over their height. In the first zone, pure Ar was used as the process gas. In the second zone, a mixture of 50 vol.-% Ar and 50 vol.-% N_2 was applied. The last zone was processed under pure N_2. The gas changes were performed seamlessly during processing. Metallography to create cross-sections, SEM to detect cracks and possible nitrides, and energy-dispersive X-ray spectroscopy (EDX) to determine the chemical compositions served for the investigations.

The results showed that the Zr-addition to the Al-Zn-Mg alloy led to the mitigation of cracking in the fabricated parts under Ar and N_2. In the parts processed with pure Al-Zn-Mg, elongated cracks occurred along the melt pool centers. This phenomenon was attributed to the liquation cracking mechanism described in the literature. The investigations with the in-situ gas changes unveiled that cracking only happened in the N_2 section of the cuboid (see Figure 5-2). Solid precipitates were found as white areas in the SEM images from all three process gas regions. These were found to be accumulations of Zr. Since they appeared close to cracks in the N_2 region, it was assumed that these could have been Zr nitrides leading to stresses in the microstructures and, ultimately, to cracks. However, as these light areas were found in all process gas regions and the EDX analysis showed no increased N_2 contents, the initial hypothesis could not be proven. The exact mechanism that led to the cracking in the N_2 region remained to be unveiled.

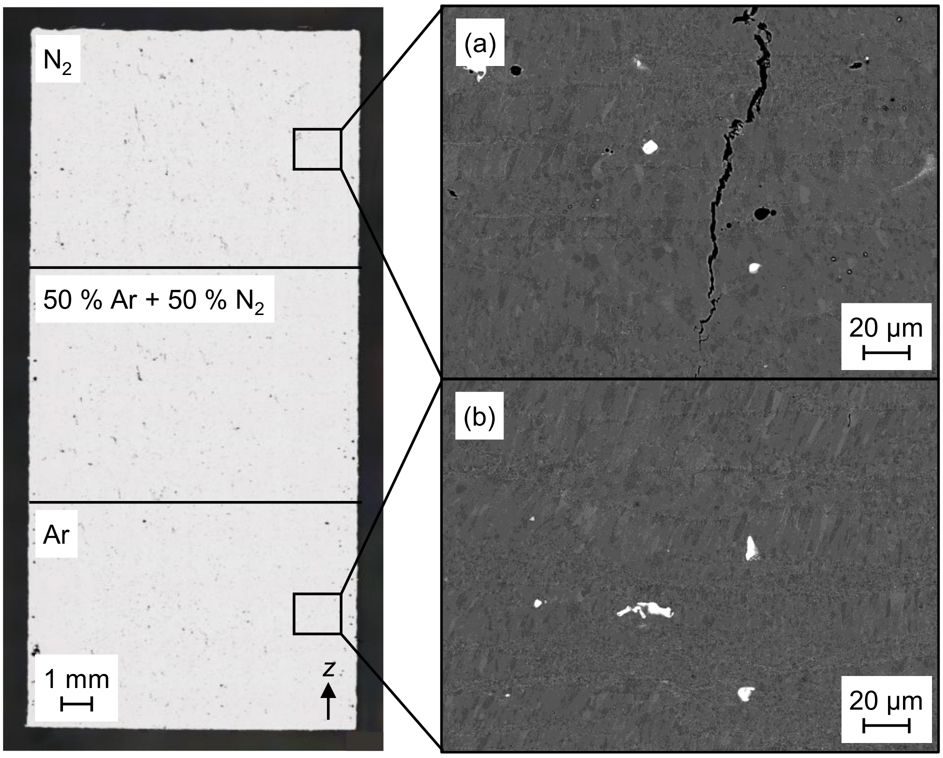

Figure 5-2: Microscopy images of the test sample processed under varying atmospheres within one build job; (a) detailed view of the N_2 section, (b) detailed view of the Ar section, z: building direction (own representation based on BAEHR ET AL. (2021))

Main findings

The main conclusions and research findings of BAEHR ET AL. (2021) were the following:

RF1 Parts from a high-strength Al-Zn-Mg alloy can be manufactured so that they are crack-free via PBF-LB/M under Ar by the addition of 1.2 m% Zr.

RF2 Processing the Zr-blended Al alloy under N_2 leads to cracking in the parts compared to when processing under Ar. It remains to be clarified if this phenomenon can be traced back to Zr nitride formation leading to higher stresses in the microstructure.

Contributions of the authors

Siegfried Baehr was the main author of this publication and presented the results in a talk at the scientific conference *Metal Additive Manufacturing Conference (MAMC)* that took place from November 3 – 5, 2021 in Vienna, Austria. The individual contributions of all authors are listed below:

Siegfried Baehr Conceptualization, Formal analysis, Investigation, Methodology, Validation, Visualization, Writing – original draft

Thomas Ammann Investigation, Methodology

Graham Matheson Investigation

Andreas Wimmer Project administration, Supervision, Writing – review & editing

Michael F. Zaeh Project administration, Supervision, Writing – review & editing

5.2.3 P3: Removal of spatters

Recapitulation

In P3 "Experimental and analytical investigations of the removal of spatters by various process gases during the powder bed fusion of metals using a laser beam" (BAEHR ET AL. 2024a), a two-step approach was applied to comprehensively investigate spatter removal in PBF-LB/M. First, the gas-dependent particle pickup velocity u_{pu} as well as the force F that a gas flow exerts on a spatter were calculated. u_{pu} is the threshold velocity, above which the first powder particle from the powder bed starts to be blown away. In the second step, these theoretical considerations were further investigated experimentally. Therefore, a comparative study between Ar and ArHe30 was performed concerning their ability to remove spatters at various gas flow velocities.

To calculate u_{pu}, the two dimensionless quantities of the particle Reynolds number Re_p and the Archimedes number $Arch$ had to be determined, whereby $u_{pu} = f(Re_p)$ and $Re_p = f(Arch)$. It turned out that an increasing molar fraction of He in Ar leads to an increasing u_{pu}, which offers the potential to apply higher gas flow velocities during PBF-LB/M with those gases while not blowing away the powder bed.

Next, the force F that a gas flow can apply to a spatter particle was evaluated. The two assumptions of spatters being spherical and initially at rest were made. The Stokes equation was utilized for the calculation of F. To improve the comparison of the results, F was normalized with the specific force F that an Ar gas flow with a velocity of $u_g = 2$ m/s exerts to a spatter (considered as the industry standard), resulting in the quantity $\bar{F}$. The results showed that Ar outperforms the He-containing gases in terms of spatter removal capability, since F depends on the gas density. However, as a higher u_{pu} can be reached with He-containing gases, higher values of $\bar{F}$ can theoretically be reached compared to Ar, which could compensate for the beforementioned drawbacks in F.

To further validate and investigate the theoretical considerations, an experimental setup was developed and built. This setup enabled the in-situ collection of spatters during PBF-LB/M by applying a moveable platform cover with a cut-out on the powder bed. Due to the possibility of movement, the cover could be moved upwards and downwards during processing to enable recoating. In the experiments, three cases were studied for both gases, which are summarized in Figure 5-3. In Figure 5-3a, the current industry standard of u_g= 2 m/s is represented, while, in Figure 5-3b, such gas flow velocities were applied that a similar force $\bar{F} = 1$ was reached for all gases. Finally, in Figure 5-3c, an increased $u_g = 3$ m/s was chosen for both gases to showcase the potential of the u_{pu} calculations.

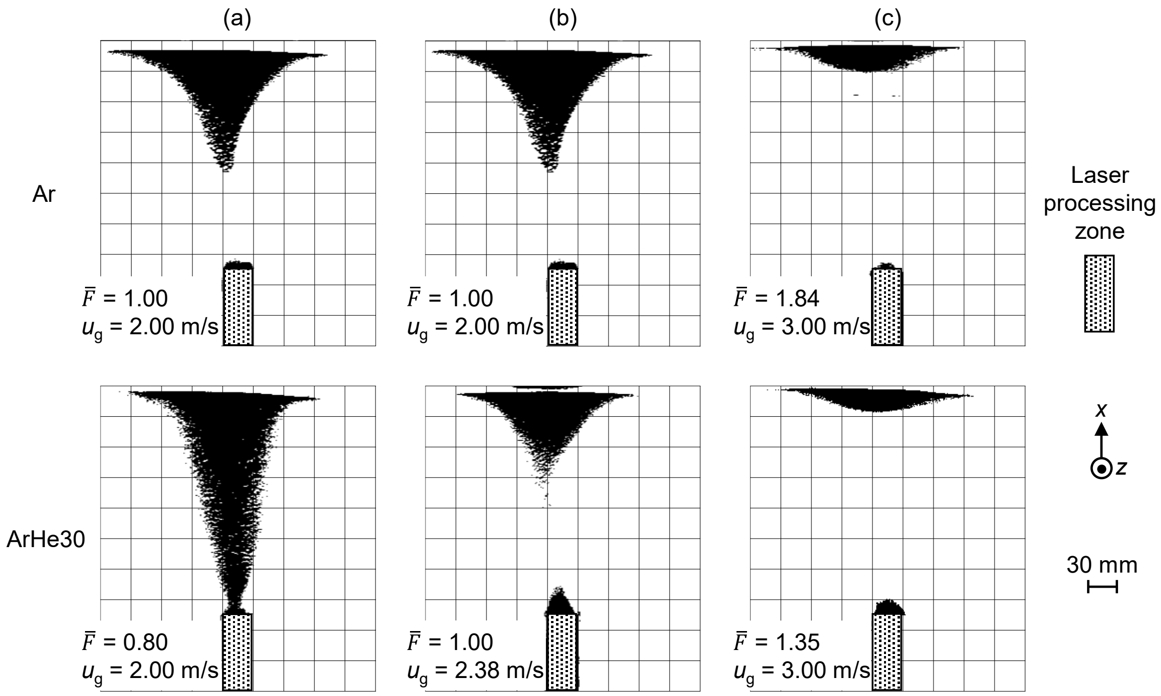

Figure 5-3: Distribution of spatters (black) on the powder bed (white) for Ar and ArHe30 at various conditions; (a) similar gas flow velocity u_g=2 m/s, (b) similar force on spatters $\bar{F}$ = 1, (c) similar gas flow velocity u_g =3 m/s; z: building direction, x: gas flow direction (own representation based on BAEHR ET AL. (2024a))

Main findings

The main conclusions and research findings of BAEHR ET AL. (2024a) were the following:

RF1 The particle pickup velocity correlates positively with an increasing molar fraction of He in Ar.

RF2 A comparable removal of spatters between pure Ar and He-containing gases can be achieved by varying the gas flow velocity.

RF3 With an increased gas flow velocity, which stays below the gas-dependent particle pickup velocity, spatters can be almost completely removed from the powder bed area.

Contribution of the authors

Siegfried Baehr was the main author of this publication. The individual contributions of all authors are listed below:

Siegfried Baehr Conceptualization, Formal analysis, Investigation, Methodology, Validation, Visualization, Writing – original draft

Tobias Klecker Investigation, Methodology

Sebastian Pielmeier Investigation, Methodology

Thomas Ammann Project administration, Supervision, Writing – review & editing

Michael F. Zaeh Project administration, Supervision, Writing – review & editing

5.2.4 P4: Cooling of spatters

Recapitulation

In P4 "Investigations of process by-products by means of Schlieren imaging during the powder bed fusion of metals using a laser beam" (BAEHR ET AL. 2022), the different spatter cooling capabilities of various gases were studied. Based on the fundamentals of heat transfer, the occurring convection, radiation, and conduction were analyzed. Since heat conduction can be neglected in gaseous media, the heat transfer by convection and radiation was focused on. In the first part of the study, a heat transfer model was elaborated that is capable of generally describing the cooling of a single spatter particle by a flow of any gas type. In parallel, a linear Schlieren imaging setup was developed and integrated into a PBF-LB/M machine. This was used in the second part of the study to capture the process under Ar, He, and two mixtures thereof. Finally, video processing was applied to evaluate the cooling of spatters using the experimental data and to compare the observations with the analytical model.

For the heat transfer model, three assumptions were made. Firstly, spatters were assumed to be spherically symmetric. Secondly, a representative relative velocity between the gas flow and the spatter of 10 m/s was assumed based on spatter velocities found in the literature. Lastly, the spatter temperature was fixed at a temperature of 1273.15 K, where Al is in the molten state, and the gas temperature was set to 298.15 K. With these assumptions, the two contributing factors to the total heat flux, radiation and convection, were calculated separately and, finally, summed up. The heat transfer by radiation is a function of the Stefan-Boltzmann constant, the emission coefficient, the surface, and the temperature of the spatter particle and, thus, independent of the gas type. In contrast, the heat transfer by convection highly depends on the gas type. The model included components for natural and forced convection. For the forced convection, individual terms for laminar and turbulent flows were considered. The results showed that the cooling ability of He is about 4.6 times as high as that of Ar. When evaluating the influencing factors on the heat transfer by convection individually, it turned out that an increasing thermal conductivity showed a dominating influence rather than an increasing specific heat capacity. This means that both gases offer a comparable thermal mass and that the higher thermal conductivity of He leads to the enhanced cooling of spatters by He compared to Ar processing gas.

In the experiments, the four gases Ar, ArHe30, ArHe70, and He were applied to the PBF-LB/M process and analyzed using the custom Schlieren imaging setup. The results from this investigation are presented in Figure 5-4, where a single frame from each process is shown. It became evident that, with an increasing fraction of He in the processing gas, the amount of vapor produced during processing could be reduced. Also, less incandescent spatters were tracked in the He process, which coincided with the analytical results of a higher cooling ability of He.

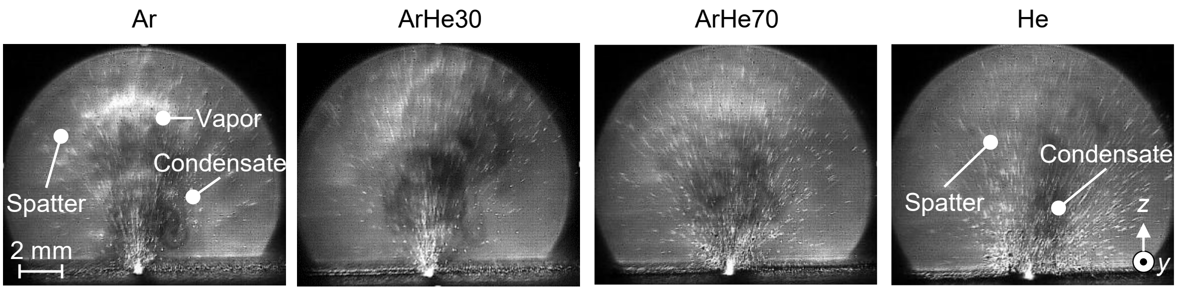

Figure 5-4: Schlieren imaging snapshots captured at the same point in time from the PBF-LB/M processes under Ar, ArHe30, ArHe70, and He with no gas flow; y: scanning direction (own representation based on BAEHR ET AL. (2022))

Main findings

The main conclusions and research findings of BAEHR ET AL. (2022) were the following:

RF1 The cooling of spatters is by a factor of about 4.6 times stronger when using He compared to Ar.

RF2 The heat transfer is mainly influenced by the thermal conductivity rather than by the specific heat capacity.

RF3 Less incandescent spatters and a weaker vapor plume appear during processing under He compared to Ar.

Contribution of the authors

Siegfried Baehr was the leading author of this publication and presented the results in a talk at the scientific conference *International Congress on Applications of Lasers & Electro-Optics (ICALEO)* which was held from October 17 – 20, 2022 in Orlando (Florida), USA. The individual contributions of all authors are listed in the following:

Siegfried Baehr	Conceptualization, Formal analysis, Investigation, Methodology, Validation, Visualization, Writing – original draft
Lukas Melzig	Investigation
Dominik Bauer	Investigation, Methodology
Thomas Ammann	Project administration, Supervision, Writing – review & editing
Michael F. Zaeh	Project administration, Supervision, Writing – review & editing

5.2.5 P5: Heat balance of the melt pool

Recapitulation

In P5 “Investigations on the Heat Balance of the Melt Pool during PBF-LB/M under Various Process Gases” (BAEHR ET AL. 2024c), experimental and numerical investigations on the resulting melt pool characteristics of a high-strength Al alloy processed via PBF-LB/M under Ar, ArHe30, ArHe70, and He were performed. A two-step approach was applied. In the first step, a validated SPH simulation model was extended by means of integrating various atmospheres and then used to study the occurring melt pool surface temperatures and dimensions. To validate the numerical results, an experimental study using pyrometry was performed. Cross-sections of the fabricated single lines and the surface temperature measurements acquired via pyrometry were utilized to deliver similar types of results as received from the simulation. In the second step of the study, the SPH simulation model was applied to study PBF-LB/M phenomena that are not accessible via experiments. The cooling rates, the temperature field, and the heat transfer within the melt pool and its surroundings were extracted from the numerical results to compare the influences of various gases.

The comparison of the experimental and numerical findings in the first part of the study unveiled that the SPH simulation model reflects reality well in the given use case. Temperatures in the order of magnitude of 1200 K were found at the melt pool surface with a slight trend towards lower temperatures with an increasing He-fraction in the process atmosphere. A similar trend occurred for the melt pool dimensions. Melt pool widths in the range of 180 – 195 µm and depths in the range of 141 – 160 µm were determined on the single line cross-sections. The results indicated a conduction melting regime with the parameters used.

After validating the simulation model, the temperature fields in longitudinal cross-sections were studied. It was found that the temperature fields in the gas phase differed significantly showing the increased heat transport ability of He compared to Ar. Furthermore, a more rapid decrease of the temperature was detected in the direction of the substrate. These findings were corroborated by the acquired results on the temperature rates (see Figure 5-5). As it can be seen in Figure 5-5, high cooling rates were more likely towards the substrate. The highest heating rates of up to 10^8 K/s were found in the vicinity of the laser beam interaction zone. For the melt pool surface, cooling rates between 10^5 and 10^6 K/s occurred, which were comparable to those found in the literature. The comparison between the gases confirmed the results from the previous publications that heat is dissipated better in He than in Ar, as the temperature rates in the gas phase were found to be highest under He. In the final step, an integral heat balance was applied to the melt pool. The results showed that approximately 95 % of the input energy by the laser is dissipated via conduction into the substrate, while only approximately 5 % dissipate by convection into the gas phase. Thereby, the heat transfer into the He gas phase exhibited slightly higher values than that into the Ar gas phase.

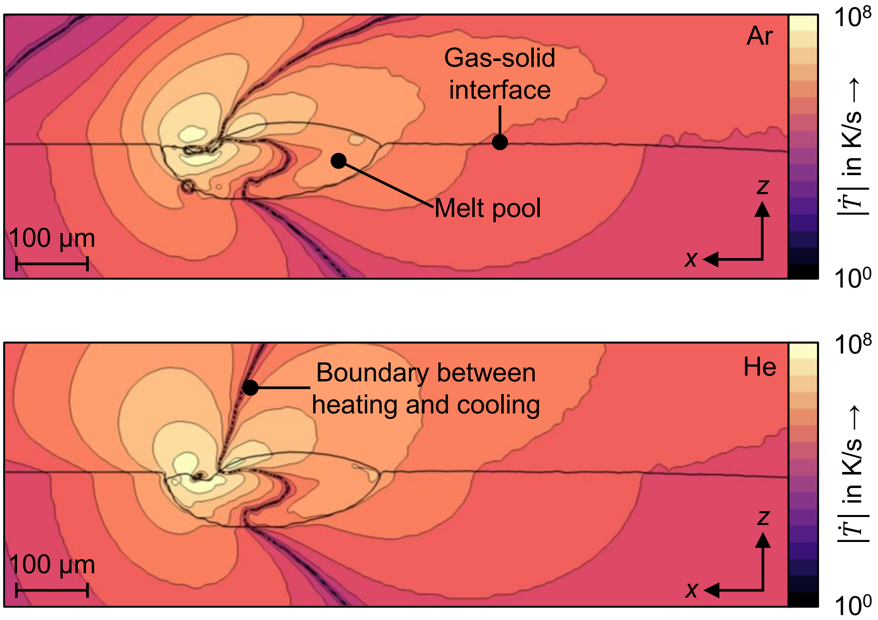

Figure 5-5: Logarithmic representation of the rates of temperature change $|\dot{T}|$ under Ar and He in a cross-sectional view of the PBF-LB/M process zone (the black iso surface line separates zones of heating (left of it) and cooling (right of it)); (neg.) x: (gas flow) scanning direction, z: building direction (own representation based on BAEHR ET AL. (2024c))

Main findings

The main conclusions and research findings of BAEHR ET AL. (2024c) were the following:

RF1 Slightly lower melt pool surface temperatures and dimensions were found experimentally and numerically when He was used instead of Ar as the process gas.

RF2 Temperature change rates of up to 10^8 K/s in the vicinity of the laser beam interaction zone and between 10^5 and 10^6 K/s on the melt pool surface were determined by the SPH simulation model. Only minor differences were found between the gases.

RF3 The heat transfer by conduction into the substrate contributes approximately 95 % to the overall heat transfer. The remaining 5 % are contributed by the convective heat transfer into the gas phase, whereby higher values were found for processing with He than for processing with Ar.

RF4 It was determined that a power of approximately 42 W was introduced into the material with a nominal laser power of 200 W for all gases. This resulted in an average effective absorptivity of the material of 0.238.

Contribution of the authors

Siegfried Baehr and Fabian Fritz are shared leading authors of this publication. The individual contributions of all authors are listed below:

Siegfried Baehr Conceptualization, Formal analysis, Investigation, Methodology, Validation, Visualization, Writing – original draft

Fabian Fritz	Conceptualization, Formal analysis, Investigation, Methodology, Validation, Visualization, Writing – original draft
Thomas Ammann	Supervision, Writing – review & editing
Stefan Adami	Supervision, Writing – review & editing
Nikolas A. Adams	Project administration, Supervision, Writing – review & editing
Michael F. Zaeh	Project administration, Supervision, Writing – review & editing

5.2.6 P6: Enhanced processing of a novel high-strength aluminum alloy

Recapitulation

For P6 "Influence of argon, helium, and their mixtures on the powder bed fusion of an Al-Cu-Li-Ti alloy using a laser beam: evaporation, microstructure, and mechanical properties" (BAEHR ET AL. 2024b), it was investigated to what extent the PBF-LB/M process capability can be enhanced by using He-containing gas mixtures. To assess this research question, a full-factorial experimental plan was set up in the first part of the study, varying three process parameters between three levels. The laser power, the scanning velocity, and the hatch distance were varied while keeping the layer thickness constant. Each of the 27 resulting parameter sets was applied to one cuboid placed on the build platform. After processing, the densities of the cuboids were measured by the Archimedes principle and by image analysis on polished cross-sections. Based on these results, the parameter set leading to the highest density was selected and applied to the build job layout of the second part of the study. Bars with a hexagonal cross-section were manufactured. These were machined afterwards for static tensile tests to the shape of a standardized tensile bar. Electron backscatter diffraction (EBSD) and EDX were applied to the specimens to determine the grain sizes and the distributions of elements, respectively. SEM additionally supported the analysis of the powder and the solidified material.

Overall, the processing under a He-containing atmosphere led to several benefits. The higher cooling ability of He with respect to spatters and fumes was visible on process images. This can be seen in the comparison of the processing with Ar and He according to Figure 5-6. In the He process, a visibly lower process lighting appeared.

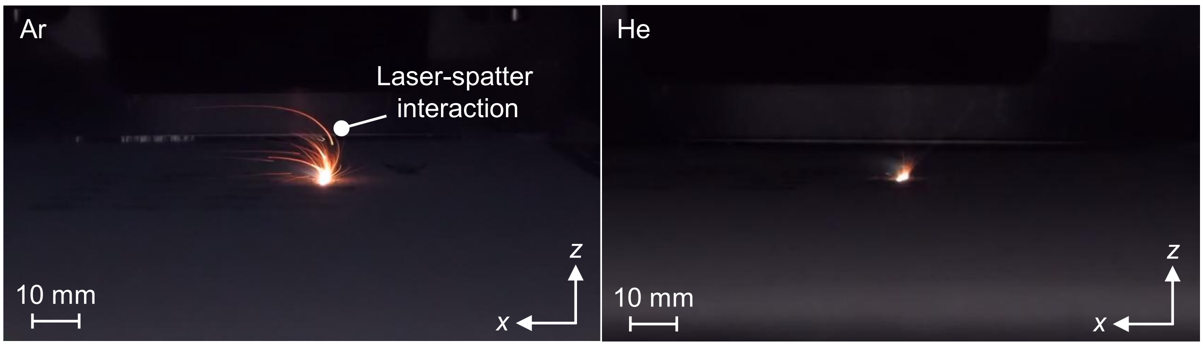

Figure 5-6: Process images captured at the same point in time by a digital camera for Ar and He; x: gas flow direction, z: building direction (own representation based on BAEHR ET AL. (2024b))

The results from the metallographic evaluation showed that the use of He led to overall higher densities over a wide range of *VED*s compared to Ar. This could be a result of the weaker interactions of the laser beam with process by-products. Relative densities of 97.6 – 99.8 % and 98.6 – 99.8 % were determined for Ar and He, respectively. In contrast, no significant differences were found for the evaporation of volatile elements. The highest evaporative losses were found for the elements Zn and Mg. When studying the microstructure via EBSD, a shift towards smaller grain size classes was found in the samples processed under He compared to Ar. This observation was attributed to the higher cooling abilities of He. Finally, the static tensile tests supported the results so far as they indicated a trend towards higher YS and UTS values of parts processed with an increasing He-fraction in the atmosphere (see Figure 5-7). YSs and UTSs in the ranges of approximately 400 to 420 MPa and 400 to 410 MPa, respectively, were found. The values for the elongation at break were between 13 and 14 %.

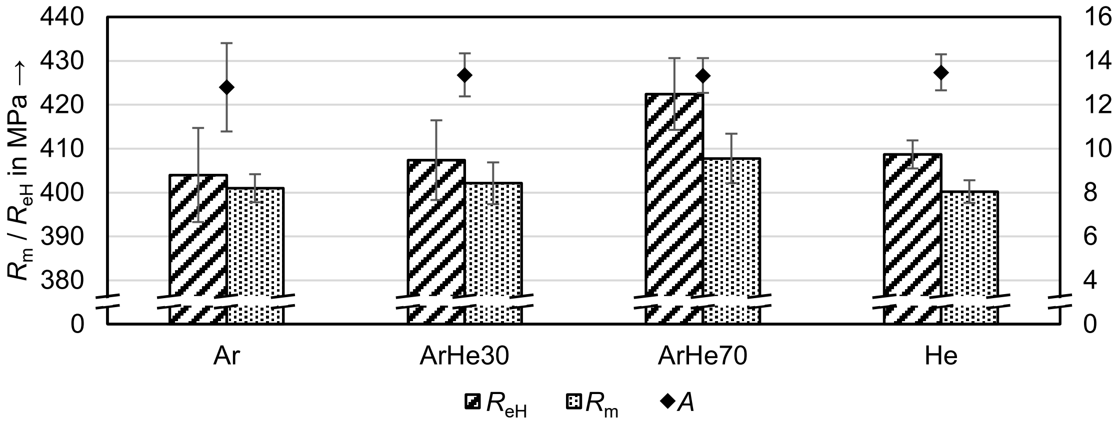

Figure 5-7: Results from the static tensile tests for samples processed under Ar, ArHe30, ArHe70, and He via PBF-LB/M (the mean values and standard deviations are indicated); R_{eH}: yield strength, R_m: tensile strength, A: elongation at break (own representation based on BAEHR ET AL. (2024b))

Main findings

The main conclusions and research findings of BAEHR ET AL. (2024b) were the following:

RF1 An increasing content of He in Ar-He gas mixtures leads to higher part densities and slightly higher penetration depths.

RF2 A refined microstructure and a higher yield and tensile strength occur when using increasing He contents in Ar-He gas mixtures.

RF3 The use of He-containing gas mixtures has no significant detrimental influence on the evaporation of volatile alloying elements.

Contribution of the authors

Siegfried Baehr was the leading author of this publication. The individual contributions of all authors are listed in the following:

Siegfried Baehr Conceptualization, Formal analysis, Investigation, Methodology, Validation, Visualization, Writing – original draft

Graham Matheson Investigation, Methodology, Visualization, Writing – original draft

Thomas Ammann Supervision, Writing – review & editing

Peter Mayr Project administration, Supervision, Writing – review & editing

Michael F. Zaeh Project administration, Supervision, Writing – review & editing

5.3 Discussion of the findings

In this section, the results of the six key-publications are discussed with regard to the state of the art prior to this dissertation project. Furthermore, the achievement of the three SOs is documented. The obtained results were clustered by using the research field that they contributed to according to Figure 5-8. The research fields are defined as influences of the process gas on the melt pool, spatter particles as well as process and parts, whereby each field is further detailed and divided by experimental and analytical or numerical works.

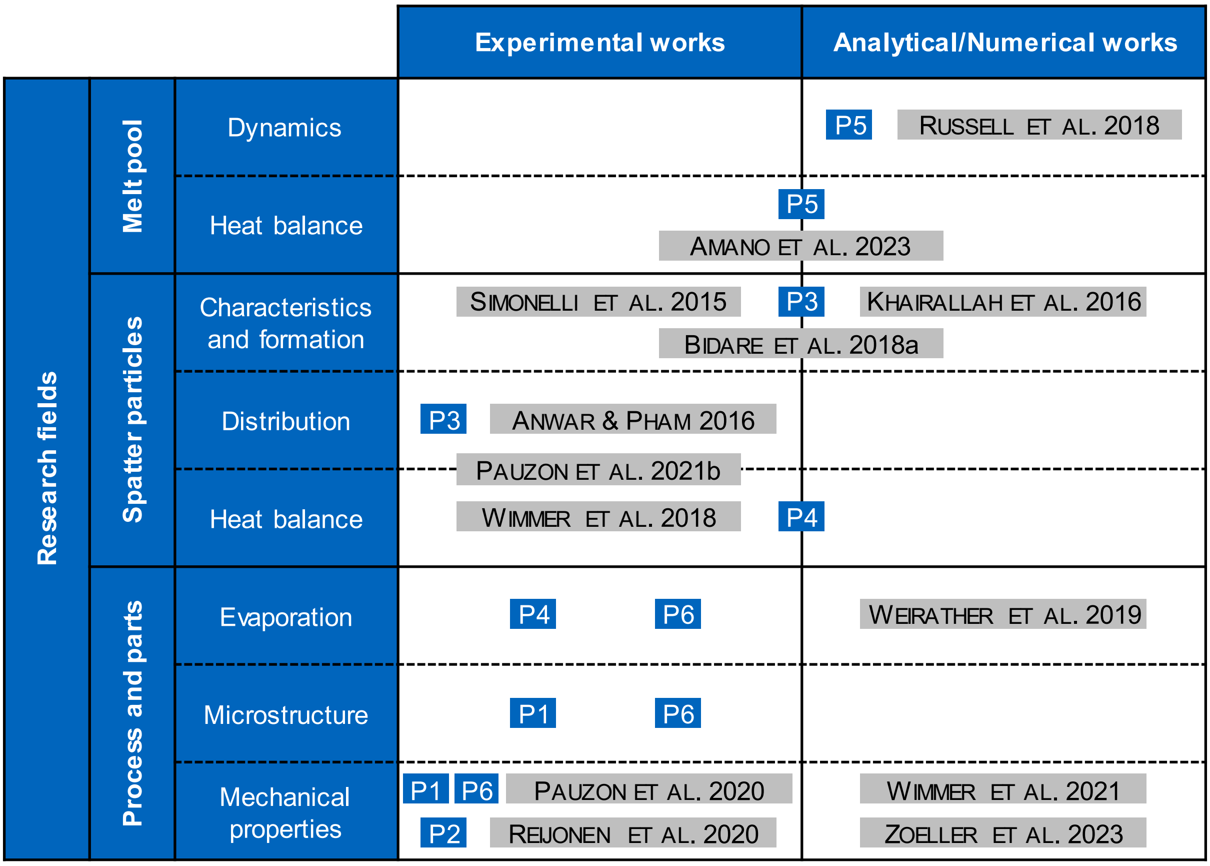

Figure 5-8: Classification of the six key-publications P1 – P6 as well as selected related publications from the state of the art according to their contribution to a research field (ordinate) and their type of work (abscissa)

The first two publications P1 and P2 from stage 1 of this thesis (cf. Section 4.4) contained preliminary experimental investigations on the influences of He and N_2, respectively, compared to Ar on the PBF-LB/M process. As shown in Figure 5-8, they contributed to the research field *Process and parts*, since the resulting part properties of 3.2381 (P1) and an Al-Zn-Mg alloy (P2) were investigated. He has shown promising experimental results during the processing of 3.2381 and 3.7164 in WIMMER ET AL. (2018) and PAUZON ET AL. (2020), respectively, where a higher process stability, increased cooling rates, and decreased numbers of tracked spatters were found for Ar-He gas mixtures compared to Ar. In P1, indications for proofs that these findings are transferable were discovered. Smaller sizes of the material's well-known cellular grain substructure and higher static mechanical properties under a He-containing gas compared to Ar contributed to this theory. In parallel, similar part qualities with regard to the porosity and hardness were achieved. In contrast, P2 was dedicated to another standard gas for PBF-LB/M, N_2, and its influence on the processing of a Zr-blended Al-Zn-Mg alloy. There, a possible chemical reaction of the process gas with the alloy (unfavorable formation of nitrides as they could act as crack initiation locations) was investigated using a novel gas mixing setup that went beyond the state of the art. However, the results did not lead to a clear indication of the creation of nitrides, which is why the focus of the further studies was placed on He and Ar-He mixtures.

P3 to P5 continued the investigations on He-addition to the process gas and focused on thoroughly elaborating one scientific aspect each. P3 from stage 2 (cf. Section 4.4) analytically and experimentally described spatter removal by the process gas flow and, thereby, contributed to the sub-classified research fields of *Characteristics and formation* as well as *Distribution*. Findings similar to the works from ANWAR & PHAM (2018) or LADEWIG ET AL. (2016) were found, as higher gas flow velocities lead to a better removal of spatters. The approach of P3 went beyond the state of the art, as the spatter removal capability of any gas-material combination with respect to the individual u_{pu} was described analytically. In parallel, a novel and unique experimental setup was elaborated to capture the real spread of spatters that were separated from the powder bed. That device differed significantly from other works from the state of the art, such as ANWAR & PHAM (2018), as it was not based on analyses of powder-spatter mixtures. Thus, this analytical and experimental approach enabled studying the spread of spatters over the build platform as well as their characteristics and mass under varying gas flow velocities and types. The experimental findings validated the elaborated model and showed that it is possible to overcome the drawbacks of the lower density of He when it comes to spatter removal by increasing the gas flow velocity in the region below u_{pu}. The generalized model approach delivers a possibility to properly adjust the gas flow velocity. In summary, P3 meets the SO1 that was defined in Section 4.2.

P4 and P5 were dedicated to the global topic of the heat balance in the PBF-LB/M process, whereby the publications contributed to the two research fields *Spatter particles* and *Melt pool*, respectively (see Figure 5-8). In P4, an analytical heat balance model for the description of spatter cooling by the gas flow for any gas-material combination was elaborated. To validate the model, a Schlieren imaging setup was built and applied in combination with an image analysis approach to determine the cooling capability of various gases. In contrast to the high-speed or Shadowgraphy imaging approaches from WIMMER ET AL. (2018) or PAUZON ET AL. (2021b), the chosen approach added value by enabling the study of temperature gradients in the atmosphere that are otherwise invisible. The experimental results confirmed the analytical findings from the heat balance model. P4 delivered new knowledge in addition to what was known from the state of the art, as the model quantitatively described the superior spatter cooling abilities of He compared to Ar quite well. Other findings of the study, such as less incandescent spatters and a weaker vapor plume occurring during processing, were found to be consistent with the experimental results from TRAORE ET AL. (2021) or PAUZON ET AL. (2022b). The publication

P5, which contributed to the sub-classified research fields of *Heat balance* and *Dynamics*, experimentally and numerically provided the heat balance and flow of the melt pool during PBF-LB/M under Ar and He via SPH modeling and pyrometry as well as metallography, respectively. Compared to other works using SPH modeling from the state of the art, such as WEIRATHER ET AL. (2019) or ZÖLLER ET AL. (2023), the gas phase was additionally considered in the chosen approach in P5. This enabled drawing conclusions on the convective heat transfer by the gas flow and, thus, delivered a possibility to study the overall heat balance of the PBF-LB/M melt pool. The novel and unique results from the simulations quantified the temperature rates occurring simultaneously in the melt pool, substrate, and gas phase. Furthermore, the individual contributions of the heat transfers by convection and conduction could be determined. The results specified the slightly increased cooling capacity of He compared to Ar as hypothesized in P1 and indicated by AMANO ET AL. (2021a). In contrast to the hypothesis of lower recoil pressures under He depicted in Figure 3-4, no significant differences were found in the melt pool dynamics or shapes within this thesis. In summary, SO2 from Section 4.2 can be considered as achieved with the addressed results from P4 and P5.

The publication P6 was dedicated to experimentally reviewing the findings from P3 – P5 by studying the processing of a high-strength Al alloy via PBF-LB/M under Ar and He. Using qualitative image analyses, the enhanced spatter cooling capability of He compared to Ar could be observed. Suitable destructive testing methods proved the increased melt pool cooling capability of He compared to Ar, as a refined microstructure and slightly increased static mechanical properties were determined. Indications towards a higher process stability with colder melt pools under He were derived by the overall higher part density levels and the constant chemical composition of those parts. The findings gave proof to the analytical achievements from P3 – P5 and were underlined by experimental results from the previous state of the art, such as from AMANO ET AL. (2021a) or PAUZON ET AL. (2022b). P6, thereby, met the requirements formulated in SO3 in Section 4.2.

5.4 Economic assessment of part costs with regard to process gases

In order to assess the economic impact of a change in the process gas on the overall costs per part, a holistic cost model of the entire PBF-LB/M process chain needs to be considered. Such a model needs to include costs related to the setting up and the running of a PBF-LB/M laboratory (e.g., purchase, installation, and maintenance of the printer and its periphery, depreciation costs), processing as well as post-processing costs (e.g., energy consumption, gas usage, material costs), or costs of labor work. In the work of PARENTI ET AL. (2024), such a cost model for PBF-LB/M was presented. In a case study, the authors compared the costs for the fabrication of a filigree, lightweight impeller made of the material 17-4 PH stainless steel using single-laser PBF-LB/M, multi-laser PBF-LB/M, and fused filament fabrication. The overall cost function C was formulated to be

$$C = C_{\mathrm{eq}} + C_{\mathrm{fac}} + C_{\mathrm{setup}} + C_{\mathrm{mat}} + C_{\mathrm{en}} + C_{\mathrm{gas}} + C_{\mathrm{cons}} + C_{\mathrm{pp}} + C_{\mathrm{lab}}\,, \quad (53)$$

with the costs of the equipment C_{eq}, the costs of the facility C_{fac}, the costs of the setup of the process C_{setup}, the material costs C_{mat}, the energy consumption costs C_{en}, the gas costs during processing C_{gas}, the consumables costs C_{cons}, the post-processing costs C_{pp}, and the labor work costs C_{lab}.

Considering the scope of this dissertation project, where the gas usage is only compared during the actual processing step, the costs for the purchase, the installation, the maintenance, and the use of a commercially available single-laser PBF-LB/M printer and its periphery (C_{eq}, C_{fac}, C_{setup}, C_{en}, C_{cons}, C_{lab}, and C_{pp}) were assumed to be consistent to the input data from PARENTI ET AL. (2024). For more details on the calculation and input data of these cost terms, the reader is kindly referred to the literature (PARENTI ET AL. 2024).

In contrast to the literature, the following assumptions were made for the remaining cost terms for the cost calculation within this dissertation project:

- For C_{mat}, the material costs per kilogram were adapted to represent the processing of an aluminum alloy. For this, the price of the alloy AlSi10Mg of approximately 50 €/kg was considered (EOS GMBH 2024).
- The term C_{gas} was extended by the time that the machine needs to purge the build chamber to reach the desired level of remaining oxygen in the atmosphere. Thus, C_{sec} is given by

$$C_{gas} = \frac{(t_{purge} \cdot \dot{V}_{purge} + t_{build} \cdot \dot{V}_{build}) \cdot c_g}{n_b \cdot (1 - f)}, \tag{54}$$

  with the durations of purging and processing t_{purge} and t_{build}, respectively, the volume flow rates of the gas during purging and processing $\dot{\boldsymbol{V}}_{\mathbf{purge}}$ and $\dot{\boldsymbol{V}}_{\mathbf{build}}$, respectively, the cost of gas per volume c_g, the number of parts per build job n_b, and the scrap rate f.
- The values for the variables in the Equation (54), except for $\dot{\boldsymbol{V}}_{\mathbf{purge}}$, $\dot{\boldsymbol{V}}_{\mathbf{build}}$, and c_g, were taken from PARENTI ET AL. (2024). $\dot{\boldsymbol{V}}_{\mathbf{purge}}$ and $\dot{\boldsymbol{V}}_{\mathbf{build}}$ were set to 3 m^3/h and 0.6 m^3/h for all gases, respectively.
- The cost of Ar per volume c_g was derived from internal data of the *iwb* and set to c_g = 2.50 €/m^3. Publicly available gas prices from gas manufacturer websites are usually not very meaningful in this comparison, since gas pricing is individual and depends on several factors, such as the volatile availability of gases as well as on the customer-supplier relationship. Due to a lack of alternatives, to be able to compare the influences of different gases on the costs per part, nevertheless, the factors by which ArHe30, ArHe70, or He are more expensive than Ar were calculated from data available online (LINDE GMBH 2024). The factors are given in Table 3 (a). The resulting gas costs per volume are listed in Table 3 (b).

Table 3: (a) Factors of price increases of He-containing gases compared to Ar, (b) gas costs per volume

(a)

Gas	Price of a bundle in € (LINDE GMBH 2024)	Factor
Ar	3,151	-
ArHe30	6,773	2.15
ArHe70	9,569*	3.04
He	12,320	3.91

*calculated value: 0.3 · (price of an Ar bundle) + 0.7 · (price of a He bundle)

(b)

c_g in €/m³
2.50
5.38
7.60
9.78

Using Equation (53) and the above-mentioned assumptions, the costs per part were calculated for the use case of PARENTI ET AL. (2024). Figure 5-9 depicts an overview of the structure of the costs per part, given in shares of the total costs. As it can be seen, the costs for the equipment and for the laboratory account for approximately 60 % of the part costs for all gases (C_{lab} + C_{cons} + C_{setup} + C_{fac} + C_{eq}). The second and third largest contributors are the post-processing costs C_{pp} and the material costs C_{mat}, respectively. The energy costs C_{en} are minor contributors for all gases.

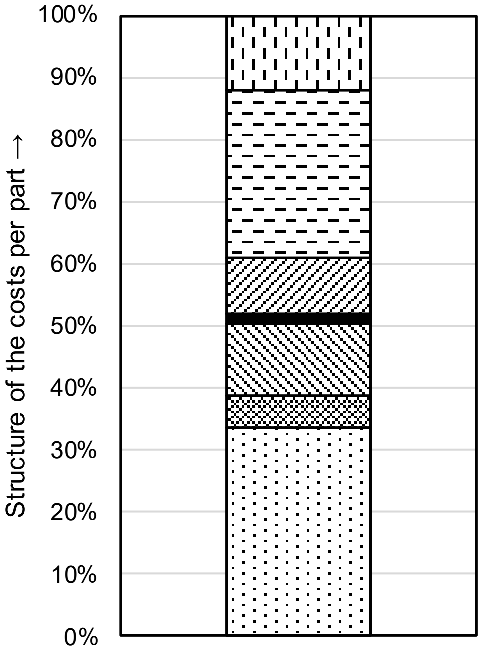

Cost term	Share of the costs per part in % Ar	ArHe30	ArHe70	He
C_{lab}	12.30	12.25	12.21	12.17
C_{pp}	27.34	27.22	27.13	27.04
C_{cons}	9.00	8.96	8.93	8.90
C_{gas}	0.38	0.81	1.13	1.45
C_{en}	0.11	0.11	0.11	0.11
C_{mat}	11.68	11.63	11.59	11.55
C_{setup}	5.12	5.10	5.08	5.07
C_{fac}	0.15	0.15	0.15	0.15
C_{eq}	33.93	33.78	33.67	33.56

Figure 5-9: Exemplary cost structure of a part manufactured by PBF-LB/M (use case adapted from PARENTI ET AL. (2024))

The costs for the gas usage differ between the gases considered and are highlighted in the color orange in Figure 5-9. For Ar, the share of the costs per part is the lowest with 0.38 %. With an increasing fraction of He, C_{gas} increases and accounts for 1.45 % of the part costs for pure He. This corresponds to a near quadrupling of the cost share. However, considering the overall costs per part, this share is still comparably low.

In the publications P3 – P6 of this dissertation project, the advantages of using He-containing gas mixtures in the PBF-LB/M process were highlighted. Since small fractions of He in Ar already enhance the process capability, such as the use of ArHe30, the cost increase is considered to be acceptable for the given use case.

6 Summary and outlook

6.1 Summary

The PBF-LB/M process is a promising manufacturing technology for future high-performance applications. Its layer-by-layer procedure enables the one-step fabrication of near-net-shape parts with complex geometries and integrated functionalities. The various physical phenomena occurring in the process zone require a careful selection of the process parameters to ensure a stable process. Besides primary parameters, which have been thoroughly studied in the literature, such as the laser power or the scanning velocity, influences from the material composition or the ambient atmosphere need to be taken into account. The latter factor has in part been investigated in experimental studies constituting the state of the art. However, the analytical and generalized knowledge about the intricate underlying physical interactions between the atmosphere and the process is required to fully exploit the benefits of PBF-LB/M.

The underlying idea of this dissertation was to enhance the process capability of PBF-LB/M by elaborating generalized models for the description of the interactions between the atmosphere and the process. The scientific findings and models aimed at providing decision supports for a suitable choice of the process gas type and flow. The research approach of this thesis was based on four stages. In stage 1, preliminary experimental investigations on the influences of He and N_2 compared to Ar on the processing of Al alloys via PBF-LB/M were performed. For this purpose, a suitable experimental setup including a novel gas mixing device was applied. The main findings of the first stage were the following:

- Processing with He-containing gases rather than with Ar leads to a refined microstructure. This was attributed to hypothesized higher cooling rates under He compared to Ar.
- Increased static mechanical properties under He-processing were determined. These were assumed to occur following a hardening effect due to the refined microstructure.
- No significant differences between Ar and N_2 processing were found.

Based on the findings of stage 1, the stages 2 and 3 were dedicated to unveiling the differences in the underlying interactions when processing with Ar and He. Therefore, in stage 2, a unique experimental setup was employed to experimentally study the spatter removal and distribution on the powder bed. The experiments built upon an analytical model describing the spatter removal under various gases and were performed in such a way that the differences between Ar and He could be observed. The most important findings of stage 2 were the following:

- He-addition to the process gas enables higher gas flow velocities compared to pure Ar processing, since the particle pickup velocity increases.

- With comparable gas flow velocities, the removal of spatters was better with Ar than with He. However, due to the increased particle pickup velocity, a similar removal could be reached with He by increasing the gas flow velocity.
- For both gases, it could be nearly fully avoided that spatters land on the powder bed by increasing the gas flow velocity while staying below the gas-dependent limits.

In stage 3, the cooling of spatters and of the melt pool by the process gas was investigated. This was done by applying suitable process monitoring devices, namely Schlieren imaging and pyrometry, and analytical approaches to study the occurring heat balances. For spatter cooling, a formula-based model was elaborated, while an SPH model was employed to investigate the heat balance of the melt pool. The main research findings of stage 3 are summarized as follows:

- The use of He leads to a faster cooling of spatters and the melt pool compared to the use of Ar. The effect was significantly stronger for the spatter cooling.
- The melt pool surface temperatures and dimensions were slightly decreased when using He instead of Ar.
- The heat transfer into the gas atmosphere by convection contributed approximately 5 % to the overall heat transfer, while the heat transfer by conduction into the underlying substrate accounted for approximately 95 % of the total heat transfer.

Stage 4 concluded the research of this dissertation. An experimental study based on a statistical experimental design and suitable destructive testing methods (e.g., metallography, SEM, EBSD) aimed at reviewing the benefits of applying He which were found in the stages 1 – 3. The increased process capability was evaluated by determining various part properties, such as the density, chemical composition, microstructure, or static mechanical properties. The main findings of stage 4 were the following:

- Less incandescent spatters were observed in the He process.
- Overall higher part densities over a wide range of *VED*s were found in He-processed parts compared to Ar-processed parts.
- Smaller grain sizes and higher static mechanical properties were determined for the parts processed under He compared to Ar, while the chemical composition remained constant.

In summary, the results of this dissertation have provided a decisive step towards an improved and targeted use of the process gas as a parameter in the PBF-LB/M process.

6.2 Outlook

In the following, two proposals on future research possibilities as well as one industrial application perspective are derived based on the knowledge gained in this dissertation.

Research possibilities

- In P6, metal vaporization has shown to be minorly influenced by the choice of the process gas type. Thus, a sufficiently high gas flow velocity has to be set to ensure the proper removal of the vapor plume and an unhindered laser energy input. This phenomenon is especially relevant when processing alloys with alloying elements with low boiling points. In this work, these were, for example, the elements Zn or Mg. The evaporative losses were found to be the highest for these elements. Another parameter of the atmosphere in the PBF-LB/M process that remained untouched within this work is the ambient pressure. This parameter has hardly been studied in the literature. A rare example is the work of BIDARE ET AL. (2018b). In their work, the authors used a self-built high-pressure PBF-LB/M chamber to process under increased ambient pressures of 3 and 5 bar with Ar and He. The study showed promising results with regard to the suppression of spatter creation but highlighted remaining challenges, such as the increased process temperatures and the creation of plasma. The creation of plasma was highly influenced by the choice of the process gas with He leading to less plasma. In this field, an open research area was identified. The underlying mechanisms of the dependencies between an increased ambient pressure and relevant process phenomena, such as the suppression of metal vaporization due to increased boiling points of the elements, have to be uncovered for various gases. A step-wise increase of the ambient pressure should be considered to determine the minimum increase required to benefit from this parameter.

- The results of this thesis have shown benefits in the use of various inert gases. The study described in P2 on the use of the slow-to-react N_2 in Al processing via PBF-LB/M has shown little indications concerning the benefits of the use of other than inert gases. In general, the use of active gases for the PBF-LB/M process has hardly been studied in the literature. Although those gases are well-established in other welding processes, such as LW, due to their positive effect on the process stability or productivity, their application to PBF-LB/M is limited so far. Few works, such as the study from ABEL ET AL. (2020), have investigated potential interactions. Their work showed the first benefits of adding hydrogen to Ar for the processing of a Mg alloy. Other gases that have proven beneficial for LW, such as CO_2, remain to be studied. This gas, in particular, can dissociate into CO and O during high-energy LW leading to increased penetration depths, as shown by CHUNG ET AL. (1999) (cf. Section 3.5). Here, an open research area is to be seen. The dissociation of those gas molecules requires high energies. These can occur, for example, due to increased process temperatures in LW applications. In the PBF-LB/M industry, an increasing need for increased productivity is arising. This can exemplarily be addressed by the use of high-power lasers to increase layer thicknesses or hatch distances and, thus, decrease the number of layers or the layer time. In these processes, heat accumulation arises as a growing challenge but might offer a chance to exploit the benefits of active gases. Thus, a study dedicated to unveiling the interactions of active gases in high-power PBF-LB/M processes should be considered in future research.

Industrial application

For the industry, two significant barriers to implementing PBF-LB/M into production are the low reproducibility of part properties and the comparably high processing times. The latter can be addressed either by altering the process parameters (i.e., increasing the layer thickness or the scanning velocity) or by applying multi-laser systems. These systems are increasingly being studied due to the fact that the processing time can, in theory, be reduced by splitting up the build platform into multiple sectors and illuminating each with a single laser (KHORASANI ET AL. 2020). However, various challenges of this approach appear, such as more process by-products being created, a stronger heating up of the process zone and its surroundings, or hard-to-identify scanning patterns in the overlapping zones (PFALZ ET AL. 2023). This can further deteriorate the reproducibility of the part properties. The results of this thesis have shown benefits in using He-containing gases to enhance the PBF-LB/M process capabilities. Especially the observed findings of overall higher relative part densities that were attributed to fewer process by-products and a calmer melt pool could be exploited further to minimize the current drawbacks in the use of multi-laser systems. An initial step towards this could be a proper analysis and improvement of the gas flow field in the build chamber used by adjusting the machine hardware for an optimized use of the low-density He (e.g., optimizing the inlet nozzle or installing a high-power pump). The method presented in P3 could then be applied to a certain material to determine a suitable gas flow velocity.

References

Please note that wherever bibliographic indices are missing, the information is not available or not known to the author.

ABEL ET AL. 2020
Abel, A.; Wessarges, Y.; Julmi, S.; Hoff, C.; Hermsdorf, J.; Klose, C.; Maier, H. J.; Kaierle, S.; Overmeyer, L.: Laser powder bed fusion of WE43 in hydrogen-argon-gas atmosphere. Procedia CIRP 94 (2020), pp. 21–24.

AFRASIABI ET AL. 2021
Afrasiabi, M.; Lüthi, C.; Bambach, M.; Wegener, K.: Multi-Resolution SPH Simulation of a Laser Powder Bed Fusion Additive Manufacturing Process. Applied Sciences 11 (2021), pp. 1–20.

AFRASIABI ET AL. 2022a
Afrasiabi, M.; Keller, D.; Lüthi, C.; Bambach, M.; Wegener, K.: Effect of Process Parameters on Melt Pool Geometry in Laser Powder Bed Fusion of Metals: A Numerical Investigation. Procedia CIRP 113 (2022), pp. 378–384.

AFRASIABI ET AL. 2022b
Afrasiabi, M.; Lüthi, C.; Bambach, M.; Wegener, K.: Smoothed Particle Hydrodynamics Modeling of the Multi-layer Laser Powder Bed Fusion Process. Procedia CIRP 107 (2022), pp. 276–282.

AHN ET AL. 2017
Ahn, J.; He, E.; Chen, L.; Dear, J.; Davies, C.: The effect of Ar and He shielding gas on fibre laser weld shape and microstructure in AA 2024-T3. Journal of Manufacturing Processes 29 (2017), pp. 62–73.

AIRBUS 03.03.2016
Airbus: Pioneering bionic 3D printing. https://www.airbus.com/en/newsroom/news/2016-03-pioneering-bionic-3d-printing,

ALI ET AL. 2019
Ali, U.; Esmaeilizadeh, R.; Ahmed, F.; Sarker, D.; Muhammad, W.; Keshavarzkermani, A.; Mahmoodkhani, Y.; Marzbanrad, E.; Toyserkani, E.: Identification and characterization of spatter particles and their effect on surface roughness, density and mechanical response of 17-4 PH stainless steel laser powder-bed fusion parts. Materials Science and Engineering: A 756 (2019), pp. 98–107.

AMANO ET AL. 2021a
Amano, H.; Ishimoto, T.; Suganuma, R.; Aiba, K.; Sun, S.-H.; Ozasa, R.; Nakano, T.: Effect of a helium gas atmosphere on the mechanical properties of Ti-6Al-4V alloy built with laser powder bed fusion: A comparative study with argon gas. Additive Manufacturing 48 (2021), pp. 1–9.

AMANO ET AL. 2021b
Amano, H.; Yamaguchi, Y.; Ishimoto, T.; Nakano, T.: Reduction of Spatter Generation Using Atmospheric Gas in Laser Powder Bed Fusion of Ti–6Al–4V. Material Transactions 62 (2021) 8, pp. 1225–1230.

AMANO ET AL. 2023
Amano, H.; Ishimoto, T.; Hagihara, K.; Suganuma, R.; Aiba, K.; Sun, S.-H.; Wang, P.; Nakano, T.: Impact of gas flow direction on the crystallographic texture evolution in laser beam powder bed fusion. Virtual and Physical Prototyping 18 (2023) 1, pp. 1–16.

ANDANI ET AL. 2017
Andani, M. T.; Dehghani, R.; Karamooz-Ravari, M. R.; Mirzaeifar, R.; Ni, J.: Spatter formation in selective laser melting process using multi-laser technology. Materials & Design 131 (2017), pp. 460–469.

ANDANI ET AL. 2018
Andani, M. T.; Dehghani, R.; Karamooz-Ravari, M. R.; Mirzaeifar, R.; Ni, J.: A study on the effect of energy input on spatter particles creation during selective laser melting process. Additive Manufacturing 20 (2018), pp. 33–43.

ANISIMOV 1968
Anisimov, S. I.: Vaporization of metal absorbing laser radiation. Journal of Experimental and Theoretical Physics 27 (1968) 1, p. 182 f.

ANWAR ET AL. 2019
Anwar, A. B.; Ibrahim, I. H.; Pham, Q.-C.: Spatter transport by inert gas flow in selective laser melting: A simulation study. Powder Technology 352 (2019), pp. 103–116.

ANWAR & PHAM 2016
Anwar, A. B.; Pham, Q.-C.: Effect of inert gas flow velocity and unidirectional scanning on the formation and accumulation of spattered powder during selective laser melting. Proceedings of the 2nd International Conference on Progress in Additive Manufacturing (2016), pp. 531–536.

ANWAR & PHAM 2017
Anwar, A. B.; Pham, Q.-C.: Selective laser melting of AlSi10Mg: Effects of scan direction, part placement and inert gas flow velocity on tensile strength. Journal of Materials Processing Technology 240 (2017), pp. 388–396.

ANWAR & PHAM 2018
Anwar, A. B.; Pham, Q.-C.: Study of the spatter distribution on the powder bed during selective laser melting. Additive Manufacturing 22 (2018), pp. 86–97.

BAEHR ET AL. 2021
Baehr, S.; Ammann, T.; Matheson, G.; Wimmer, A.; Zaeh, M.: Cracking Behavior of a Zr-blended Al-Zn-Mg Alloy Processed by Powder Bed Fusion of Metals Using a Laser Beam Under Different Process Gas Mixtures. Proceedings of the Metal Additive Manufacturing Conference (2021).

BAEHR ET AL. 2022
Baehr, S.; Melzig, L.; Bauer, D.; Ammann, T.; Zaeh, M. F.: Investigations of process by-products by means of Schlieren imaging during the powder bed fusion of metals using a laser beam. Journal of Laser Applications 34 (2022) 4, 42045.

BAEHR ET AL. 2024a
Baehr, S.; Klecker, T.; Pielmeier, S.; Ammann, T.; Zaeh, M. F.: Experimental and analytical investigations of the removal of spatters by various process gases during the powder bed fusion of metals using a laser beam. Progress in Additive Manufacturing 9 (2024), pp. 905–917.

BAEHR ET AL. 2024b
Baehr, S.; Matheson, G.; Ammann, T.; Mayr, P.; Zaeh, M. F.: Influence of argon, helium, and their mixtures on the powder bed fusion of an Al–Cu–Li–Ti alloy using a laser beam: Evaporation, microstructure, and mechanical properties. Advances in Industrial and Manufacturing Engineering 8 (2024), 100142.

BAEHR ET AL. 2024c
Baehr, S.; Fritz, F.; Adami, S.; Ammann, T.; Adams, N. A.; Zaeh, M. F.: Investigations on the Heat Balance of the Melt Pool during PBF-LB/M under Various Process Gases. Metals 14 (2024) 9, 1058.

BAEHR & STEPHAN 2011
Baehr, H. D.; Stephan, K.: Heat and Mass Transfer. Berlin, Heidelberg: Springer 2011.

BÄHR ET AL. 2020
Bähr, S.; Ammann, T.; Matheson, G.; Evirgen, A.; Forêt, P.; Bachmann, A.; Zäh, M. F.: Influence of Different Process Gases on AlSi10Mg Parts Processed By LPBF – Microstructure and Mechanical Properties. Proceedings of the European Powder Metallurgy Congress (2020).

BAUER ET AL. 2016
Bauer, D. M.; Dietrich, K.; Walter, M.; Forêt, P.; Palm, F.; Witt, G.: Effect of Process Gas and Powder Quality on Aluminum Alloys Processed by Laser Based Powder Bed Melting Process. Proceedings of the 27th Annual International Solid Freeform Fabrication Symposium (2016).

BERGMUELLER ET AL. 2023
Bergmueller, S.; Gerhold, L.; Fuchs, L.; Kaserer, L.; Leichtfried, G.: Systematic approach to process parameter optimization for laser powder bed fusion of low-alloy steel based on melting modes. The International Journal of Advanced Manufacturing Technology 126 (2023) 9-10, pp. 4385–4398.

BIDARE ET AL. 2017
Bidare, P.; Maier, R.; Beck, R. J.; Shephard, J. D.; Moore, A. J.: An open-architecture metal powder bed fusion system for in-situ process measurements. Additive Manufacturing 16 (2017), pp. 177–185.

BIDARE ET AL. 2018a
Bidare, P.; Bitharas, I.; Ward, R. M.; Attallah, M. M.; Moore, A. J.: Fluid and particle dynamics in laser powder bed fusion. Acta Materialia 142 (2018), pp. 107–120.

BIDARE ET AL. 2018b
Bidare, P.; Bitharas, I.; Ward, R. M.; Attallah, M. M.; Moore, A. J.: Laser powder bed fusion in high-pressure atmospheres. The International Journal of Advanced Manufacturing Technology 99 (2018) 1-4, pp. 543–555.

BOUKHA ET AL. 2013
Boukha, Z.; Sánchez-Amaya, J. M.; González-Rovira, L.; Rio, E. D.; Blanco, G.; Botana, J.: Influence of CO2-Ar Mixtures as Shielding Gas on Laser Welding of Al-Mg Alloys. Metallurgical and Materials Transactions A 44 (2013) 13, pp. 5711–5723.

BUDZIER & GERLACH 2023
Budzier, H.; Gerlach, G.: Pyrometrie und Thermografie – Leitfaden für die Praxis (engl.: Pyrometry and thermography – guidelines for practical use): John Wiley & Sons 2023.
ISBN: 9783527830374.

CH ET AL. 2019
Ch, S. R.; Raja, A.; Nadig, P.; Jayaganthan, R.; Vasa, N. J.: Influence of working environment and built orientation on the tensile properties of selective laser melted AlSi10Mg alloy. Materials Science and Engineering A 750 (2019), pp. 141–151.

CHEN ET AL. 2022
Chen, Q.; Fu, Y.; To, A. C.: Multiphysics modeling of particle spattering and induced defect formation mechanism in Inconel 718 laser powder bed fusion. The International Journal of Advanced Manufacturing Technology 123 (2022) 3-4, pp. 783–791.

CHEN ET AL. 2023
Chen, A.; Li, B.; Chen, X.; Jiang, M.; Zou, S.; Tao, W.; Lei, Z.; Chen, Y.: Experimental and Numerical Investigation of Shielding Gas Behaviors in Laser Welding of TC4 Alloy. Materials 16 (2023) 19.

CHEN & YAN 2020
Chen, H.; Yan, W.: Spattering and denudation in laser powder bed fusion process: Multiphase flow modelling. Acta Materialia 196 (2020), pp. 154–167.

CHENG ET AL. 2020
Cheng, C.; Liu, L.; He, H.; Luo, B.; Hu, J.; Chen, W.; He, J.: Experimental study of the dynamics of leader initiation with a long dark period. Journal of Physics D: Applied Physics 53 (2020) 20, 205203.

CHIEN ET AL. 2021
Chien, C.-Y.; Le, T.-N.; Lin, Z.-H.; Lo, Y.-L.: Numerical and experimental investigation into gas flow field and spattering phenomena in laser powder bed fusion processing of Inconel 718. Materials & Design 210 (2021), 110107.

CHOWDHURY ET AL. 2022
Chowdhury, S.; Yadaiah, N.; Prakash, C.; Ramakrishna, S.; Dixit, S.; Gupta, L. R.; Buddhi, D.: Laser powder bed fusion: a state-of-the-art review of the technology, materials, properties & defects, and numerical modelling. Journal of Materials Research and Technology 20 (2022), pp. 2109–2172.

CHUNG ET AL. 1999
Chung, B. G.; Rhee, S.; Lee, C. H.: The effect of shielding gas types on CO2 laser tailored blank weldability of low carbon automotive galvanized steel. Materials Science and Engineering A 272 (1999) 2, pp. 357–362.

DAI & GU 2015
Dai, D.; Gu, D.: Effect of metal vaporization behavior on keyhole-mode surface morphology of selective laser melted composites using different protective atmospheres. Applied Surface Science 355 (2015), pp. 310–319.

DAUB 2012
Daub, R.: Increasing the Weld Pool Depth during the Heat Conduction Mode Laser Beam Welding of Steel. Dissertation. Technical University of Munich. Munich, Germany (2012).

DEBROY ET AL. 2018
DebRoy, T.; Wei, H. L.; Zuback, J. S.; Mukherjee, T.; Elmer, J. W.; Milewski, J. O.; Beese, A. M.; Wilson-Heid, A.; De, A.; Zhang, W.: Additive manufacturing of metallic components – Process, structure and properties. Progress in Materials Science 92 (2018), pp. 112–224.

DECKERS ET AL. 2024
Deckers, T.; Fardan, A.; Kersting, L.; Kreutzer, A.; Forêt, P.; Goff, S. D.-L.; Witt, G.; Kleszczynski, S.; Klement, U.; Hryha, E.: Impact of processing gas composition on process stability and properties of PBF-LB/M processed alloy 718. Journal of Manufacturing Processes 120 (2024), pp. 712–718.

DIN EN ISO/ASTM 52900:2021
DIN EN ISO/ASTM 52900:2021: Additive manufacturing - General principles - Fundamentals and vocabulary. German Institute for Standardization. Berlin: Beuth 2021.

DOWNIE 2002
Downie, N. A.: Industrial Gases. New York, Boston, Dordrecht, London, Moscow: Kluwer Academic Publishers 2002.

EOS GMBH 2024
EOS GmbH: EOS Aluminium AlSi10Mg (2024). Available online at
<https://store.eos.info/collections/aluminum-powders/products/eos-aluminum-alsi10mg>.

GEBHARDT 2016
Gebhardt, A.: Additive Manufacturing. 3D Printing for Prototyping and Manufacturing. Munich: Hanser 2016.

GENGENBACH 2007
Gengenbach, J.: REM-Berechnung und Messung des Emissionsgrades mikrostrukturierter Oberflächen (engl.: SEM calculation and measurement of the emissivity of microstructured surfaces). Dissertation. Helmut Schmidt University. Hamburg, Germany (2007).

GIBSON ET AL. 2021
Gibson, I.; Rosen, D.; Stucker, B.; Khorasani, M.: Additive manufacturing technologies. Cham, Switzerland: Springer 2021.

GRIESINGER 2019
Griesinger, A. C.: Wärmemanagement in der Elektronik – Theorie und Praxis (engl.: Thermal management in electronics – theory and practice). Berlin, Heidelberg: Springer Vieweg 2019.

GRUND 2015
Grund, M.: Implementierung von schichtadditiven Fertigungsverfahren (engl.: Implementation of layer-wise additive manufacturing processes). Berlin, Heidelberg: Springer Vieweg 2015.

GUO ET AL. 2018
Guo, Q.; Zhao, C.; Escano, L. I.; Young, Z.; Xiong, L.; Fezzaa, K.; Everhart, W.; Brown, B.; Sun, T.; Chen, L.: Transient dynamics of powder spattering in laser powder bed fusion additive manufacturing process revealed by in-situ high-speed high-energy x-ray imaging. Acta Materialia 151 (2018), pp. 169–180.

HAUBOLD & ZÄH 2019
Haubold, M. W.; Zäh, M. F.: Real-time spatter detection in laser welding with beam oscillation. Procedia CIRP 79 (2019), pp. 159–164.

HEELING ET AL. 2017
Heeling, T.; Gerstgrasser, M.; Wegener, K.: Investigation of selective laser melting spatter characteristics for single- and multi-beam strategies using high speed imaging. Proceedings of the Lasers in Manufacturing Conference (2017), pp. 1–10.

HOPPE & ENK 2019
Hoppe, B.; Enk, S.: Schlieren- and Shadowgraphy for Visualization of the Shielding Gas Dynamics in Laser Powder Bed Fusion (L-PBF). Proceedings of the 16th Rapid.Tech Conference (2019).

HU ET AL. 2016
Hu, H.; Fetzer, F.; Berger, P.; Eberhard, P.: Simulation of laser welding using advanced particle methods. GAMM-Mitteilungen 39 (2016) 2, pp. 112–265.

HU & EBERHARD 2017
Hu, H.; Eberhard, P.: Thermomechanically coupled conduction mode laser welding simulations using smoothed particle hydrodynamics. Computational Particle Mechanics 4 (2017) 4, pp. 473–486.

HÜGEL & GRAF 2009
Hügel, H.; Graf, T.: Laser in der Fertigung – Strahlquellen, Systeme, Fertigungsverfahren (engl.: Lasers in manufacturing – beam sources, systems, manufacturing processes). Wiesbaden: Vieweg+Teubner Verlag 2009.

KALMAN ET AL. 2005
Kalman, H.; Satran, A.; Meir, D.; Rabinovich, E.: Pickup (critical) velocity of particles. Powder Technology 160 (2005) 2, pp. 103–113.

KAPLAN & POWELL 2011
Kaplan, A. F.; Powell, J.: Spatter in laser welding. Journal of Laser Applications 23 (2011) 3, pp. 1–7.

KATAYAMA 2020
Katayama, S.: Fundamentals and details of laser welding. Singapore: Springer 2020.

KENT 1992
Kent, J. A.: Riegel's Handbook of Industrial Chemistry. New York: Van Nostrand Reinhold 1992.

KHAIRALLAH ET AL. 2016
Khairallah, S. A.; Anderson, A. T.; Rubenchik, A.; King, W. E.: Laser powder-bed fusion additive manufacturing: Physics of complex melt flow and formation mechanisms of pores, spatter, and denudation zones. Acta Materialia 108 (2016), pp. 36–45.

KHORASANI ET AL. 2020
Khorasani, A.; Gibson, I.; Veetil, J. K.; Ghasemi, A. H.: A review of technological improvements in laser-based powder bed fusion of metal printers. The International Journal of Advanced Manufacturing Technology 108 (2020) 1-2, pp. 191–209.

KOTADIA ET AL. 2021
Kotadia, H. R.; Gibbons, G.; Das, A.; Howes, P. D.: A review of Laser Powder Bed Fusion Additive Manufacturing of aluminium alloys: Microstructure and properties. Additive Manufacturing 46 (2021) 102155.

LADEWIG ET AL. 2016
Ladewig, A.; Schlick, G.; Fisser, M.; Schulze, V.; Glatzel, U.: Influence of the shielding gas flow on the removal of process by-products in the selective laser melting process. Additive Manufacturing 10 (2016), pp. 1–9.

LI ET AL. 2014
Li, S.; Chen, G.; Katayama, S.; Zhang, Y.: Relationship between spatter formation and dynamic molten pool during high-power deep-penetration laser welding. Applied Surface Science 303 (2014), pp. 481–488.

LI ET AL. 2023
Li, Z.; Yu, G.; He, X.; Gan, Z.; Liu, W. K.: Vapor-induced flow and its impact on powder entrainment in laser powder bed fusion. Materials Today Communications 36 (2023) 106669.

LINDE GMBH 2024
Linde GmbH: Linde Gas – Technische Gase und Zubehör online kaufen (engl.: Linde Gas – buy industrial gases and accessories online) (2024). Available online at <https://www.linde-gas.de/shop/de/de-ig/home>.

LIU & WEN 2022
Liu, J.; Wen, P.: Metal vaporization and its influence during laser powder bed fusion process. Materials & Design 215 (2022).

LUTTER-GÜNTHER ET AL. 2018
Lutter-Günther, M.; Bröker, M.; Mayer, T.; Lizak, S.; Seidel, C.; Reinhart, G.: Spatter formation during laser beam melting of AlSi10Mg and effects on powder quality. Procedia CIRP 74 (2018), pp. 33–38.

MEINERS 1999
Meiners, W.: Direktes Selektives Laser Sintern einkomponentiger metallischer Werkstoffe (engl.: Direct selective laser sintering of single-component metallic materials). Dissertation. RWTH Aachen. Aachen, Germany (1999).

MONAGHAN 1992
Monaghan, J. J.: Smoothed Particle Hydrodynamics. Annual Review of Astronomy and Astrophysics 30 (1992), pp. 543–574.

MONAGHAN ET AL. 2005
Monaghan, J. J.; Huppert, H. E.; Grae Worster, M.: Solidification using smoothed particle hydrodynamics. Journal of Computational Physics 206 (2005) 2, pp. 684–705.

MONAGHAN & GINGOLD 1983
Monaghan, J. J.; Gingold, R. A.: Shock simulation by the particle method SPH. Journal of Computational Physics 52 (1983) 2, pp. 374–389.

NARASIMHARAJU ET AL. 2022
Narasimharaju, S. R.; Zeng, W.; See, T. L.; Zhu, Z.; Scott, P.; Jiang, X.; Lou, S.: A comprehensive review on laser powder bed fusion of steels: Processing, microstructure, defects and control methods, mechanical properties, current challenges and future trends. Journal of Manufacturing Processes 75 (2022), pp. 375–414.

OBEIDI ET AL. 2020
Obeidi, M. A.; Mussatto, A.; Groarke, R.; Vijayaraghavan, R. K.; Conway, A.; Rossi Kaschel, F.; McCarthy, E.; Clarkin, O.; O'Connor, R.; Brabazon, D.: Comprehensive assessment of spatter material generated during selective laser melting of stainless steel. Materials Today Communications 25 (2020), 101294.

OLIVEIRA ET AL. 2023
Oliveira, A. R. de; Castro, H. L. de; Santos, S. F.; Jardini, A. L.; Del Conte, E. G.: Effects of spatter deposition and build location in laser powder bed fusion of maraging steel parts. The International Journal of Advanced Manufacturing Technology 129 (2023) 5-6, pp. 2111–2123.

PAKKANEN 2018
Pakkanen, J. A.: Designing for Additive Manufacturing. Dissertation. Politecnico di Torino. Torino, Italy (2018).

PAN ET AL. 2022
Pan, Z.; Nadimpalli, V. K.; Christiansen, T. L.; Andersen, S. A.; Kjer, M. B.; Mishin, O. V.; Zhang, Y.: Influence of shielding gas flow on the uniformity of additively manufactured martensitic stainless steel. IOP Conference Series: Materials Science and Engineering 1249 (2022) 1, 12026.

PANIGRAHI & MURALIDHAR 2012
Panigrahi, P. K.; Muralidhar, K.: Schlieren and Shadowgraph Methods in Heat and Mass Transfer. New York, NY: Springer New York 2012.

PARENTI ET AL. 2024
Parenti, P.; Puccio, D.; Semeraro, Q.; Colosimo, B. M.: A techno-economic approach for decision-making in metal additive manufacturing: metal extrusion versus single and multiple laser powder bed fusion. Progress in Additive Manufacturing 9 (2024) 2, pp. 185–210.

PAUZON ET AL. 2019
Pauzon, C.; Hryha, E.; Forêt, P.; Nyborg, L.: Effect of argon and nitrogen atmospheres on the properties of stainless steel 316 L parts produced by laser-powder bed fusion. Materials & Design 179 (2019), pp. 1–10.

PAUZON ET AL. 2020
Pauzon, C.; Forêt, P.; Hryha, E.; Arunprasad, T.; Nyborg, L.: Argon-helium mixtures as Laser-Powder Bed Fusion atmospheres: Towards increased build rate of Ti-6Al-4V. Journal of Materials Processing Technology 279 (2020).

PAUZON ET AL. 2021a
Pauzon, C.; Raza, A.; Hryha, E.; Forêt, P.: Oxygen balance during laser powder bed fusion of Alloy 718. Materials & Design 201 (2021), pp. 1–10.

PAUZON ET AL. 2021b
Pauzon, C.; Hoppe, B.; Pichler, T.; Dubiez-Le Goff, S.; Forêt, P.; Nguyen, T.; Hryha, E.: Reduction of incandescent spatter with helium addition to the process gas during laser powder bed fusion of Ti-6Al-4V. CIRP Journal of Manufacturing Science and Technology 35 (2021), pp. 371–378.

PAUZON ET AL. 2022a
Pauzon, C.; van Petegem, S.; Hryha, E.; Sin Ting Chang, C.; Hocine, S.; van Swygenhoven, H.; Formanoir, C. de; Dubiez-Le Goff, S.: Effect of helium as process gas on laser powder bed fusion of Ti-6Al-4V studied with operando diffraction and radiography. European Journal of Materials (2022), pp. 422–435.

PAUZON ET AL. 2022b
Pauzon, C.; Mishurova, T.; Fischer, M.; Ahlström, J.; Fritsch, T.; Bruno, G.; Hryha, E.: Impact of contour scanning and helium-rich process gas on performances of Alloy 718 lattices produced by laser powder bed fusion. Materials & Design 215 (2022), pp. 1–12.

PEI ET AL. 2023
Pei, E.; Bernard, A.; Gu, D.; Klahn, C.; Monzón, M.; Petersen, M.; Sun, T.: Springer Handbook of Additive Manufacturing. Cham: Springer International Publishing; Imprint Springer 2023.

PFALZ ET AL. 2023
Pfalz, T.; Rota, A.; Saeidnezhad, N.; Leyens, C.: Comparison of different multi-laser powder bed fusion exposure strategies and their influence on the part quality of IN718. The International Journal of Advanced Manufacturing Technology 128 (2023) 9-10, pp. 4469–4490.

POLING ET AL. 2001
Poling, B. E.; Prausnitz, J. M.; O'Connell, J. P.: The properties of gases and liquids. New York: McGraw-Hill 2001.

QIN ET AL. 2021
Qin, Y.; Liu, J.; Chen, Y.; Wen, P.; Zheng, Y.; Tian, Y.; Voshage, M.; Schleifenbaum, J. H.: Influence of Laser Energy Input and Shielding Gas Flow on Evaporation Fume during Laser Powder Bed Fusion of Zn Metal. Materials 14 (2021) 10, pp. 1–17.

RAKESH ET AL. 2018
Rakesh, C. S.; Priyanka, N.; Jayaganthan, R.; Vasa, N. J.: Effect of build atmosphere on the mechanical properties of AlSi10Mg produced by selective laser melting. Materials Today: Proceedings 5 (2018) 9, pp. 17231–17238.

REIJONEN ET AL. 2020
Reijonen, J.; Revuelta, A.; Riipinen, T.; Ruusuvuori, K.; Puukko, P.: On the effect of shielding gas flow on porosity and melt pool geometry in laser powder bed fusion additive manufacturing. Additive Manufacturing 32 (2020), pp. 1–10.

RUDOLPH ET AL. 2023
Rudolph, K.; Kübler, M.; Noack, M.; Kirchner, E.: Influence of Joining Zone Geometry on Material Distribution in Electrochemically Produced Component Joints in Additive Manufacturing. In: Lachmayer, R.; Bode, B.; Kaierle, S. (Eds.): Innovative Product Development by Additive Manufacturing 2022. 1st ed. 2023 Aufl. Cham: Springer International Publishing; Imprint Springer 2023, pp. 31–46.

RUSSELL ET AL. 2018
Russell, M. A.; Souto-Iglesias, A.; Zohdi, T. I.: Numerical simulation of Laser Fusion Additive Manufacturing processes using the SPH method. Computer Methods in Applied Mechanics and Engineering 341 (2018), pp. 163–187.

SCHLICHTING, H., GERSTEN, K. 2006
Schlichting, H., Gersten, K.: Boundary Layer Theory. Berlin, Heidelberg: Springer 2006.

SCHMIDT ET AL. 2020
Schmidt, L.; Schricker, K.; Bergmann, J. P.; Junger, C.: Effect of Local Gas Flow in Full Penetration Laser Beam Welding with High Welding Speeds. Applied Sciences 10 (2020) 5, pp. 1–19.

SCHWEIER ET AL. 2013
Schweier, M.; Heins, J. F.; Haubold, M. W.; Zaeh, M. F.: Spatter Formation in Laser Welding with Beam Oscillation. Physics Procedia 41 (2013), pp. 20–30.

SETTLES 2001
Settles, G. S.: Schlieren and Shadowgraph Techniques. Visualizing Phenomena in Transparent Media. Berlin Heidelberg: Springer 2001.

SHEN ET AL. 2020
Shen, H.; Rometsch, P.; Wu, X.; Huang, A.: Influence of Gas Flow Speed on Laser Plume Attenuation and Powder Bed Particle Pickup in Laser Powder Bed Fusion. JOM 72 (2020) 3, pp. 1039–1051.

SIMONELLI ET AL. 2015
Simonelli, M.; Tuck, C.; Aboulkhair, N. T.; Maskery, I.; Ashcroft, I.; Wildman, R. D.; Hague, R.: A Study on the Laser Spatter and the Oxidation Reactions During Selective Laser Melting of 316L Stainless Steel, Al-Si10-Mg, and Ti-6Al-4V. Metallurgical and Materials Transactions A 46 (2015) 9, pp. 3842–3851.

SIREN ET AL. 2001
Siren, K.; Rosén, G.; Vad, J.; Nielsen, P. V.: Industrial Ventilation Design Guidebook. Experimental Techniques. 2001.

SLODCZYK ET AL. 2021
Slodczyk, M.; Ilin, A.; Kiedrowski, T.; Bareth, T.; Ploshikhin, V.: Spatter reduction by multi-beam illumination in laser powder-bed fusion. Materials & Design 212 (2021), 110206.

SOUNDARARAJAN ET AL. 2021
Soundararajan, B.; Sofia, D.; Barletta, D.; Poletto, M.: Review on modeling techniques for powder bed fusion processes based on physical principles. Additive Manufacturing 47 (2021), 102336.

STOKES ET AL. 2022
Stokes, M. A.; Khairallah, S. A.; Volkov, A. N.; Rubenchik, A. M.: Fundamental physics effects of background gas species and pressure on vapor plume structure and spatter entrainment in laser melting. Additive Manufacturing 55 (2022), 102819.

STUTZMAN ET AL. 2023
Stutzman, C.; Przyjemski, A.; Nassar, A. R.: Effects of gas flow speed on bead geometry and optical emissions during laser powder bed fusion additive manufacturing. Rapid Prototyping Journal 29 (2023) 7, pp. 1386–1394.

TRAORE ET AL. 2021
Traore, S.; Schneider, M.; Koutiri, I.; Coste, F.; Fabbro, R.; Charpentier, C.; Lefebvre, P.; Peyre, P.: Influence of gas atmosphere (Ar or He) on the laser powder bed fusion of a Ni-based alloy. Journal of Materials Processing Technology 288 (2021), 116851.

TREJOS-TABORDA ET AL. 2022
Trejos-Taborda, J.; Reyes-Osorio, L.; Garza, C.; Del Carmen Zambrano-Robledo, P.; Lopez-Botello, O.: Finite element modeling of melt pool dynamics in laser powder bed fusion of 316L stainless steel. The International Journal of Advanced Manufacturing Technology 120 (2022) 5-6, pp. 3947–3961.

VDI 3405:2014
VDI 3405:2014: Additive manufacturing processes, rapid manufacturing. The Association of German Engineers. Berlin: Beuth 2014.

VDI E.V. 2013
VDI e.V.: VDI Heat Atlas. Berlin Heidelberg: Springer Vieweg 2013.

WALTER ET AL. 2019
Walter, J.; Griemsmann, T.; Hustedt, M.; Hoff, C.; Hermsdorf, J.; Kaierle, S.: Safety during handling of metal powders in the course of additive manufacturing: Risk assessment along the entire process chain. Lasers in Manufacturing Conference 2019 (2019), pp. 1–12.

WANG ET AL. 2007
Wang, H.; Shi, Y.; Gong, S.; Duan, A.: Effect of assist gas flow on the gas shielding during laser deep penetration welding. Journal of Materials Processing Technology 184 (2007) 1-3, pp. 379–385.

WANG ET AL. 2014
Wang, X. J.; Zhang, L. C.; Fang, M. H.; Sercombe, T. B.: The effect of atmosphere on the structure and properties of a selective laser melted Al–12Si alloy. Materials Science and Engineering: A 597 (2014), pp. 370–375.

WANG ET AL. 2017
Wang, D.; Wu, S.; Fu, F.; Mai, S.; Yang, Y.; Liu, Y.; Song, C.: Mechanisms and characteristics of spatter generation in SLM processing and its effect on the properties. Materials & Design 117 (2017), pp. 121–130.

WANG ET AL. 2021
Wang, D.; Dou, W.; Ou, Y.; Yang, Y.; Tan, C.; Zhang, Y.: Characteristics of droplet spatter behavior and process-correlated mapping model in laser powder bed fusion. Journal of Materials Research and Technology 12 (2021), pp. 1051–1064.

WANG ET AL. 2024
Wang, D.; Yongqiang, Y.; Yang, L.; Yuchao, B.; Chaolin, T.: Laser Powder Bed Fusion of Additive Manufacturing Technology. Singapore: Springer Nature Singapore; Imprint Springer 2024.

WEAVER ET AL. 2023
Weaver, J.; Schlenoff, A.; Deisenroth, D.; Moylan, S.: Assessing the influence of non-uniform gas speed on the melt pool depth in laser powder bed fusion additive manufacturing. Rapid Prototyping Journal 29 (2023) 8, pp. 1580–1591.

WEIRATHER ET AL. 2019
Weirather, J.; Rozov, V.; Wille, M.; Schuler, P.; Seidel, C.; Adams, N. A.; Zaeh, M. F.: A Smoothed Particle Hydrodynamics Model for Laser Beam Melting of Ni-based Alloy 718. Computers & Mathematics with Applications 78 (2019) 7, pp. 2377–2394.

WILKE 1950
Wilke, C. R.: A Viscosity Equation for Gas Mixtures. The Journal of Chemical Physics 18 (1950) 4, pp. 517–519.

WILLE ET AL. 2002
Wille, G.; Millot, F.; Rifflet, J. C.: Thermophysical Properties of Containerless Liquid Iron up to 2500 K. International Journal of Thermophysics 23 (2002), pp. 1197–1206.

WILLIAMS ET AL. 2016
Williams, S. W.; Martina, F.; Addison, A. C.; Ding, J.; Pardal, G.; Colegrove, P.: Wire + Arc Additive Manufacturing. Materials Science and Technology 32 (2016) 7, pp. 641–647.

WIMMER ET AL. 2018
Wimmer, A.; Zeller, C.; Bayerlein, F.; Scherer, D.; Zaeh, M. F.; Forêt, P.; Scholz, J.: Influence of the Process Gas on the Laser Beam Melting Process. Proceedings of the Seventh International Conference on Additive Technologies (2018), pp. 66–70.

WIMMER ET AL. 2021
Wimmer, A.; Yalvac, B.; Zoeller, C.; Hofstaetter, F.; Adami, S.; Adams, N. A.; Zaeh, M. F.: Experimental and Numerical Investigations of In Situ Alloying during Powder Bed Fusion of Metals Using a Laser Beam. Metals 11 (2021) 11, 1842.

WIRTH ET AL. 2021
Wirth, F.; Frauchiger, A.; Gutknecht, K.; Cloots, M.: Influence of the Inert Gas Flow on the Laser Powder Bed Fusion (LPBF) Process. Industrializing Additive Manufacturing (2021), pp. 192–204.

XIA & PESTANA 2023
Xia, W.; Pestana, L. A.: Fundamentals of Multiscale Modeling of Structural Materials: Elsevier 2023. ISBN: 978-0-12-823021-3.

XU ET AL. 2019
Xu, J.; Luo, Y.; Zhu, L.; Han, J.; Zhang, C.; Chen, D.: Effect of shielding gas on the plasma plume in pulsed laser welding. Measurement 134 (2019), pp. 25–32.

YOUNG ET AL. 2020
Young, Z. A.; Guo, Q.; Parab, N. D.; Zhao, C.; Qu, M.; Escano, L. I.; Fezzaa, K.; Everhart, W.; Sun, T.; Chen, L.: Types of spatter and their features and formation mechanisms in laser powder bed fusion additive manufacturing process. Additive Manufacturing 36 (2020), 101438.

ZHANG ET AL. 2013
Zhang, M. J.; Chen, G. Y.; Zhou, Y.; Li, S. C.; Deng, H.: Observation of spatter formation mechanisms in high-power fiber laser welding of thick plate. Applied Surface Science 280 (2013), pp. 868–875.

ZÖLLER ET AL. 2023
Zöller, C.; Adams, N. A.; Adami, S.: Numerical investigation of balling defects in laser based powder bed fusion of metals with Inconel 718. Additive Manufacturing 73 (2023), 103658.

Appendix

A. List of embedded key publications

This section lists the publications that were embedded into this dissertation. Please note that wherever bibliographic indices are missing, the information is not available or not known to the author.

Publication P1: Bähr, S.; Ammann, T.; Matheson, G.; Evirgen, A.; Forêt, P.; Bachmann, A.; Zäh, M. F.: In-fluence of Different Process Gases on AlSi10Mg Parts Processed By LPBF – Microstructure and Mechanical Properties. Proceedings of the European Powder Metallurgy Congress (2020).

Publication P2: Baehr, S.; Ammann, T.; Matheson, G.; Wimmer, A.; Zaeh, M.: Cracking Behavior of a Zr-blended Al-Zn-Mg Alloy Processed by Powder Bed Fusion of Metals Using a Laser Beam Under Different Process Gas Mixtures. Proceedings of the Metal Additive Manufacturing Conference (2021).

Publication P3: Baehr, S.; Klecker, T.; Pielmeier, S.; Ammann, T.; Zaeh, M. F.: Experimental and analytical investigations of the removal of spatters by various process gases during the powder bed fusion of metals using a laser beam. Progress in Additive Manufacturing 9 (2024), pp. 905–917.

Publication P4: Baehr, S.; Melzig, L.; Bauer, D.; Ammann, T.; Zaeh, M. F.: Investigations of process by-products by means of Schlieren imaging during the powder bed fusion of metals using a laser beam. Journal of Laser Applications 34 (2022) 4, 42045.

Publication P5: Baehr, S.; Fritz, F.; Adami, S.; Ammann, T.; Adams, N. A.; Zaeh, M. F.: Investigations on the Heat Balance of the Melt Pool during PBF-LB/M under Various Process Gases. Metals 14 (2024) 9, 1058.

Publication P6: Baehr, S.; Matheson, G.; Ammann, T.; Mayr, P.; Zaeh, M. F.: Influence of argon, helium, and their mixtures on the powder bed fusion of an Al–Cu–Li–Ti alloy using a laser beam: Evaporation, microstructure, and mechanical properties. Advances in Industrial and Manufacturing Engineering 8 (2024), 100142.

B. List of supervised student research projects

In the context of the research performed by the author, various student research projects (see Table B.1) were intensively supervised by the author of this thesis with regard to the methodology, problem statements, objectives, and approach, along with the interpretation and documentation of the results. The supervision took place at the Institute for Machine Tools and Industrial Management (*iwb*) of the Technical University of Munich (TUM). The findings and results of the student research projects listed below have contributed to this dissertation. The author would like to express his sincere gratitude for the remarkable commitment of all supervised students and their interesting and important contributions.

Table B.1: List of supervised student research projects

Name of student	**Research project**			
	Title	**Type**	**Date of submission**	**Language**
Franziska Gutmair	Analysis of the process gas influence during laser powder bed fusion (*iwb* no. 2020/54287)	Bachelor's thesis	July 2020	German
Sebastian Pielmeier	Development of a method for the experimental investigation of the influence of different process gases on the formation of process by-products during laser beam melting (*iwb* no. 2020/53974)	Bachelor's thesis	November 2020	English
Tobias Klecker	Numerical Calculation of the Process Gas Flow in a Laser-based Powder Bed Fusion Machine (*iwb* no. 2021/56031)	Bachelor's thesis	March 2021	German
Matthias Wagenstetter	Feasibility study for the production of additively manufactured structures with specifically adjusted damping behavior (*iwb* no. 2021/56242)	Master's thesis	April 2021	German
Martin Guggemos	Investigations of aging processes in laser beam molten parts made of aluminum-based powder materials (*iwb* no. 2021/56828)	Bachelor's thesis	May 2021	German
Nguyen Toan Le	Experimental Investigations on the Influence of the Process Gas during Laser-based Powder Bed Fusion on Crack Formation in High-Strength Aluminum Alloys (*iwb* no. 2021/58450)	Bachelor's thesis	August 2021	English

Lichu Wang	Numerical Representation and Investigation of the Influence of different Process Gases During Laser-based Powder Bed Fusion (*iwb* no. 2021/58454)	Master's thesis	August 2021	English
Tobias Klecker	Numerical analysis of the influence of different process gases on the heat balance during the powder bed fusion of metals using a laser beam (*iwb* no. 2021/59454)	Semester's project	November 2021	English
Maximilian Reiserer	Simulative and Experimental Determination of Criteria for the Identification of Thermally Critical Component Areas in Laser-based Powder Bed Fusion (*iwb* no. 2021/59938)	Semester's project	December 2021	English
Lukas Melzig	Experimental Investigations on the Influence of the Process Gas during Laser-based Powder Bed Fusion on Mechanical Part Properties of High-Strength Aluminum Alloys (*iwb* no. 2022/62190)	Semester's project	May 2022	English
Franz Wolf	Experimental and Analytical Investigations on the Influence of Process Gases on the Production Process of Filigree Structures during Powder Bed Fusion of a Nickel-Based Alloy Using a Laser Beam (*iwb* no. 2022/62427)	Master's thesis	June 2022	English
Matthias Lang	Experimental and Analytical Investigation of the Influence of the Process Gas on the Powder Bed Fusion of C18150 Using a Laser Beam (*iwb* no. 2023/63710)	Master's thesis	July 2023	English